PREDICTION OF STRUCTURES AND PROPERTIES OF HIGH-PRESSURE SOLID MATERIALS USING FIRST PRINCIPLES METHODS

A Thesis Submitted to the College of

Graduate Studies and Research

In Partial Fulfillment of the Requirements

For the Degree of Master of Science

In the Department of Physics and Engineering Physics

University of Saskatchewan

Saskatoon

By

MICHAEL JAMES GRESCHNER

Permission to Use

In presenting this thesis in partial fulfilment of the requirements for a Postgraduate degree from the University of Saskatchewan, I agree that the Libraries of this University may make it freely available for inspection. I further agree that permission for copying of this thesis in any manner, in whole or in part, for scholarly purposes may be granted by the professor or professors who supervised my thesis work or, in their absence, by the Head of the Department or the Dean of the College in which my thesis work was done. It is understood that any copying or publication or use of this thesis or parts thereof for financial gain shall not be allowed without my written permission. It is also understood that due recognition shall be given to me and to the University of Saskatchewan in any scholarly use which may be made of any material in my thesis.

Requests for permission to copy or to make other use of material in this thesis in whole or part should be addressed to:

Head of the Department of Physics and Engineering Physics

University of Saskatchewan

Saskatoon, Saskatchewan S7N5E2

ABSTRACT

The purpose of the research contained in this thesis is to allow for the prediction of new structures and properties of crystalline structures due to the application of external pressure by using first-principles numerical computations. The body of the thesis is separated into two primary research projects.

The properties of cupric oxide (CuO) have been studied at pressures below 70 GPa, and it has been suggested that it may show room-temperature multiferroics at pressure of 20 to 40 GPa. However, at pressures above these ranges, the properties of CuO have yet to be examined thoroughly. The changes in crystal structure of CuO were examined in these high-pressure ranges. It was predicted that the ambient pressure monoclinic structure changes to a rocksalt structure and CsCl structure at high pressure. Changes in the magnetic ordering were also suggested to occur due to superexchange interactions and Jahn-Teller instabilities arising from the d-orbital electrons. Barium chloride (BaCl) has also been observed, which undergoes a similar structural change due to an $s - d$ transition, and whose structural changes can offer further insight into the transitions observed in CuO.

Ammonia borane (NH_3BH_3) is known to have a crystal structure which contains the molecules in staggered conformation at low pressure. The crystalline structure of NH_3BH_3 was examined at high pressure, which revealed that the staggered configuration transforms to an eclipsed conformation stabilized by homopolar $B–H^{\delta-}\cdots {}^{\delta-}H–B$ dihydrogen bonds. These bonds are shown to be covalent in nature, comparable in bond strength to conventional hydrogen bonds, and may allow for easier molecular hydrogen formation in hydrogen fuel storage.

STATEMENT OF CO-AUTHORSHIP

The research reported in this thesis are a result of collaborations between the author, Michael J. Greschner, supervisor Dr. Yansun Yao, Dr. John S. Tse and Xue Yong of the Department of Physics and Engineering Physics at the University of Saskatchewan, Dr. Ning Chen of the HXMA beamline at the Canadian Light Source Inc. and Dr. Dennis D. Klug of the National Research Council of Canada, whose contributions are described below.

Chapter 1 describes the underlying theory and computational methodology used in this thesis, and was written by Michael J. Greschner.

Chapter 2 is based primarily on the paper "Pressure-driven suppression of the Jahn-Teller effects and structural changes in cupric oxide" by Michael J. Greschner, Ning Chen and Yansun Yao [J. Phys. Cond. Matt., **2016**, *28*, 025401]. Calculations of equations of state and phonon dispersion were carried out by Michael J. Greschner. Measurement and calculation of XANES and XRD were performed by Ning Chen. Analysis and manuscript drafting were performed by all authors. Chapter 2 also contains a digression into a second paper, "Prediction of a Novel Stable Half-Metal Ferromagnetic BaCl Solid" by Michael J. Greschner, Dennis D. Klug and Yansun Yao [accepted for publication in Phys. Rev. B., February 22, 2016], as the results and discussion therein are relevant to the previous paper. Equation of state calculations, electronic band structure, Wannier functions and superconducting properties were calculated by Yansun Yao. Charge density calculations were performed by Michael J. Greschner. Density of state and projected density of state calculations were performed by Michael J. Greschner and Yansun Yao. Phonon dispersions were calculated by Dennis. D. Klug. Manuscript was drafted by all authors.

Chapter 3 is based on the paper “Dihydrogen Bonding in Compressed Ammonia Borane and Its Roles in Structural Stability” by Yansun Yao, Xue Yong, John S. Tse and Michael J. Greschner [*J. Phys. Chem.*, **2014**, *118*, 29591]. Equation of state and Bader analysis were calculated by Yansun Yao. All-electron charge densities were mapped by Michael J. Greschner. Natural bond orbital calculations, Wiberg bond index calculations and charge decomposition analysis were performed by Xue Yong and John S. Tse. The manuscript was drafted by Yansun Yao, with revisions by all authors.

Other work has also been performed, but is not included in this thesis for reasons of continuity.

1. Michael J. Greschner, Meng Zhang, Arnab Majumdar, Hanyu Liu, Feng Peng, John S. Tse and Yansun Yao. “A new allotrope of nitrogen as high-energy density material”, J. Phys. Chem. (submitted)

ACKNOWLEDGMENTS

I am immensely grateful to my supervisor, Dr. Yansun Yao. He gave me a chance to prove myself, and without that, this thesis would never have been possible. I am extremely thankful to Yansun for the trust he has placed in me throughout my time working with him, whether it was through the research we did together, the opportunity to present our work on my own, or the writing up of our projects. I would also like to thank him for the generous financial support he provided.

I would also like to thank those who I worked with and who supported me at the Canadian Light Source. Along with the financial support provided by them, I would like to thank everyone who allowed me the opportunity to work in such an amazing facility, and those I had a chance to work with, especially Dr. Josef Hormes, Dr. Emil Hallin and Dr. Tom Ellis, for giving me the opportunity to work there when I first came to Saskatoon; Dr. Joyce McBeth, for stepping in as supervisor when Yansun was away; and Tracy Walker, Victoria Martinez and the whole Outreach and Education team.

Thanks also goes out to the ICT department at the University of Saskatchewan and Compute Canada for the use of their computing clusters, without whom none of this research would have been possible.

Last, but certainly not least, I would like to thank my parents and my sisters for believing in me, even when I was at my worst.

TABLE OF CONTENTS

page

LIST OF TABLES

LIST OF FIGURES

Figure page

LIST OF ABBREVIATIONS

DFT ..... Density Functional Theory

LDA ..... Local Density Approximation

GGA ..... Generalized-Gradient Approximation

LSDA ..... Local Spin Density Approximation

PBE ..... Perdew-Burke-Ernzerhof

HSE ..... Heyd-Scuseria-Ernzerhof

SR ..... Short-Range

LR ..... Long-Range

BZ ..... First Brillouin Zone

MP ..... Monkhorst-Pack

PP ..... Pseudopotential

AE ..... All-Electron

EOS ..... Equation of State

*p*V ..... Pressure-Volume

HXMA ..... Hard X-ray MicroAnalysis

VASP .....Vienna Ab initio Simulation Package

FCC .....Face-Centered Cubic

BCC ..... Body-Centered Cubic

IFC .....Interatomic Force Constant

CN .....Coordinate Number

AIRSS .....Ab Initio Random Structure Searching

XANES .....X-ray Absorption Near Edge Structures

NN ..... Nearest Neighbor

NNN ..... Next Nearest Neighbor

XRD ..... X-Ray Diffraction

EXAFS ..... Extended X-ray Absorption Fine Structure

DOS ..... Density of States

ISQ .....Interstitial Quasi-atoms

pDOS ..... Projected Density of States

vdW .....van der Waals

CSD ..... Cambridge Structural Database

MD .....Molecular Dynamics

QTAIM ..... Quantum Theory of Atoms in Molecules

NBO ..... Natural Bond Orbital

WBI .....Wiberg Bond Index

CDA ..... Charge Decomposition Analysis

ECDA ..... Extended Charge Decomposition Analysis

MO .....Molecular Orbital

CHAPTER 1

INTRODUCTION

1.1 Ab Initio Methods and Quantum Mechanics

In recent decades, computer simulations have become a useful tool to support both theoretical and experimental studies in science. Computer simulation can allow theoretical hypotheses to be modelled, and can provide predictions and help identify processes of experiments. They also allow for virtual experiments to be performed in situations that are difficult, dangerous or otherwise impossible with the current experimental capabilities in a laboratory setting, such as the high pressures which may be encountered in physical sciences. However, the results of any simulation are only as reliable as the theory being applied to produce them, and as many of the theories are difficult, if not impossible, to exactly calculate, approximations must be made in order to provide numerical results. In order to reduce the number of approximations needed, simulation models are often formulated from fundamental laws of nature, or *ab initio*, from the Latin for "from the beginning".

In condensed matter physics, the most fundamental laws of nature are derived from quantum mechanics, and so any *ab initio* simulation method must be derived from these laws. Using the laws of quantum mechanics, it should be possible to describe any electronic system in terms of its wavefunction. While in principle the full theoretical formulation of quantum

mechanics must necessarily include the theory of relativity to describe massive or fast moving particles, a more simple formulation taking into account only the non-relativistic, time-independent, stationary nucleus description is sufficient in most cases. To describe these systems, it is thus necessary to solve Schrödinger's equation,

$$\hat{H}\Psi(\vec{r}_1,\vec{r}_2,...,\vec{r}_N) = E\Psi(\vec{r}_1,\vec{r}_2,...,\vec{r}_N), \qquad (1.1)$$

where $\hat{H}$ is the Hamiltonian operator, $\Psi(\vec{r}_1,\vec{r}_2,...,\vec{r}_N)$ is the many-body wavefunction with $\vec{r}_i$ being the electronic degrees of freedom, and E is the total energy of the system.

As the interactions in chemistry and physics are dependent on the laws of quantum mechanics, the mathematical theory behind the underlying physical laws of these fields are thus completely known, so long as the wavefunction of the system can be described. Unfortunately, the exact analytical solution for a given system is often too complicated for the equations to be solved. Only in fairly simple cases, such as the case of hydrogen, or hydrogen-like, atoms, can these equations be completely solved [1]. The difficulty arises is because more complex systems must deal with large numbers of interacting particles. In these systems the physical laws are no different, nor more complex, dealing primarily with Coulomb interactions between charged particles, *i.e.* electrons and protons. The difficulty lies in the fact that there must be N electrons and M nuclei, all interacting together in the electronic system, which must be accounted for in the Hamiltonian operator as

$$\hat{H} = \sum_{i=1}^{N}\left(-\frac{\hbar^2}{2m}\nabla_i^2\right) - \sum_{i=1}^{N}\sum_{j=1}^{M}\frac{Z_j e^2}{\left|\vec{r}_i - \vec{R}_j\right|} + \frac{1}{2}\sum_{i=1}^{N}\sum_{j\neq i}\frac{e^2}{\left|\vec{r}_i - \vec{r}_j\right|}. \qquad (1.2)$$

In this form, the Hamiltonian in Eq. 1.2 contains three terms. The first term covers the kinetic energy of the N electrons. The second and third terms are the Coulombic interactions. The second term then is the interaction between the N electrons and the M nuclei, which is system

dependent, and can be considered as an external potential (v_{ext}), while the third term is the electron-electron repulsion. While in principle the kinetic energy of the nuclei should also be included, in practice, compared to the speed of the electrons, the nuclei are practically motionless, and thus the kinetic energy is negligible and can be ignored. This is the Born-Oppenheimer approximation. In the Hamiltonian, $\hbar$ is the reduced Planck constant, m is the mass of the electron, Z_j is the atomic number of the jth nucleus, e is the standard charge and $\vec{R}_j$ is the position of the jth nucleus. In future equations, atomic units will be used, such that $\hbar = m = e = 1$, for easier readability.

These last two terms in the Hamiltonian are pair-wise interactions, and their inclusion is the crux of the complications in solving the Schrödinger equation. Taking these into account renders the many-body wavefunction too complex to solve for, as it must be 3N-dimensional, and the difficulty in solving it grows dramatically with the increasing number of electrons and nuclei in the system. Thus, new methods of tackling the Schrödinger equation must be formulated in the forms of approximations made to decrease complexity.

One method of approximation, which dates back to the 1920s and 1930s, was proposed by D. R. Hartree and V. A. Fock [2]. The Hartree-Fock method assumes that the electrons move independently from each other, thus ignoring the pairwise interaction. It does this by assuming that the electrons feel an effective Coulomb potential which is due to the average position of all other electrons in the system. In order to preserve the Pauli Exclusion Principle, the many-particle wavefunction cannot be written as a product of the single-particle wavefunctions (as Hartree first suggested), as it does not satisfy the asymmetry requirement of the sign of the many-fermion wavefunction changing if any of the arguments are interchanged. In order to

satisfy this, the single-particle wavefunction must be written as an N×N Slater determinant of single-particle wavefunctions containing both spatial ($\vec{r}_i$) and spin (s_i) components:

$$\Psi \approx \frac{1}{\sqrt{N!}} \begin{vmatrix} \psi_1(\vec{r}_1 s_1) & \psi_1(\vec{r}_2 s_2) & \dots & \psi_1(\vec{r}_N s_N) \\ \psi_2(\vec{r}_1 s_1) & \psi_2(\vec{r}_2 s_2) & \dots & \psi_2(\vec{r}_N s_N) \\ \dots & \dots & \dots & \dots \\ \psi_N(\vec{r}_1 s_1) & \psi_N(\vec{r}_2 s_2) & \dots & \psi_N(\vec{r}_N s_N) \end{vmatrix} . \qquad (1.3)$$

The spatial components of the single-particle wavefunctions in Eq. 1.3 are obtained from the Schrödinger-like Hartree-Fock equations

$$\begin{aligned} &-\frac{1}{2}\nabla^2\psi_i(\vec{r}) - \sum_{j=1}^{M}\frac{Z_j}{|\vec{r}_i - \vec{R}_j|}\psi_i(\vec{r}) + \int d\vec{r}\,' n(\vec{r}\,')\frac{1}{|\vec{r} - \vec{r}\,'|}\psi_i(\vec{r}) \\ &-\sum_{j=1}^{N}\int d\vec{r}\,'\frac{1}{|\vec{r} - \vec{r}\,'|}\psi_j^*(\vec{r}\,')\psi_i(\vec{r}\,')\psi_j(\vec{r})\delta_{s_i s_j} = \varepsilon_i\psi_i(\vec{r}) \end{aligned} , \qquad (1.4)$$

where the fourth term on the left hand side is the exchange term. This term is called the "exchange" term because it fulfills the asymmetry requirements of the Pauli Exclusion Principle regarding the exchange of arguments in the wavefunction, as mentioned above. The third term is the Coulombic potential of the electrons, and in the case where

$$n(\vec{r}) = \sum_{i=1}^{N}|\psi_i(\vec{r})|^2 , \qquad (1.5)$$

this term is the Hartree potential, $v_H(\vec{r})$. From this formulation, we also find that the total energy in the Hartree-Fock method involves the sum over all *i* values and the integral over all space of the left-hand terms in the Hartree-Fock equations [2].

Despite these approximations, the Hartree-Fock method is still quite difficult to work with in many general cases. It is quite useful when the periodic potential is zero or constant, such as in the case of a free electron gas, and the free electron gas model does shed some light on further approximations which can be made for periodic potentials, such as in crystalline solids.

However, even with these increased approximations, the accuracy of predictions made solely with the Hartree-Fock method fall short of physical and chemical reality. Further refinements have been put forward to increase the accuracy of the Hartree-Fock method, but these improvements lead to increases in computation complexity, limiting their usefulness to small systems. Thus a new, less computationally intensive method was required to make computational results viable [3, 4].

1.2 Density Functional Theory

In density functional theory (DFT), the ground state of an electronic system can be determined from the electron density distribution, $n(\vec{r})$. This method of using the electron density was first suggested by L. H. Thomas and E. Fermi in the late 1920s. They assumed that the electron-electron interactions were determined by the classical Coulomb potential, that the electrons behaved as a Fermi gas, and that the kinetic energy of the electrons followed a local density approximation (LDA), where the contribution at any point $\vec{r}$ can be determined from the homogeneous electron gas density kinetic energy [5]. However, a more modern and widely known method of DFT was developed by Hohenberg, Kohn and Sham.

Like the Thomas-Fermi method, the Hohenberg-Kohn method assumes that the ground state of an electronic system, as well as the Hamiltonian and thus all the physical properties that can be found from it, depends solely on the ground state electron density. The total energy of the system, as stated by the Hohenberg-Kohn method, can be expressed in terms of the electron density, and must reach its minimum value as the density reaches the ground state density. Hohenberg and Kohn also showed that the external potential must be a unique functional of the

density (to within a constant). However, Hohenberg and Kohn showed that their method was only exact in the cases of a nearly constant electron density and of a slowly varying electron density [6]. A year after Hohenberg and Kohn's method was published, Kohn and Sham built on that formalism, as well as the Hartree and Hartree-Fock formalisms, developing the Kohn-Sham method.

In the Kohn-Sham method, the interacting electrons in an external potential in a many-body system are treated as non-interacting single quasi-particles in an effective potential. As long as the final ground state density remains the same, we can ensure that all the physical properties of the system are correct, so long as they are determined by the density. Kohn and Sham defined the potential acting on the electrons as having three parts,

$$v_{KS}(\vec{r}) = v_{ext}(\vec{r}) + v_H(\vec{r}) + \mu_{XC}(n(\vec{r})), \qquad (1.6)$$

where $v_{ext}(\vec{r})$ is the external potential, $v_H(\vec{r})$ is the Hartree potential as shown in third term in Eq. 1.4 with the condition shown in Eq. 1.5, and $\mu_{XC}(n(\vec{r}))$ is the exchange-correlation contribution to the chemical potential. As the electrons are considered non-interacting single particles, we transform the N-particle wavefunction problem we were faced with initially into a series of 1-particle wavefunctions, which satisfy the Kohn-Sham equations:

$$\left(-\frac{1}{2}\nabla^2 + v_{KS}(\vec{r})\right)\psi_i(\vec{r}) = \varepsilon_i\psi_i(\vec{r}). \qquad (1.7)$$

The Kohn-Sham method also describes the total ground state energy in terms of the electron density and an interacting inhomogeneous electron gas

$$E = \int d\vec{r}\, v_{ext}(\vec{r})n(\vec{r}) + \frac{1}{2}\int\int d\vec{r}\,d\vec{r}'\frac{n(\vec{r})n(\vec{r}')}{|\vec{r}-\vec{r}'|} + T_s[n] + E_{XC}[n(\vec{r})]. \qquad (1.8)$$

In Eq. 1.8, the first term is the energy arising from the external potential (E_{ext}). The second term is the energy arising from the Hartree potential (E_H), as described above. The third term is the kinetic energy of the system of non-interacting electrons with density $n(\vec{r})$. The fourth term is the exchange-correlation energy functional. In principle, all the terms except the exchange-correlation energy functional can be known exactly, and thus it is only the exchange-correlation parts which need to be approximated. This also allows all the complications arising from many-body interactions to be gathered into this one term. The exchange-correlation functional can be further broken down into an exchange part ($E_X[n(\vec{r})]$) and a correlation part ($E_C[n(\vec{r})]$) [7]

$$E_{XC}[n(\vec{r})] = E_X[n(\vec{r})] + E_C[n(\vec{r})] \ . \qquad (1.9)$$

Eq. 1.4 already defined the exact exchange potential in the Hartree-Fock method, which we can again make use of to determine the exact exchange energy functional

$$E_X^{exact}[n(\vec{r})] = -\sum_{i=1}^{N}\sum_{j=1}^{N}\int\int d\vec{r}\,d\vec{r}\,' \frac{\psi_i(\vec{r})\psi_i^*(\vec{r}\,')\psi_j^*(\vec{r})\psi_j(\vec{r}\,')}{|\vec{r}-\vec{r}\,'|}, \qquad (1.10)$$

where the $\psi_i(\vec{r})$ terms in Eq. 1.10 are the single-particle wavefunctions originating from the Kohn-Sham equation (Eq. 1.7) as opposed to the Hartree-Fock wavefunctions used in Eq. 1.4. While this does give an exact exchange in the Hartree-Fock style, the exchange functional does not depend explicitly on the electron density. Rather, it implicitly depends on the density through the Kohn-Sham wavefunctions. Furthermore, the correlation functional does not have an exact form as the exchange functional does. It was found that the exact exchange functional, paired with an approximate correlation functional, was not as precise as an approximate exchange functional which depended explicitly on the electron density paired with an approximate correlation functional [8].

Once the exchange-correlation and external potential terms have been specified, the method of using DFT to find the ground state of a system becomes one of self-consistent iteration. Starting with an initial guess of the electron density $n(\vec{r})$, the effective Kohn-Sham potential $v_{KS}(\vec{r})$ can be constructed. With the Kohn-Sham potential, the Kohn-Sham equation (Eq. 1.7) can be constructed for the system, and solved for the Kohn-Sham wavefunctions $\psi_i(\vec{r})$, which can then be used to determine a new electron density, as in Eq. 1.5. If this new density matches the initial density (within a given tolerance), then the ground state density has been found, and the ground state properties of the system can be determined. If not, the calculations are repeated, this time using the new density as the initial density, until convergence is reached. While this may, in principle, now sound like a complete method, there are still many steps which must be completed before these self-consistent calculations can be performed. The choice of exchange-correlation functionals is the most obvious point which needs to be resolved, but in addition, considerations concerning the treatment of periodic systems must also be addressed. This treatment will invariably depend on the *k*-space wavevectors in the system, and so we must also determine how to properly sample this space. Finally, a numerical solution to the Kohn-Sham equations will require that the Kohn-Sham wavefunctions be expanded in some basis set, and the choice of basis sets will affect the values derived from the DFT method as well [3, 4].

1.3 Exchange-Correlation

There are a number of different approximations which can be made to the exchange-correlation functional, and this thesis will address three of them; LDA, the generalized-gradient approximation (GGA) and hybrid functionals.

1.3.1 Local Density Approximation

LDA is one of the most straightforward, and more commonly used, approximations to the exchange-correlation term. In LDA, we assume that the exchange-correlation functional at any point in space for each electron in a non-uniform system is the same as the exchange-correlation energy of the homogeneous electron gas having the same electron density as at that point. In this way, then, we find

$$E_{XC}^{LDA}[n(\vec{r})] = \int d\vec{r}\, \varepsilon_{HEG}[n(\vec{r})] n(\vec{r}), \qquad (1.11)$$

where $\varepsilon_{HEG}[n(\vec{r})]$ is the exchange-correlation energy per particle of the homogeneous electron gas. Because LDA is based on the homogeneous electron gas, it is only exact in the case where the density is uniform, and gives the best results as an approximation in systems where the density is slowly varying. While this approximation is reasonable for some solid state materials, in the case of materials which are covalently bonded it is not sufficient. Another deficiency of this method is that is does not take into consideration the spin density. While in general it should be sufficient to solely consider the electron density, in systems where there may be unpaired electrons it has been shown that using a term $\varepsilon_{HEG}[n_{\uparrow}(\vec{r}), n_{\downarrow}(\vec{r})]$ in place of $\varepsilon_{HEG}[n(\vec{r})]$ in Eq. 1.11, where $\varepsilon_{HEG}[n_{\uparrow}(\vec{r}), n_{\downarrow}(\vec{r})]$ is the exchange-correlation energy density of a spin-polarized electron gas with spin up electron density $n_{\uparrow}(\vec{r})$ and spin down electron density $n_{\downarrow}(\vec{r})$, gives improved results over the LDA method. This method of including the spin-polarized electron densities is known as the local spin density approximation (LSDA). However, even LSDA is not a perfect approximation. In cases where LSDA does not give accurate results, it tends to overestimate binding energies and underestimate bond lengths [3, 4, 9].

1.3.2 Local Spin Density Approximation with Hubbard Correction

Another area where LSDA tends to fall short is in the prediction of properties of Mott insulators, like in 3*d* transition metal oxides, or in predicting ground state magnetic moments in high-T_c superconducting cuprates. Despite the fact that all the information for describing these systems appears to be contained in the LSDA approach, it has difficulty describing these systems. These highly-correlated systems can instead be described by approximations such as the Hubbard and Anderson-lattice models, which assume that the highly-correlated *d* or *f* electrons can be treated as being affected by on-site, quasiatomic interactions. Specifically, the Hubbard parameter *U*, where

$$U = E\left(d^{n+1}\right) + E\left(d^{n-1}\right) - 2E\left(d^{n}\right), \qquad (1.12)$$

is the Coulomb energy cost of placing two electrons at the same site, and $E\left(d^{x}\right)$ is the energy of the electron in the *d* orbital with occupancy *x*. The reason LSDA fails to describe these systems is because there is an inherent assumption within LSDA that the localization of electrons is controlled by the Hund's rule exchange parameter, *J*, through the Stoner parameter [10]. For 3*d* transition metals, the Stoner parameter is independent of crystal structure and magnetization, and is essentially a characteristic of the transition metal atom itself. In other words, LSDA reproduces the atomic term splittings, since in the homogeneous electron gas the spin dependence has its roots in the Hund's rule exchange *J*, but does not reproduce the integer only electron exchange in orbitals, instead producing unphysical energy minima from the partial orbital occupation (Fig. 1-1, obtained from Ref. 11). In systems like transition metal oxides, the Hubbard parameter *U* is responsible for the spin dependence, and in general *J* is on the order of 1

eV while *U* is on the order of 10 eV. This order of magnitude difference between *J* and *U* is what leads to the failing of LSDA in these systems [12]. Thus, in the LSDA+U method, we can write the rotationally invariant LSDA+U energy functional in terms of the LSDA energy functional $E^{LSDA}\left[\rho^{\sigma}(r)\right]$, the Hubbard energy functional $E^{U}\left[\left\{n^{\sigma}\right\}\right]$, which accounts for the screened Coulomb interactions, and the double counting energy functional $E^{dc}\left[\left\{n^{\sigma}\right\}\right]$,

$$E^{LSDA+U} = E^{LSDA}\left[\rho^{\sigma}(r)\right] + E^{U}\left[\left\{n^{\sigma}\right\}\right] - E^{dc}\left[\left\{n^{\sigma}\right\}\right], \qquad (1.13)$$

where $\rho^{\sigma}(r)$ is the charge density of electrons with spin σ and $\left\{n^{\sigma}\right\}$ are the elements of the density matrix. The double counting energy functional makes use of both *U* and *J*, as

$$E^{dc}\left[\left\{n^{\sigma}\right\}\right] = \frac{1}{2}U\left[n(n-1)\right] - \frac{1}{2}J\left[n^{\uparrow}\left(n^{\uparrow}-1\right) + n^{\downarrow}\left(n^{\downarrow}-1\right)\right], \qquad (1.14)$$

where $n^{\uparrow}$ and $n^{\downarrow}$ are the electron densities for spin up and spin down, respectively, and $n = n^{\uparrow} + n^{\downarrow}$ is the total electron density [12]. A further simplification to a rotationally invariant form of the LSDA+U method also exists, which reduces the dependence of *U* and *J* to an effective *U* parameter, $U_{eff} = U - J$, and [13]

$$E^{LSDA+U} = E^{LSDA}\left[\rho^{\sigma}(r)\right] + \frac{1}{2}(U-J)\left[n^{\uparrow}\left(n^{\uparrow}-1\right) + n^{\downarrow}\left(n^{\downarrow}-1\right) - \left\{n^{\uparrow}\left(n^{\uparrow}-1\right) + n^{\downarrow}\left(n^{\downarrow}-1\right)\right\}^{2}\right]. \qquad (1.15)$$

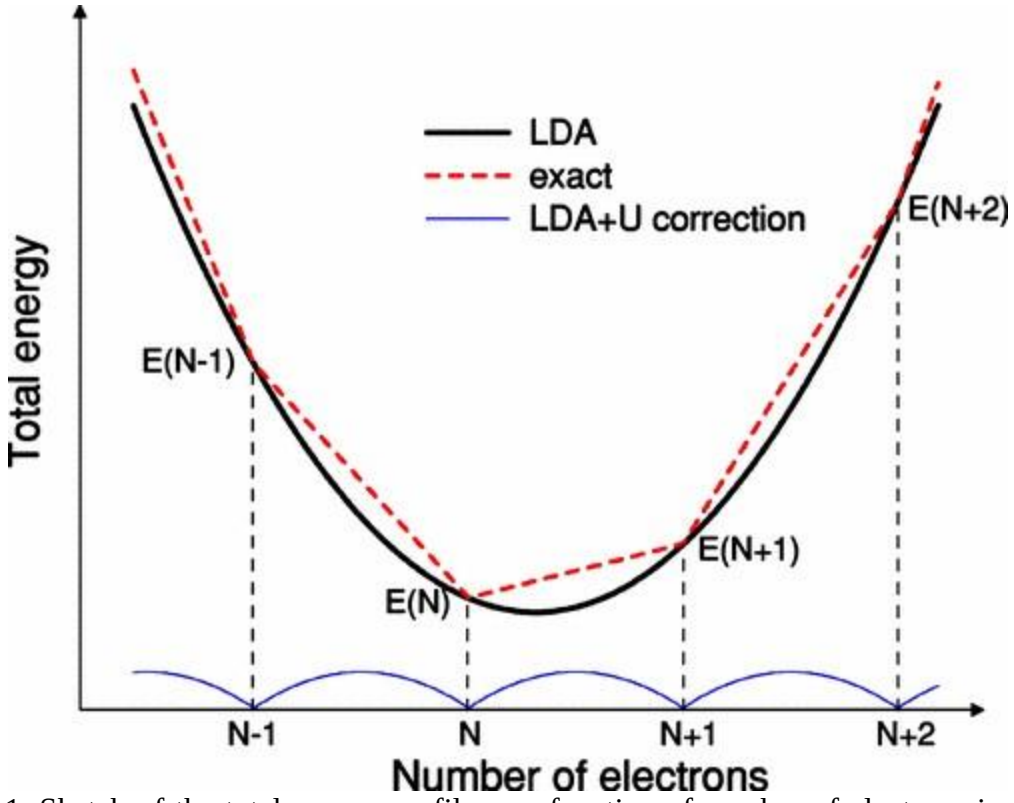

Figure 1-1. Sketch of the total energy profile as a function of number of electrons in a generic atomic system in contact with a reservoir. The bottom curve is simply the difference between the other two (the LDA energy and the "exact" result for an open system). [11].

1.3.4 Generalized-Gradient Approximation

To overcome the deficiencies which may arise in the LSDA method, GGA was developed as somewhat of an extension to LSDA. In GGA, the exchange-correlation functional depends on both the local electron density and the variations in space of the electron density, through the gradient, $\vec{\nabla} n(\vec{r})$. As such, the energy functional takes the form

$$E_{XC}^{GGA}[n(\vec{r})] = \int d\vec{r}\, \varepsilon_{XC}[n(\vec{r})] F_{XC}[n(\vec{r}), \vec{\nabla} n(\vec{r})] n(\vec{r}). \quad (1.16)$$

In Eq. 1.16, $F_{XC}[n(\vec{r}), \vec{\nabla} n(\vec{r})]$ is known as the enhancement factor, which incorporates both an exchange term and a correlation term. Dimensional analysis of $E_{XC}^{GGA}[n(\vec{r})]$ indicates that

$F_{XC}\left[n(\vec{r}),\vec{\nabla}n(\vec{r})\right]$ must be dimensionless, as the units of Eq. 1.16 must be the same as in Eq. 1.11, and so the enhancement factor is usually expressed through a parameter, *s*,

$$s(\vec{r}) = \frac{\left|\vec{\nabla}n(\vec{r})\right|}{2k_F n(\vec{r})}, \qquad (1.17)$$

where k_F is the Fermi wavevector and has the form [15]

$$k_F = \left(3\pi^2 n(\vec{r})\right)^{\frac{1}{3}}. \qquad (1.18)$$

Because of the enhancement factor's dependence on the gradient of the density, there can be many different forms to the GGA, as opposed to the single form of LDA, which makes GGA more versatile. Like LDA, however, GGA does have its own downsides. It may overestimate bond lengths, underestimate band gaps, and promote non-magnetic states over magnetic ones [3, 4, 16].

1.3.5 Hybrid Functionals

As mentioned above, the exact form of the exchange functional can be expressed, but not the exact form of the correlation functional, and mixing the exact exchange with an approximate correlation does not give accurate results. It has been shown, however, that a mixing of the exact exchange with approximate exchange functionals and approximate correlation functionals does give accurate results for properties such as atomization energies and bond lengths [8]. In fact, the accuracy of these hybrid functionals, which average an order of 0.1 eV, are better even than the GGA, which averages an order of 0.2 eV [16]. These functionals have the form of

$$E_{XC}^{hybrid} = aE_X^{exact} + (1-a)E_X^{approx} + E_C^{approx}, \qquad (1.19)$$

where *a*, a value between 0 and 1, is the mixing fraction. The exact value of *a* will depend on the system it is being applied to, and will give the most accurate results if it can be fitted empirically to experimental data. However, despite the increases in accuracy from using hybrid functionals, they are more computationally intensive, which limits their applications.

The development of different approximations for exchange and correlation functionals is an area of interest in the community of computational physics and chemistry. In this work, we primarily focused on the use of the GGA functional proposed by Perdew, Burke and Ernzerhof (PBE) and the hybrid functional proposed by Heyd, Scuseria and Ernzerhof (HSE) [3, 4].

1.3.6 PBE Functionals

Of the different GGA functionals, the PBE functional is one of the most commonly used in DFT programs. A number of conditions for any GGA exchange-correlation functional are known, even if the exact form of the functional cannot be stated. One of the conditions is that the exchange-correlation functional in any GGA formulation must reduce to the same as the LDA exchange-correlation functional, *i.e.* to the exact exchange-correlation functional of a homogeneous electron gas, if the electron density is constant [17]. It has also been shown that the exchange-correlation energy must follow the criteria that [18]

$$E_{XC}\left[n(\vec{r})\right] \geq -1.68\int d\vec{r} n^{\frac{4}{3}}(\vec{r}). \qquad (1.20)$$

In order to fulfill this criteria, Perdew, Burke and Ernzerhof suggested that the exchange enhancement factor must also be bounded by $F_X(s) \leq 1.804$, and suggested a form of the enhancement factor as

$$F_x^{PBE}(s) = 1 + \kappa - \frac{\kappa}{1 + \frac{\mu s^2}{\kappa}}. \qquad (1.21)$$

In Eq. 1.21, $\kappa = 0.804$ and $\mu = 0.21951$. The value of κ was chosen to satisfy Eq. 1.20 and the bound on the enhancement factor, and the value of μ was chosen to so that the effective gradient coefficient for exchange cancels out the effective gradient coefficient for correlation. They also proposed using the correlation functional in the spin polarized form

$$E_C^{PBE}[n(\vec{r})] = \int d\vec{r} n(\vec{r})\{\varepsilon_C(r_s, \zeta) + H(r_s, \zeta, t)\}. \qquad (1.22)$$

Here, r_s is the Seitz radius and ζ is the relative spin polarization. $H(r_s, \zeta, t)$ is a correction term for the gradient contribution and has the form

$$H(r_s, \zeta, t) = \gamma \phi^3(\zeta) \ln\left[1 + \frac{\beta}{\gamma} t^2 \left(\frac{1 + At^2}{1 + At^2 + A^2 t^4}\right)\right], \qquad (1.23)$$

where $\beta \approx 0.066725$, $\gamma \approx 0.031091$ and

$$A = \frac{\beta}{\gamma}\left[\exp\left(\frac{-\varepsilon_C(r_s, \zeta)}{\gamma \phi^3(\zeta)}\right) - 1\right]^{-1}. \qquad (1.24)$$

t is the dimensionless density gradient, and has the form

$$t = \frac{|\vec{\nabla} n(\vec{r})|}{2\phi(\zeta) k_s n(\vec{r})}, \qquad (1.25)$$

where $k_s = \sqrt{4k_F/\pi}$ is the Thomas-Fermi wave number and $\phi(\zeta) = \left[(1+\zeta)^{\frac{2}{3}} + (1-\zeta)^{\frac{2}{3}}\right] \Big/ 2$ is the spin-scaling factor. Also in Eqs. 1.22 and 1.24, $\varepsilon_C(r_s, \zeta)$ is the correlation energy per electron for a homogeneous electron gas [20].

As mentioned, the PBE functional is one of the most commonly used in DFT. However, as with the previously mentioned methods, it too has its downsides. PBE functionals have a

tendency to overestimate bond lengths and lattice parameters by around 1%, which in turn affects any physical properties which are dependent on geometries, such as phonon frequencies, magnetism and ferroelectricity. A further enhancement of the PBE functional, which is the PBE functional revised for solids, or PBESol, was devised as well. This new formulation uses a value of $\mu = 10/81$, which is the gradient expansion form, and increases accuracy for slowly varying electron density, which increases accuracy of some properties in solids, such as phonon frequencies [3, 4, 21].

1.3.7 HSE Functional

As mentioned before, the mixing of the exact Hartree-Fock exchange term with approximate exchange and correlation terms gives very accurate results for calculated systems. However, in periodic systems, metallic systems, or systems of large molecules, calculating the exact exchange is extremely computationally expensive. Heyd, Scuseria and Ernzerhof considered the screened Coulomb interaction for the exact exchange in order to increase calculation efficiency [22]. In metals and periodic systems, the Coulomb potential has divergence issues with respect to the Fourier transform of $1/r$ ($4\pi/k^2$) at $k = 0$. However at short ranges, a screened Coulomb potential eliminates the divergence. Thus, they proposed that the exact Coulumb exchange can be separated into short-range (SR) and long-range (LR) parts of the form

$$\frac{1}{r} = \underbrace{\frac{1 - erf(\omega r)}{r}}_{SR} + \underbrace{\frac{erf(\omega r)}{r}}_{LR}, \qquad (1.26)$$

where $erf(\omega r)$ is the error function and ω is an adjustable parameter. The error function has the form

$$erf(\omega r) = \frac{2}{\sqrt{\pi}} \int_0^{\omega r} dt e^{-t^2} \ . \qquad (1.27)$$

From this, it can easily be seen that when ω goes to zero, the error function goes to zero, so the exact exchange is dominated by the short-range component. Similarly when ω goes to infinity, the error function goes to 1, so the exact exchange is dominated by the long-range component. The HSE hybrid functional was proposed using the exact exchange mixing only for the short-range interactions, as Heyd, Scuseria and Ernzerhof found that the long-range contributions of the exact HF exchange are rather small, so they can be approximated by just the approximate exchange. The HSE functional was formulated using the PBE functional for the approximate exchange, and so takes the form

$$E_{XC}^{HSE} = aE_X^{HF,SR}(\omega) + (1-a)E_X^{PBE,SR}(\omega) + E_X^{PBE,LR}(\omega) + E_C^{PBE}, \qquad (1.28)$$

where the mixing fraction used is $a = 1/4$, and they found that a value of $\omega = 0.15a_0^{-1}$ gave good accuracy and speed of calculations for both molecules and solids [3, 4, 22].

1.4 Periodic Systems

So far, these formulations of approximations to solve the Schrödinger equation for systems of electrons have all operated under the assumption that the number of electrons in the system is not too great to work with. However, in a crystalline solid, the number of electrons participating in the interactions reaches the order of Avogadro's number, which is large enough to be considered functionally infinite and render the calculations virtually impossible to compute.

However, the very fact that we are investigating crystalline solids offers an insight into the solution to this problem, as a crystal is defined by having a regularly repeating pattern of atoms. These regularly repeating patterns, or unit cells, can describe the entire crystal in terms of a small number of atoms and the three linearly independent lattice vectors which describe translations that reproduce the crystal exactly. This means that the properties of the solid as a whole, with its near infinite number of electrons, can then be determined from the much smaller unit cell. This is the essence of Bloch's theorem [3, 4].

1.4.1 Bloch's Theorem

Bloch's theorem states that the solutions to the Schrödinger equation for periodic potentials must have the form

$$\psi_i\left(\vec{k},\vec{r}\right)=u_i\left(\vec{k},\vec{r}\right)e^{i\vec{k}\cdot\vec{r}}, \qquad (1.29)$$

where $u_i\left(\vec{k},\vec{r}\right)$ has the same periodic properties as the lattice, *i.e.* $u_i\left(\vec{k},\vec{r}\right)=u_i\left(\vec{k},\vec{r}+\vec{T}\right)$, and where $\vec{T}$ is any of the translational lattice vectors. $\vec{k}$ is the wavevector of an electron in the first Brillouin Zone (BZ), described by the reciprocal lattice vectors. Being periodic, $u_i\left(\vec{k},\vec{r}\right)$ can be expressed as a Fourier series

$$u_i(\vec{k},\vec{r})=\sum_G c_{k,G}e^{i\vec{G}\cdot\vec{r}}, \qquad (1.30)$$

where $c_{k,G}$ are the Fourier coefficients, and the vectors $\vec{G}$ are the reciprocal lattice vectors. The Fourier series gives a planewave form to $u_i\left(\vec{k},\vec{r}\right)$. Applying Eq. 1.29 to Eq. 1.30 gives the periodic potentials in the form

$$\psi_i\left(\vec{k},\vec{r}\right)=\sum_G c_{k,G}e^{i\left(\vec{k}+\vec{G}\right)\vec{r}}\ . \qquad (1.31)$$

This formulation gives a planewave solution to the Kohn-Sham equations (Eq. 1.7). This allows us to expand the Kohn-Sham orbitals in terms of the planewave basis set whose completeness can be set through the kinetic energy of the system.

Bloch's theorem also lets us describe some other properties of the solid system with only a bit more thought. If Eq. 1.29 gives the wavefunction in a single unit cell, the wavefunction in a neighboring cell must have the form

$$\psi_i\left(\vec{k},\vec{r}+\vec{T}\right)=u_i\left(\vec{k},\vec{r}+\vec{T}\right)e^{i\vec{k}\cdot\left(\vec{r}+\vec{T}\right)}=u_i\left(\vec{k},\vec{r}\right)e^{i\vec{k}\cdot\vec{r}}e^{i\vec{k}\cdot\vec{T}}=\psi_i\left(\vec{k},\vec{r}\right)e^{i\vec{k}\cdot\vec{T}}\ . \qquad (1.32)$$

In other words, the wavefunction in neighboring cells differs only by a phase change. Similarly, the electron density in a neighboring cell has the form

$$n(\vec{r}+\vec{T})=\left|\psi_i\left(\vec{k},\vec{r}+\vec{T}\right)\right|^2=\left|\psi_i\left(\vec{k},\vec{r}\right)e^{i\vec{k}\cdot\vec{T}}\right|^2=\left|\psi_i\left(\vec{k},\vec{r}\right)\right|^2=n(\vec{r})\,, \qquad (1.33)$$

as in Eq. 1.5. Eq. 1.33 shows that, in the periodic system, the electron density has the periodicity as the rest of the system, as one would expect [3, 4, 23].

1.4.2 Cutoff Energy

In the Kohn-Sham method, the kinetic energy can be expressed as

$$\int d\vec{r}\,\psi^*\left(\vec{r}\right)\left(-\frac{\vec{\nabla}^2}{2}\right)\psi\left(\vec{r}\right). \qquad (1.34)$$

If we substitute the Bloch-form Kohn-Sham orbitals from Eq. 1.31 into Eq. 1.34, it gives us

$$\int d\vec{r}\sum_{G'}c^*_{k,G'}e^{-i\left(\vec{G}'+\vec{k}\right)\vec{r}}\left(-\frac{\vec{\nabla}^2}{2}\right)\sum_G c_{k,G}e^{i\left(\vec{G}+\vec{k}\right)\vec{r}}=\sum_G\left(\frac{\vec{G}+\vec{k}}{2}\right)^2\left|c_{k,G}\right|^2\ . \qquad (1.35)$$

Therefore the kinetic energy is proportional to the square of $\vec{G}+\vec{k}$. Thus, we can justify truncating the basis set of the system so that it only includes planewaves that have kinetic energy below some cutoff energy which is

$$E_{cut} \geq \left(\frac{\vec{G}+\vec{k}}{2} \right)^2 . \qquad (1.36)$$

This cutoff will necessarily introduce some error into the system, as we are deliberately not including the infinite possible planewaves necessary to describe the system entirely. However, by slowly increasing the kinetic energy cutoff, convergence of the total energy to a given, set tolerance can be reached [3, 4, 24].

1.4.3 K-Point Sampling

As mentioned above, the Bloch theorem formulation depends on the wavevectors in the BZ. In fact, each wavevector $\vec{k}$ leads to a new eigenequation of the Kohn-Sham equation. This shifts the problem of solving for a near-infinite number of electrons to one of solving for a finite number of electronic bands for an infinite number of *k*-points in the BZ. Obviously, switching from one infinite number to another does not reduce the complexity of the problem. However, the Kohn-Sham wavefunctions for similar $\vec{k}$ are very similar themselves, *i.e.* they do not change dramatically for small changes in $\vec{k}$. In practice, we can then represent the Kohn-Sham wavefunctions in the vicinity of a given *k*-point in reciprocal space as the wavefunction at that *k*-point. Therefore, rather than an integral over the BZ of an infinite number of *k*-points, we can use a summation over a finite number of *k*-points in the BZ

$$\int d\vec{k} F\left(\vec{k}\right) \approx \sum_i w_i F\left(\vec{k}_i\right), \qquad (1.37)$$

where w_i is the weighting of the *k*-point $\vec{k}_i$. One of the more widely uses methods of sampling the BZ in this way was developed by Monkhorst and Pack [25]. Their method was to use a uniform, *k*-point mesh, the Monkhorst-Pack (MP) mesh. The MP mesh makes use of the symmetry operations of the crystal lattice in order to confine the *k*-points to just a region in the BZ that is not reducible by symmetry operations, and also to define the weighting of the *k*-points. Due to this use of symmetries, a relatively small amount *k*-points can be used in order to perform calculations. If the energy resultant from a small *k*-point mesh is not accurate enough, a denser *k*-point mesh can always be used in its place, as it is not a variable property, like the cutoff energy [3, 4, 25].

1.4.4 Pseudopotentials

While it is true that using the cutoff energy to expand the planewave basis set to a finite size is useful to enable calculations, this method still has its problems. Specifically, the tightly bound core electrons require higher cutoff energy in order to expand the localized wavefunctions, which means more planewaves are required. Also, the valence electrons and core electrons must oscillate in the same regions of space, allowable because the wavefunctions are all orthogonal, and oscillating wavefunctions again require more planewaves. However, the valence electrons contribute much more strongly to the chemical properties of atoms than the core electrons do. This has led to the use of the pseudopotential approximation, which removes all ionic and core potentials and replaces them with a pseudopotential which reproduces just the

behavior of the valence electrons as pseudowavefunctions. Since only the region outside the core electrons needs to be considered, the pseudowavefunctions do not need to be orthogonal to the core wavefunctions, as long as the pseudowavefunctions have the same eigenvalue as the real wavefunctions, and do not need to oscillate, thus reducing the number of planewaves required in the basis set.

To construct a pseudopotential, it is first necessary to determine which electrons participate in bonding and which do not, which are, usually, the valence electrons and the core electrons, respectively. In oxygen, for example, the ground state of the electron configuration is $1s^2 2s^2 2p^4$, and so the 2*s* and 2*p* electrons would be the valence electrons. The next step is to determine the cutoff radius where the core electrons no longer interact with the valence electrons. Fig. 1-2 shows the radial atomic orbitals for oxygen up to the 3*s* orbital. In Fig. 1-2, the core 1*s* electrons can be seen to be localized to within about 1 bohr, hence the radial part of the pseudopotentials (PP) needs to be equal to the valence all-electron (AE) radial potentials above the cutoff raidus, r_c

$$R_{PP}(r) = R_{AE}(r), r \geq r_c . \qquad (1.38)$$

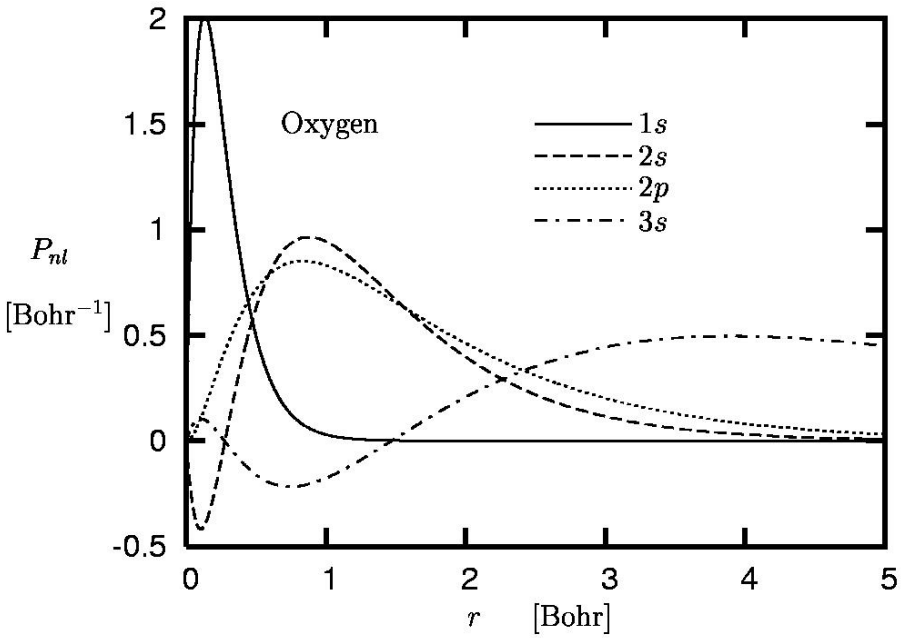

Figure 1-2. Radial atomic orbitals of an oxygen atom [26]. The horizontal axis shows the radial distance (r), and the vertical axis shows the radial probability distribution function (P_{nl}) for orbitals of principal quantum number n and azimuthal quantum number l.

In Figs. 1-3a and 1-3b, then, we see the radial parts of the all electron orbitals and pseudo-orbitals for the oxygen 2*s* (Fig. 1-3a) and 2*p* (Fig. 1-3b) electrons. Above the 1 bohr cutoff radius, we see that the pseudo-orbitals match the all electron orbitals exactly. Below cutoff, however, the pseudo-orbitals need not match as long as they produce the correct electron density in the core region, as this falls below the area of chemical activity. As we can see, in Fig. 1-3a, the 2*s* orbital has a node in the core region, while the pseudo-orbital is nodeless. The 2*p* orbital has no nodes since the number of nodes in the wavefunction is equal to $n-l-1$, thus $2-1-1=0$. Figures 1-2 and 1-3 were obtained from Ref. 26. Choosing a smaller cutoff radius will make the pseudopotential more adaptable to different types of systems; however, as mentioned above, a smaller cutoff would increase the number of planewaves, in turn increasing the calculation intensity [3, 4, 24].

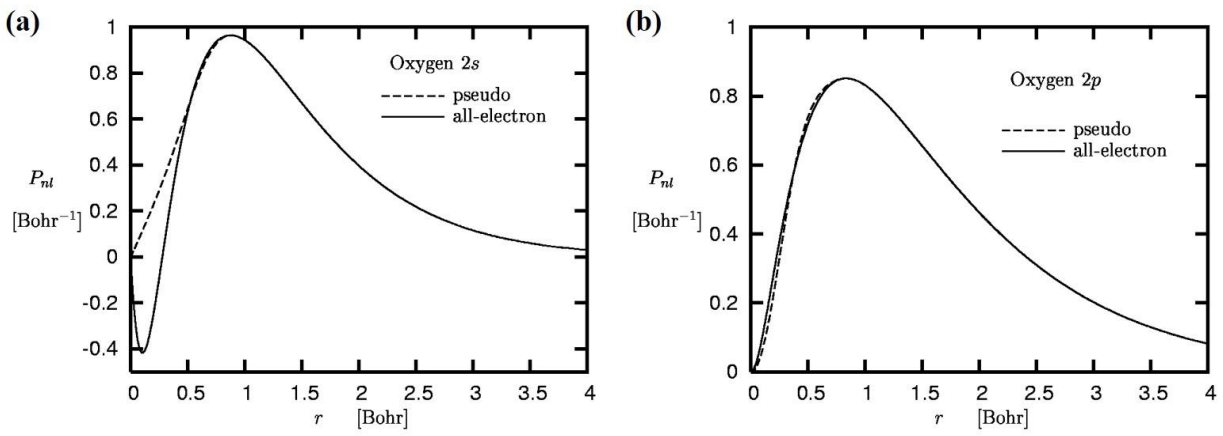

Figure 1-3. Radial all electron and pseudo-orbitals of oxygen for (a) 2s and (b) 2p electrons [26]. The horizontal axis shows the radial distance (r), and the vertical axis shows the radial probability distribution function (P_{nl}) for orbitals of principal quantum number n and azimuthal quantum number l.

1.5 DFT at High Pressure

The DFT methods described in the previous sections allow for the calculation of material properties at high pressures. Of great importance to high-pressure calculations are the ground state total energy, used to determine the pressure-dependent equations of state (EOS), as well as the phonon dispersions, which determine the mechanical and dynamical stabilities.

1.5.1 Equations of State

At high pressure, many structures which appear at ambient pressure become no longer stable, and change to a new, lower energy, or more stable, form. These new forms reduce strain and minimize forces on the atoms. Thus, a phase diagram can be constructed by comparing the total energy of a structure in terms of the formula unit. To include the pressure-volume (pV) effects on the total energy, the total Gibbs free energy ($G = E + pV - TS$) is often more useful to compare than the total energy, where T is the temperature and S is the entropy of the system. However, the calculations in this study are performed at zero temperature, and so we can consider the enthalpy instead ($H = E + pV$) without any loss of thermodynamic information. At each pressure, the total energy must be minimized by allowing the lattice shape and atomic coordinates to relax. Fig. 1-4 shows the equation of state phase diagram for ammonia borane (NH_3BH_3, more details in Chapter 3).

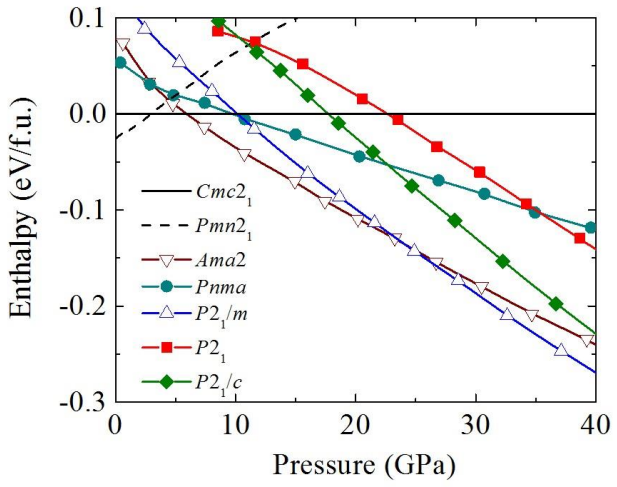

Figure 1-4. Equation of state phase diagram of ammonia borane, with the $Cmc2_1$ structure as the zero reference point [27].

In Figure 1-4, we see that as pressure increases, the structure changes; up to around 4 GPa, the $Pmn2_1$ is the stable structure. Above that point the structure changes, and takes on the $Cmc2_1$ space group, until about 9 GPa, when it again changes to the *Ama*2 space group. The *Ama*2 structure, once more, changes around 25 GPa to the $P2_1/m$ structure. Calculating these structural changes in general involves calculating the forces acting on each atom and the stress-tensor using the Hellmann-Feynman theorem [28, 29]. A stable structure has net forces minimized on any atom in the system. If the net forces are not balanced, then the energy could be further reduced by moving the atom in the direction of the non-zero force. The stress tensor respond to the external pressure if they are non-zero, and can be altered by changing the size and shape of the unit cell [4].

1.5.2 Structural Stability

In order for a structure to be considered stable, it must be not only energetically favored, but also mechanically and dynamically stable. One way of determining if the structure is mechanically and dynamically stable is through the phonon band structure. If the structure is unstable, the phonon band structure will have imaginary frequencies, often represented as negative frequencies in phonon frequency plots. These phonon band frequencies can be determined through the inter-atomic forces [4, 29]. Figs. 1-5a and 1-5b show examples of phonon dispersion plots for CuO in the *Fm*-3*m* structure (more details available in Chapter 2). The negative frequencies in Fig. 1-5a show that the structure is not mechanically and dynamically stable at 20 GPa. However, the increased pressure overcomes the instabilities, and so the structure becomes mechanically and dynamically stable above 40 GPa.

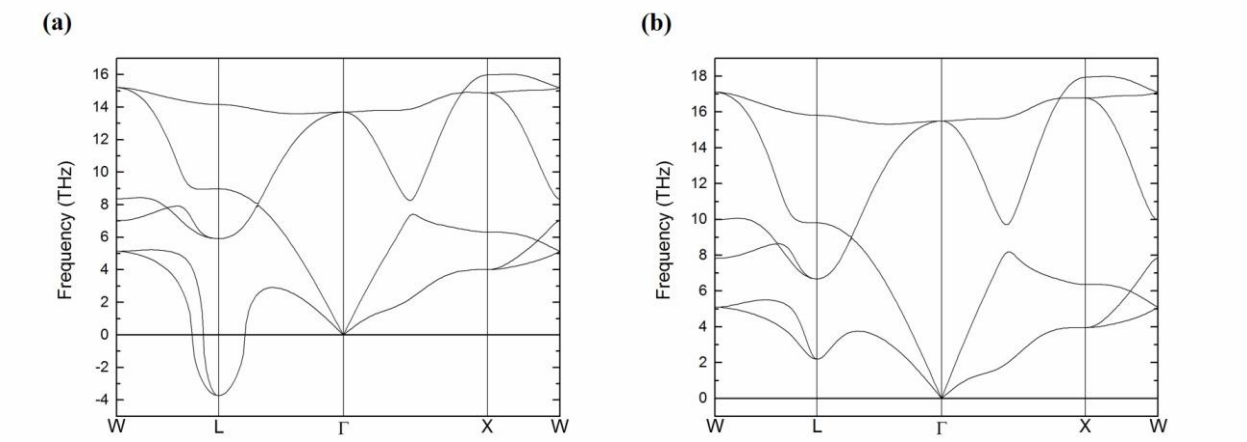

Figure 1-5. Phonon dispersions for CuO at (a) 20 GPa and (b) 40 GPa [30]. The vertical axis shows the phonon frequency, with imaginary frequencies represented by negative frequencies. The horizontal axis shows the specific *k*-points and the path between them that the phonons were calculated for.

1.5.3 VASP

VASP, or the Vienna *Ab initio* Simulation Package, is a first-principles package capable of performing electronic calculations through DFT. VASP is capable of using the Kohn-Sham equations, the Hartree-Fock approximation and hybrid functionals in order to approximate the solution to the many-body Schrödinger equation. VASP makes use of planewave basis sets to determine properties such as electronic charge density, and interactions between electrons and ions are described using projector augmented waves (PAW) [31]. All this allows VASP to determine forces and stress tensors, calculate magnetic moments, determine optical properties and allow for dynamics and relaxations to be calculated [4, 32].

1.5.4 PHON

PHON is a phonon frequency calculation program developed by Dario Alfè. It utilizes the ability of VASP (or other similar programs) to calculate the forces on atoms in a crystal in order to calculate the interatomic force constant (IFC) matrix using the small displacement method. The small displacement takes the atoms in a crystal and displaces them slightly from the ground state configuration, one at a time, making use of symmetry where appropriate, then calculates the forces acting on all the atoms in the crystal for each displacement. Doing this allows it to determine the force constant matrix, which in turn allows the phonon frequencies to be determined from the dynamical matrix (the phonon frequencies at a wavevector $\vec{k}$ are the eigenvalues of the dynamical matrix) [33].

1.6 Scope of this Study

This study is focused on the prediction of new, stable structures and properties of crystals in the framework of DFT. These were carried out with Dr. Yansun Yao and members of Dr. John S. Tse's research group from the Department of Physics and Engineering Physics at the University of Saskatchewan, as well as Dr. Ning Chen of the Hard X-ray MicroAnalysis (HXMA) beamline at Canadian Light Source, Inc and Dr. Dennis D. Klug at the National Research Council of Canada.

Chapter 2 focuses on the prediction of novel forms of cupric oxide (CuO) at high pressures. These predictions are performed primarily using the VASP and mechanical and dynamical stability was verified using the PHON program. We found that the monoclinic *C*2/*c*

structure transforms to a face-centered cubic (FCC) rocksalt structure, *Fm*-3*m*, at around 70 GPa, then to a body-centered cubic (BCC) CsCl structure, *Pm*-3*m*, at around 400 GPa through an intermediary *R*-3*m* structure. We also found that the magnetic structure may change from an antiferromagnetic structure to a non-magnetic and ferromagnetic structure, respectively. We also examine a second study of barium chloride, BaCl, which also undergoes similar structural and magnetic changes.

Chapter 3 examines the structural changes of ammonia borane (NH_3BH_3) at high pressure. We found that the structure changes from the experimentally determined $Pmn2_1$ and $Cmc2_1$ to newly predicted *Ama*2 and $P2_1/m$ structures at around 6 and 24 GPa, respectively. We found that the new structures adopted an eclipsed conformation of the hydrogen atoms, as opposed to the staggered conformation found in the low pressure structures, which we attribute to dihydrogen bonds between borane molecules.

CHAPTER 2

PRESSURE-DRIVEN SUPPRESION OF THE JAHN-TELLER EFFECTS AND STRUCTURAL CHANGES IN CUPRIC OXIDE

2.1 Introduction

Multiferroics, materials with multiple ferroic properties such as ferroelectricity, ferromagnetics, ferroelasticity and ferrotoroidicity, present us with options for tuneable multifunctional devices, especially through those with both ferroelectric and ferromagnetic properties, by allowing for the manipulation of the electric properties of a material via magnetic fields [34, 35]. The multiferroic properties of cupric oxide (CuO) have been known for some time. As a type-II multiferroic, the ferroelectric phase of CuO occurs due to magnetic ordering, and so both the ferroelectric ordering temperature and the Néel magnetic ordering temperature (*ca.* 230 K) are the same. While at ambient pressure CuO has a stable ferroelectric phase over a small temperature range of 20 K, from 210 to 230 K, it has been suggested recently that at pressures from 20-40 GPa, the multiferroic phase becomes stable from 0 to 300 K, giving it the potential to be a room-temperature multiferroic material [36]. Moreover, CuO is a quasi-one-dimensional magnetic system closely related to the family of cuprate superconductors [37]. The

Cu-O vibrations in cuprate materials promote the pairing of electrons, which has been suggested as a way to facilitate phonon-mediated superconductivity.

CuO is known to have a monoclinic structure (space group *C*2/*c*) at ambient conditions [38]. This structure is a distorted form of the *Fm*-3*m* rock salt structure. In CuO, each Cu^{2+} cation has an unpaired electron ($3d^9$), which lifts the degeneracy of the e_g states and induces magnetic ordering. The interplay between the magnetic ordering and Jahn-Teller distortions thus stabilizes the electronic structure of CuO in a distorted lattice [39]. The high Néel temperature observed in CuO arises from strong superexchange interactions in cupric pairs via the non-magnetic oxygen. Under high pressure, these interactions are expected to be strengthened, as the atoms move closer to each other, making room-temperature multiferroicity possible [36]. High-pressure behaviors of CuO have been investigated by using various experimental techniques including Raman spectroscopy, electrical conductivity measurement, neutron, and synchrotron X-ray diffractions [40-45]. Results obtained from the electrical conductivity measurements suggest that the *C*2/*c* structure is stable up to at least 70 GPa [40]. Structural refinements carried out at lower pressures, e.g., up to 47 GPa in X-ray diffractions, also confirmed the stability of the *C*2/*c* structure [44, 45]. Above the studied pressure range, however, there is little knowledge of possible structural phase changes.

Previous first-principles calculations [40] suggest that the structural phase transition of CuO may occur near 100 GPa, where the thermal activation barrier vanishes. As suggested, the effect of external pressure is to suppress the Jahn-Teller effects and drive the Cu^{2+} center back to a symmetrical coordination [46]. Applying this mechanism to CuO, we hypothesize that the *C*2/*c* structure will transform to the *Fm*-3*m* structure at a sufficiently high pressure. Another consideration is the electron back-transfer from the anions to cations at high pressure [47], such

that the occupancy of the Cu *d* shell changes, modifying the magnetic ordering and stacking pattern.

Here, we report a theoretical study on high-pressure structures of CuO based on density functional calculations. Two new structures, the rocksalt-type (*Fm*-3*m*) and CsCl-type (*Pm*-3*m*), are predicted as stable phases under high pressure. Transition from the *C*2/*c* structure to *Fm*-3*m* is predicted to occur near 72 GPa. This transition can be explained by a reduction of Jahn-Teller distortions in the *C*2/*c* structure as well as the pressure-induced stabilization of the *Fm*-3*m* structure. The transition from *Fm*-3*m* to B2 is rather sluggish over a large pressure range of about 210 GPa. The onset of the transition is predicted to occur near 190 GPa via an intermediate *R*-3*m* structure which completely transforms to the B2 structure with a ferromagnetic ground state near 400 GPa. At high pressure, the *p*V work exerted on the unit cell predominates the Jahn-Teller distortions and thus CuO retains the cubic forms.

2.2 Methods

To determine the equation of state of CuO, we performed density functional calculations of the ground state energy using VASP [32] on a number of different crystal structures; in addition to the experimentally determined monoclinic *C*2/*c* phase, *Fm*-3*m* (rocksalt), *Pm*-3*m* (CsCl), *F*-43*m* (zincblende), $P6_3mc$ (wurtzite), $P2_1/c$ (AgO) and $P4_2/mmc$ (PdO) structures were also calculated. Candidate structures were chosen based on structural analogies of CuO to other transition metal oxides, as well as on similar ratios of anion to cation radii as for free cupric and oxide ions, in the case of *Fm*-3*m* and *Pm*-3*m*, similar coordination numbers (CN) to the monoclinic phase, for *F*-43*m*, $P6_3mc$ and the PdO-like $P4_2/mmc$ structure,

and the homologue rule for the AgO-like $P2_1/c$ structure [48]. The low-energy structures obtained were cross-checked using the *ab initio* random structure searching (AIRSS) methods [49]. These calculations were performed for paramagnetic as well as ferromagnetic and antiferromagnetic spin orderings. We used projector-augmented planewave (PAW) potentials [31] with the PBE exchange-correlation functional [20]. For the paramagnetic calculations, a 16×16×16 *k*-point mesh [25] was used for the BZ sampling for accurate calculations of each crystal structure. For the spin-ordered structures, a larger 2×2×2 supercell was used, with a smaller *k*-point mesh of 4×4×4. All crystal structures were optimized until the Hellmann−Feynman forces on each atom became lower than 1 meV/Å. The electronic self-consistency loop calculations were performed until the total energy change between two steps were less than 10^{-4} eV. The effects of electron correlations beyond the density functional approximation on the Cu *d* shell were taken into account by employing the DFT+U method in a simplified rotationally invariant approach [14]. To match the structural parameters and the band gap (1.4 eV) for the monoclinic phase at ambient pressure to the experimental results, we applied L(S)DA+U corrections [13], with U_{eff} (U_{eff} = U−J) = 6.5 eV [36]. The same U parameters were used in all the structures, in order to enable direct-comparison between the calculated enthalpies. Mechanical and dynamical stability of the predicted structures was determined by phonon calculations using a finite displacement approach through a combination of VASP and PHON [33] programs. For these calculations, we used U = 10 eV and J = 1 eV for the L(S)DA+U corrections [13, 39], as well as PAW potentials with the PBESol [14, 21] exchange-correlation functional, and an energy cut-off of 520 eV, in order to match expected phonon dispersion patterns of the undistorted *Fm*-3*m* structure[39]. These calculations were done with supercells of up to 128 atoms and 4×4×4 *k*-point meshes to obtain accurate interatomic forces. For each

structure, 200 pressures were tested, from ambient pressures up to *ca.* 600 GPa, in order to accurately analyze the enthalpy curve. X-ray absorption near edge structures (XANES) of CuO were calculated using the *ab initio* FDMNES code based on the finite difference method [50]. Experimental XANES data measured at the HXMA beamline at the Canadian Light Source from the mineral tenorite was used to benchmark the calculations. The cluster's radius, core-hole width, spectral width of the final state, and arctangent function were optimized until the calculated XANES of the monoclinic structure matched the experimental data. Optimized parameters were then used for all other structures at high pressures.

2.3 Results and Discussion

The initial equation of state calculations were performed without magnetic ordering taken into account, as an attempt to narrow the possibilities for structures at higher pressures. At ambient pressure, the *C*2/*c* structure is observed experimentally, and was found to have the lowest energy among the examined structures, though the AgO-type $P2_1/c$ and PdO-type $P4_2/mmc$ structures have similar energies (Fig. 2-1a).

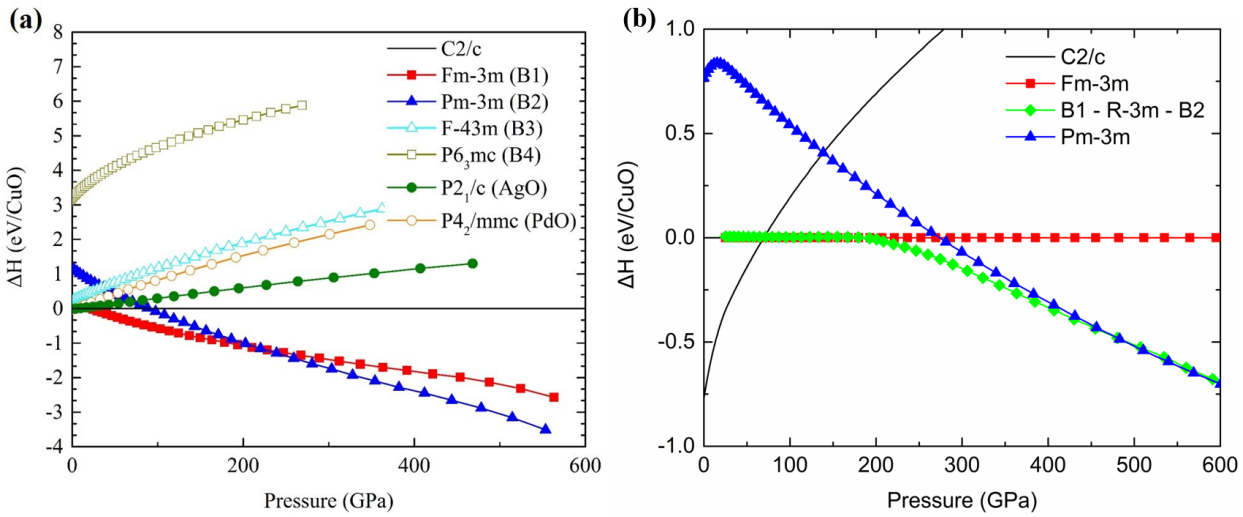

Figure 2-1. (a) Non spin-polarized and (b) spin-polarized pressure dependencies of enthalpies for candidate structures of CuO. The enthalpies of the experimentally observed *C*2/*c* structure and the *Fm*-3*m* structure are used as the zero-energy reference in (a) and (b), respectively [30].

As the pressure was increased, the *F*-43*m*, B4, $P2_1/c$ and $P4_2/mmc$ structures were found to be not energetically competitive, and thus were not considered further. The *Fm*-3*m* and *Pm*-3*m* structures, on the other hand, became more energetically favored. The transition from the *C*2/*c* structure to *Fm*-3*m* occurs near 25 GPa, and the *Fm*-3*m* to *Pm*-3*m* transition near 240 GPa. The mechanical and dynamical stability of the *Fm*-3*m* and *Pm*-3*m* structures were established from phonon calculations which revealed no imaginary frequencies (Figs. 2-2a and 2-2b). The pressure-driven *Fm*-3*m*–*Pm*-3*m* transition, as predicted here, has been previously observed or proposed in many other transition metal oxides, for example, CdO, ZnO, and FeO [51-54].

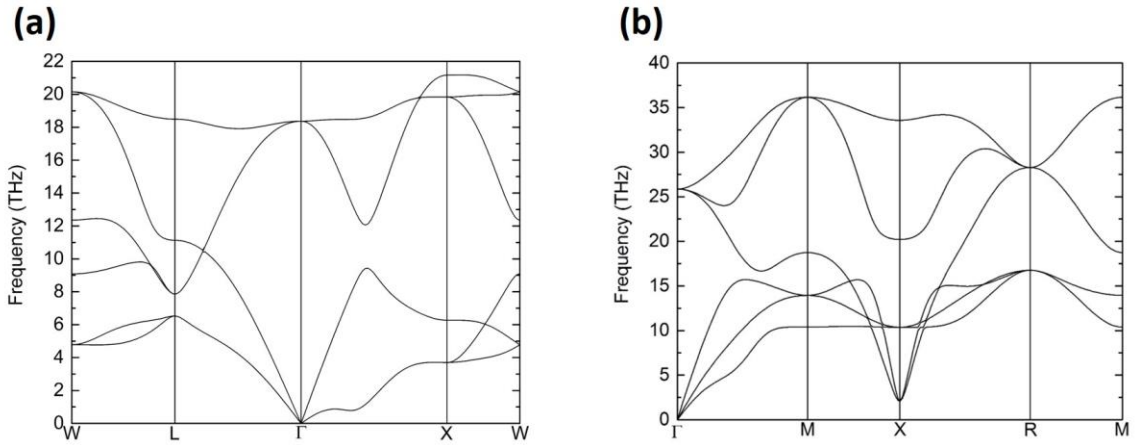

Figure 2-2. Calculated phonon dispersion patterns for (a) the net zero magnetic moment *Fm*-3*m* structure at 80 GPa and (b) the ferromagnetic *Pm*-3*m* structure at 600 GPa [30].

In order to best represent the electronic structures of CuO, the spin-ordering of the cupric ions was then considered. For the *C*2/*c* phase, the magnetic structure below the Néel temperature is known experimentally to be antiferromagnetic (AF1) at ambient pressure and high pressures up to at least 1.8 GPa [45, 55]. First principles calculations [36] further suggested that the range of stability of the AF1 phase may be extended to the Mbar region. This spin-ordered structure, as shown in Fig. 2-3a, consists of Cu unpaired spins arranged antiferromagnetically along the [10-1] direction and ferromagnetically along the [101] direction, with the [010] direction as the easy axis. The magnetic moments in the (010) planes are coupled by four superexchange interactions, J_x, J_z, J_{2a}, and J_{2b}, whereas adjacent planes are coupled by four interactions, J_a, J_b, J_c, and J_d [56]. We have examined the AF1 and other spin configurations including ferromagnetic and paramagnetic orderings for the *C*2/*c* structure and found the AF1 structure as the ground state, which is consistent with experimental results [55].

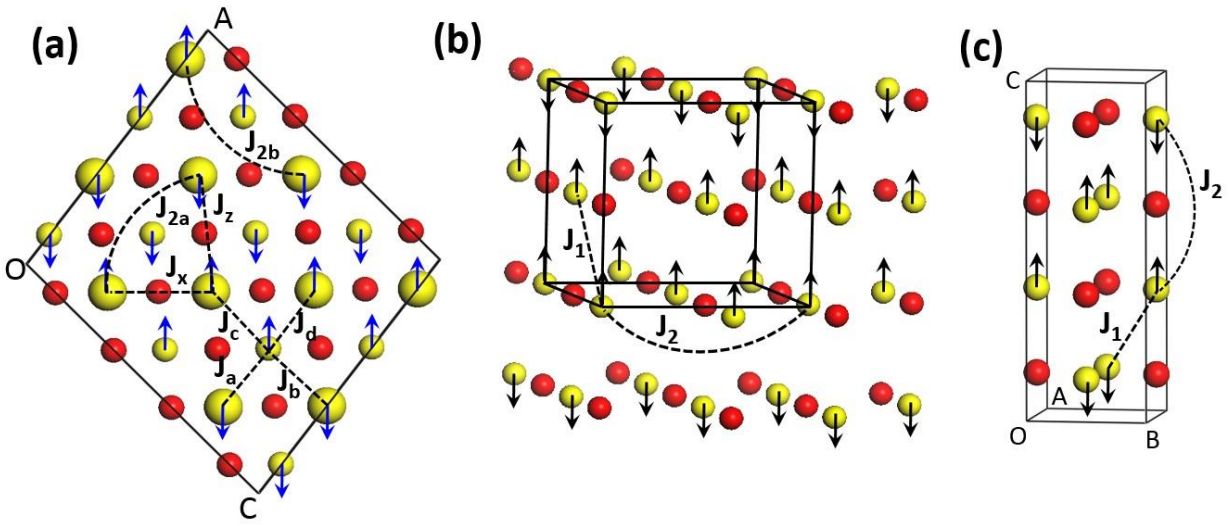

Figure 2-3. (a) Schematic view of the antiferromagnetic (AF1) state of the *C*2/*c* structure as observed experimentally. (b) The same magnetic state in an undistorted *Fm*-3*m* structure and its magnetic unit cell (c). The Cu and O atoms are colored yellow and red, respectively. In (a), Cu atoms belonging to different constant-y planes are separated by their sizes, big (y = 0) and small (y = 0.5). The Cu magnetic moment orientations are shown by arrows. Nearest-neighbor and next-nearest-neighbor interactions are indicated by dotted lines and curves, respectively [30].

For the *Fm*-3*m* and *Pm*-3*m* structures, ferromagnetic, antiferromagnetic and paramagnetic structures were all tested. To determine the exchange interactions, we used the Heisenberg Hamiltonian, $H = \sum_{NN} J_1 \vec{S}_i \cdot \vec{S}_j + \sum_{NNN} J_2 \vec{S}_i \cdot \vec{S}_j$, and summed over all cupric pairs of the nearest (NN) and next-nearest neighbors (NNN) [57, 58]. All exchange interactions more distant than the next-nearest neighbors are much weaker, and therefore were not included in these calculations. Figure 2-3b shows an example for the *Fm*-3*m* structure, where the spins are arranged in the antiferromagnetic state similar to that of the *C*2/*c* structure. The magnetic unit cell (Fig. 2-3c) of this state has a *P*4/*nmm* space group, reduced from the non-magnetic space group of *Fm*-3*m*. The exchange coupling constants J_1 and J_2 in the *Fm*-3*m* and *Pm*-3*m* structures were calculated from the total energy differences of three magnetic configurations. The first

configuration is simply the ferromagnetic configuration where all unpaired spins are parallel (Figs. 2-4a and 2-4e). The second configuration has ferromagnetic ordering on the (001) planes and antiferromagnetic ordering along the [001] direction (Figs. 2-4b and 2-4f). The third configuration has ferromagnetic ordering on the (111) planes and antiferromagnetic ordering along the [111] direction, similar to CoO for the *Fm*-3*m* structure [59] (Figs. 2-4c and 2-4g). For the *Fm*-3*m* structure, a fourth magnetic configuration was also calculated which is ferromagnetic in the (011) planes and antiferromagnetic in the [011] direction, alternating every second plane [39] (Fig. 2-4d).

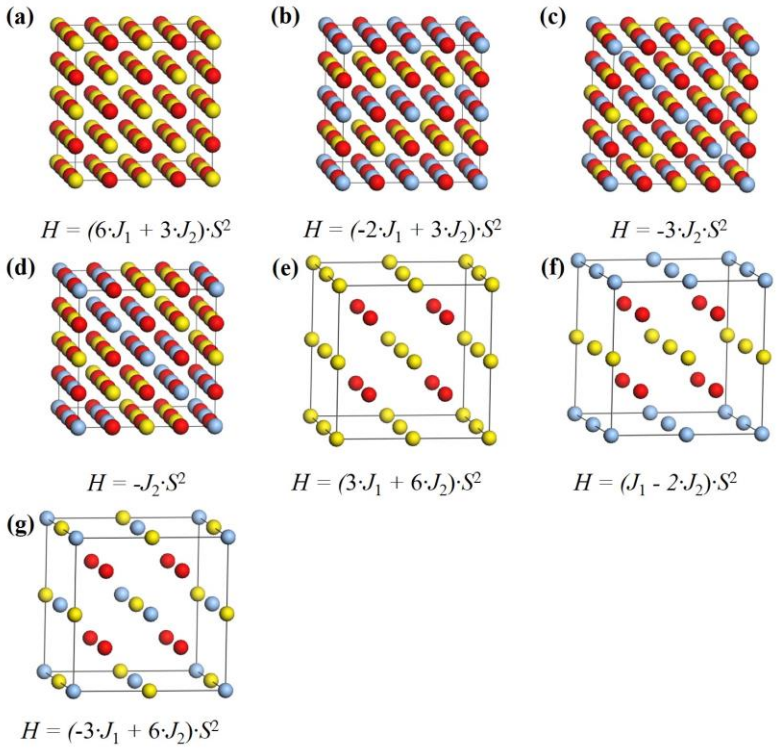

Figure 2-4. Magnetic structures and Heisenberg Hamiltonians for the *Fm*-3*m* structure in the (a) ferromagnetic structure and the antiferromagnetic structures which are (b) ferromagnetic in the (100) planes and antiferromagnetic in the [100] direction, (c) ferromagnetic in the (111) planes and antiferromagnetic in the [111] direction and (d) ferromagnetic in the (011) planes and antiferromagnetic in the [011] direction every other plane, as well as the *Pm*-3*m* structure in the (e) ferromagnetic structure and the antiferromagnetic structures which are (f) ferromagnetic in the (100) planes and antiferromagnetic in the [100] direction and (g) ferromagnetic in the (111) planes and antiferromagnetic in the [111] direction. Yellow spheres are spin up Cu sites, blue spheres are spin down Cu sites and red spheres are O sites [30].

For the *Fm*-3*m* structure, it was found that when an antiferromagnetic arrangement was used as the initial structure, the final structure would instead relax to a non-magnetic orientation with vanished magnetic moment on the Cu sites. This can be explained by a charge back-transfer from the O ion to the Cu ion in the *Fm*-3*m* structure, resulting in the Cu ion having only paired electrons in 3*d*-shell. Such charge back-transfer at high-pressure makes the CuO behave like CdO (in the $3d^{10}$ state), which indeed favors the *Fm*-3*m* structure, and also explains, in part, the fact that CuO does not have a metallic band-structure [60]. When the antiferromagnetic ordering was instead enforced throughout the calculation, the electronic structure would not converge, suggesting that the undistorted antiferromagnetic *Fm*-3*m* structure is not a likely candidate for the ground-state structure. Between the ferromagnetic, paramagnetic and non-magnetic *Fm*-3*m* structures, we found the ferromagnetic structure was marginally more thermodynamically stable (by *ca*. 28 meV/CuO), though mechanically and dynamically unstable at pressures up to and including the pressure range in which it was found to be energetically favorable when calculating phonon dispersions. The paramagnetic and charge back-transfer non-magnetic structures had virtually identical energies when compared to each other (Fig. 2-5), and phonon calculations of the net zero magnetic moment *Fm*-3*m* structure revealed it to be mechanically and dynamically stable above 20 GPa (Fig. 2-2b), suggesting a net zero magnetic moment ground state.

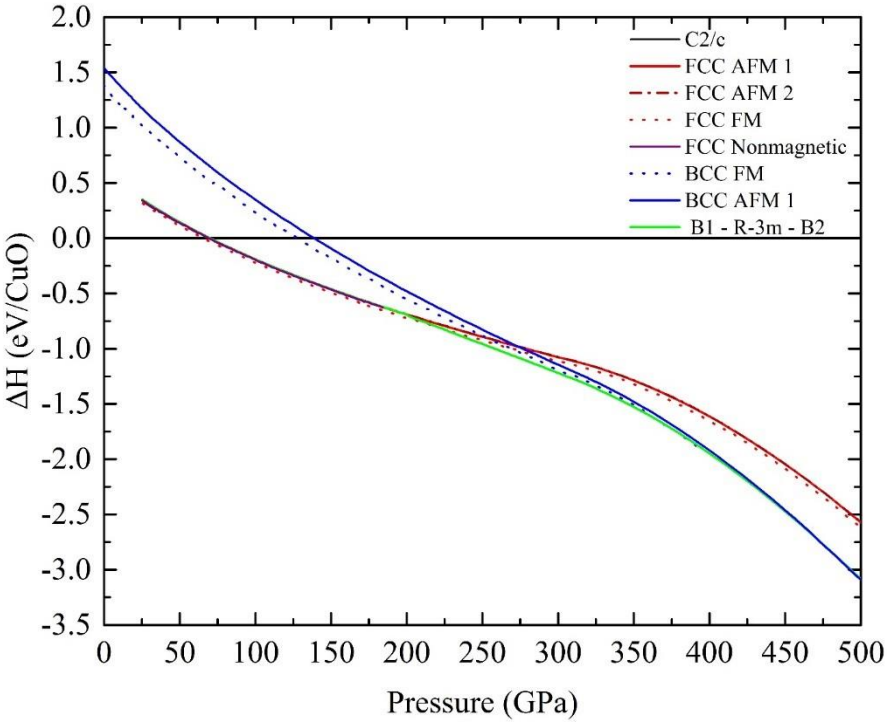

Figure 2-5. Equation of state for tested magnetic CuO structures. AFM 1 refers to a cubic structure with ferromagnetic ordering in the (111) planes and antiferromagnetic ordering in the [111] direction, alternating every plane, similar to the ordering in rocksalt CoO. AFM 2 refers to a structure with ferromagnetic ordering in the (011) planes and antiferromagnetic ordering in the [011] direction, alternating every second plane [30].

For the *Pm*-3*m* structure, on the other hand, both J_1 and J_2 were calculated to be negative (Fig. 2-6), suggesting a ferromagnetic ground state. These exchange coupling constants were determined using the Heisenberg Hamiltonians (*H*) of the magnetic *Pm*-3*m* structures in the equation $E^{Structure} = E_0 + H$, where $E^{Structure}$ is the total relaxed energy of the structure and E_0 is the ground state energy, and solving for J_1 and J_2. As both J_1 and J_2 are found to be negative, the ferromagnetic configuration is considered to be the ground state for this structure. It should be noted here that this approach [61] is semi-empirical. The magnitude of the cation spin, *S*, was assumed constant in all magnetic states, and we assumed J_1 and J_2 were the same in all considered magnetic configurations. The J_1 and J_2 values were derived from the expressions in Figs. 2-4e to 2-4g. The ferromagnetic *Pm*-3*m* structure has also been previously suggested for

FeO at high pressure [62]. An explanation is that the *Pm*-3*m* structure lacks linear superexchange interactions and therefore the energy is not sensitive to the spin ordering [63]. It should be noted here that the energy differences between different magnetic orderings are sometimes in the neighborhood of a few meV, which approaches the limit of accuracy of the DFT methods. The lowest-energy magnetic ordering suggested here, therefore, only represents a possible solution, which does not eliminate the possibility that other magnetic orderings may also exist.

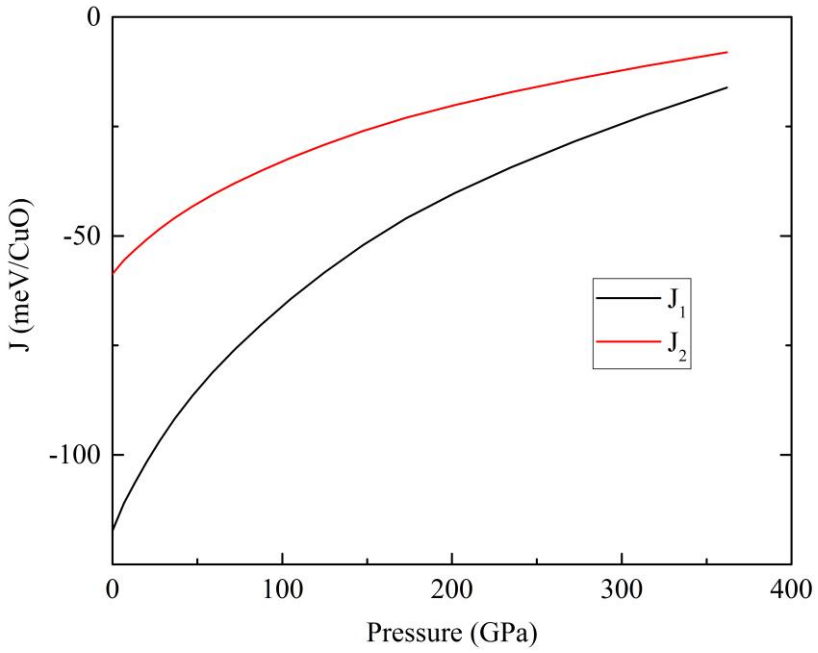

Figure 2-6. Calculations of exchange coupling constants for *Pm*-3*m* structure at different pressures [30].

Using the determined magnetic ordering for each structure, we repeated the equation of state calculations for CuO (Fig. 2-1b). Once again, the experimentally determined *C*2/*c* structure was found to be the most favorable at lower pressures. The *C*2/*c* → *Fm*-3*m* → *Pm*-3*m* transition sequence is retained in the magnetic-ordered calculation, however the pressures for the two transitions are increased. The *C*2/*c* to *Fm*-3*m* transition now occurs near 72 GPa. The *Fm*-3*m* to *Pm*-3*m* transition (Figs. 2-7b to 2-7d) is sluggish in nature.

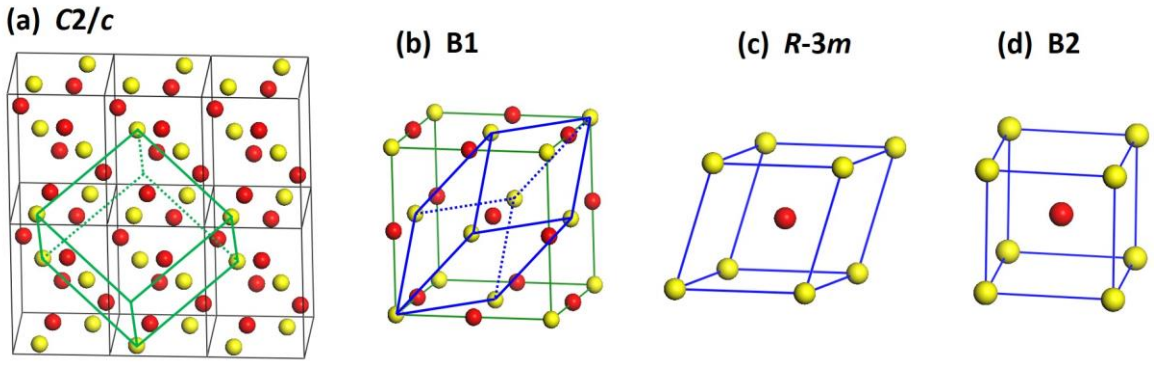

Figure 2-7. Proposed transition pathway for the *C*2/*c* (a) → *Fm*-3*m* (b) → *Pm*-3*m* (d) transition with the *R*-3*m* structure (c) as the intermediate phase between *Fm*-3*m* and *Pm*-3*m*. The face-centered cubic cell (green) of the *Fm*-3*m* structure is evolved from the *C*2/*c* structure. The primitive cell of the *Fm*-3*m* structure (blue) continuously increases its rhombohedral angle (60º) through a reduction of its body diagonal and becomes the body-centered cubic cell once the angle reaches 90º. The Cu and O atoms are colored yellow and red, respectively [30].

The onset of this transition is near 190 GPa and the transition is complete at 400 GPa. Along a large pressure range of 210 GPa, an *R*-3*m* intermediate structure, initially the primitive *Fm*-3*m* structure, is continuously compressed along its body diagonal and becomes the *Pm*-3*m* structure once its rhombohedral angle increases to 90º (Figs. 2-7a to 2-7d). In this pressure range, the *R*-3*m* structure has slightly lower enthalpy (up to *ca.* 100 meV/CuO) than the two parent structures (Fig. 2-1b). To this end, we therefore suggest that the *Fm*-3*m* to *Pm*-3*m* transition in CuO is indirect and perhaps occurs with a large pressure hysteresis. The *R*-3*m* intermediate structure is consistent with the Buerger path for the *Fm*-3*m* to *Pm*-3*m* transition [64]. We have also searched for other intermediate structures in this pressure range using the AIRSS structure search method [49] but no other structures were found to be energetically more competitive. Other transition mechanisms for the *Fm*-3*m* to *Pm*-3*m* transition, for example as suggested in Refs. 65-67, may lead to lower energy paths but yield no stable intermediate structures. It should also be noted, that in the L(S)DA +U approach (Fig. 2-1b), the *Fm*-3*m* to *Pm*-3*m* transition pressure was

calculated to be higher than the value obtained in non-magnetic DFT method (Fig. 2-1a), which seems to contradict to what one would expect from the inclusion of magnetic ordering. The transition pressure in the L(S)DA+U calculation is sensitive to the value of U_{eff}. We used the same U_{eff} value [36] for all structures in order to compare their energies on the same footing. Thus, the relation between the DFT and the L(S)DA+U calculations would not be exactly the same, such that the calculated transition pressures are not the same in the two approaches. These types of indirect phase transitions are common in transition metal oxides in which the electronic and spin degrees of freedom are strongly coupled with the lattices, and the interplay of these two mechanisms determines the phase stability (CdO is an exception, where Cd behaves like a main group element [62]). In contrast, the pressure-driven *Fm*-3*m* to *Pm*-3*m* transitions in main group compounds, i.e., alkali and ammonium halides, are usually direct, which can be explained by a closed-shell sphere model where the pressure-induced stacking change dominates the transition [68].

It is not surprising that the magnetic-ordering delays the *C*2/*c* to *Fm*-3*m* phase transition. The *C*2/*c* structure observed experimentally at lower pressures is stabilized by two mechanisms, the superexchange interactions between unpaired spins (Fig. 2-3a), and the Jahn-Teller distortions from orbital coupling (Fig. 2-8).

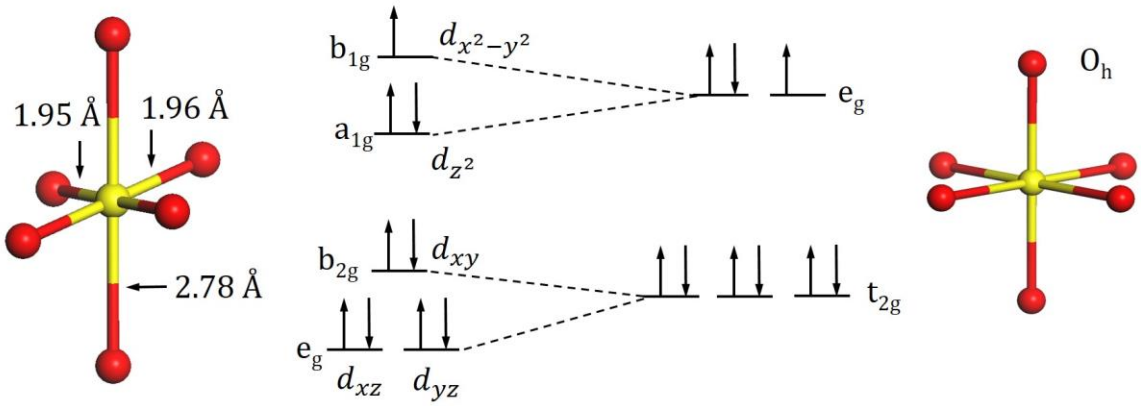

Figure 2-8. Prototypical octahedral distortions at a Cu site in CuO. In an undistorted *Fm*-3*m* structure, the Cu atom has an octahedral geometry (right) with energy degenerated e_g and t_{2g} states. In the *C*2/*c* structure, two apical Cu-O bonds are elongated (left), lifting the energy degeneracy and reducing the geometry to a distorted square-planar configuration. The energy splitting between different levels is for demonstration only, and is not plotted to scale [30].

In the non spin-ordered calculations, the stabilization from the superexchanges is absent so that the *p*V work can more effectively suppress the Jahn-Teller distortions. In this case, the *C*2/*c* to *Fm*-3*m* phase transition is entirely electrostatic and occurs at a lower pressure. As demonstrated in Fig. 2-8, the Jahn-Teller effects elongate two Cu-O bonds at the Cu site, reducing the otherwise octahedral geometry (O_h) to a distorted square-planar configuration. At ambient pressure, the two elongated Cu-O bonds in the *C*2/*c* structure are 2.78 Å, substantially longer than the other four, *ca.* 1.96 Å. The Jahn-Teller elongation along one four-fold axis is characteristic for d^9 cupric ions, as previously observed in many octahedral Cu^{2+} complexes. This distortion therefore lifts the degeneracy of the e_g states at the Cu site, where the doubly occupied a_{1g} state (d_z^2) is stabilized over the half occupied b_{1g} state ($d_{x^2-y^2}$). Moreover, the d_z^2 state is (slightly) further stabilized by mixing with Cu *s* state of the same a_{1g} symmetry. Thus, there is a net reduction in the total energy upon the Jahn-Teller elongation. At lower pressures, this distortion is reflected as a soft phonon mode at the *L* symmetry point in the Brillouin zone (Fig. 2-2a). In our calculations, we found that all spin-ordered configurations of the *Fm*-3*m*

structure showed soft phonon modes at ambient pressure. The *Fm*-3*m* structure is distorted at low pressures due to the Jahn-Teller effects, which, together with the antiferromagnetic interactions, leads to a stable *C*2/*c* structure [55]. At higher pressures, however, the *p*V work of the enthalpy is able to overcome the instability of the splitting energy, reverting to a stabilized *Fm*-3*m* structure with degenerated e_g and t_{2g} states. Similar pressure-driven suppression of Jahn-Teller distortions has been observed previously in other Cu^{2+} compounds [68, 69]. At high pressures, bond shortening occurs in all Cu-O bonds in CuO but it is more pronounced in longer (weaker) bonds which lead to a phase change once the atoms are sufficiently close to each other [69]. It is also expected that the change of structure of CuO under high pressure will affect the polarization, P, which is an important component for potential multiferroic applications [36]. A complete investigation of these properties is beyond the scope of the present study, but should be considered for future research.

To provide guidance for future experiments to test our prediction, we calculated the expected X-ray diffraction (XRD) patterns and the XANES for the high-pressure structures of CuO. To obtain suitable parameters for the XANES simulations, we measured the XANES of CuO (mineral tenorite) at ambient pressure at the HXMA beamline at the Canadian Light Source and used it as a benchmark to optimize the parameters. For the purpose of comparison, the simulations for all CuO structures adopted the same molar volume; one shall then expect the measured XRD/XANES to shift to higher angles/energies due to the strengthening of the bonding at high pressures. The XRD patterns were simulated [70] using the structure factors of the optimized CuO structures and indexed with the interplanar spacing (d_{hkl}) (Fig. 2-9a). Simulated XRD patterns reveal distinct differences in the *C*2/*c*, *Fm*-3*m* and *Pm*-3*m* structures,

which should be sufficient for structural identification. Calculated XANES spectra also revealed clear changes along the phase transitions (Fig. 2-9b).

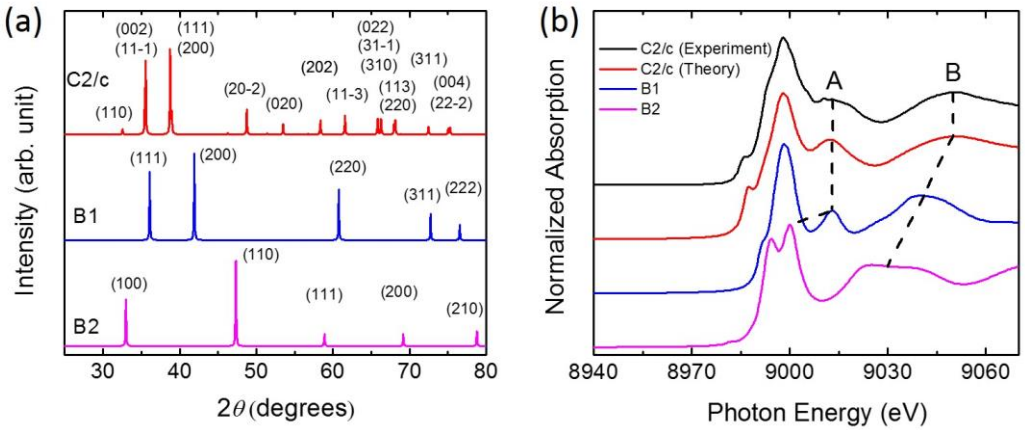

Figure 2-9. (a) Simulated X-ray powder diffraction patterns for candidate structures of CuO using a wavelength of 1.54 Å (Cu–Kα). (b) Experimental and simulated XANES spectra for candidate structures of CuO. Experimental molar volume of CuO at ambient pressure has been used in all simulations. Figure produced by N. Chen [30].

The two characteristic XANES features (A and B) have moderate changes along the transition from *C*2/*c* to *Fm*-3*m*, which is associated with the suppression of the Jahn-Teller distortions. The changes of XANES in the *Fm*-3*m* to *Pm*-3*m* transition, on the other hand, are more prominent and reveal clear changes in first-shell Cu-O coordination, and in outer-shell Cu-Cu coordination. Considering that the XANES feature B already extends into the extended X-ray absorption fine structure (EXAFS) region, a complimentary EXAFS modeling was performed by using the FEFF7 program [71] with identical clusters, revealing corresponding changes in peak positions and line shape in *k*-space along the phase transitions, supporting the XANES results.

2.4 Barium Chloride: Further Analysis and Explanations

Since the time of the completion of the project with CuO and its publication in the Journal of Physics: Condensed Matter, I was involved in another project investigating BaCl, currently accepted for publication in Physical Review B. As the results and analysis found in that project are relevant to the results obtained in this project with CuO, the discussion on BaCl will also be included here.

2.4.1 BaCl: Introduction

The application of pressure can induce extraordinary changes in the electronic properties of both elements and simple compounds. For example, at high pressures alkali metals can acquire unusual transition metal properties, like the conversion of potassium from a conventional alkali metal to one with transition metal properties via the *s* to *d* electron transition [72]. Another example is Cs, which shows s to d electron transfer at ~3 GPa, and it is expected that this may be a general phenomenon in other elemental metals [73]. If such a transition occurs, it is likely that interesting new properties could be exhibited such as magnetism and superconductivity, promoted by increased *d*-electron concentration [74]. It has been suggested that barium, which is an alkaline earth metal, exhibits an *s* to *d* transfer of electrons that plays a crucial role in the formation of complex incommensurate structures at high pressure [75, 76].

The question of whether barium compounds can also exhibit this type of behavior under high pressure is therefore interesting. Barium chloride ($BaCl_2$), for example, is a compound with two crystalline forms, cotunnite and fluorite. There is a possibility that unconventional BaCl may

also be a stable compound with the rocksalt (*Fm*-3*m*) structure [77] and that this form could be a natural result of β^- radioactive decay of ^{137}CsCl. The possibility of the existence of BaCl raises immediate questions about its electronic structure and properties and the possibility of other stable structures of BaCl that may show transition metal behavior similar to elemental Ba. Such apparent change in the oxidation state of Ba may show either interesting magnetic structures or superconducting properties exhibited in transition metals. In this study, we therefore explored this possibility using first-principles methods and predict stability, superconductivity, and magnetic structures exhibiting half-metallic features.

2.4.2 BaCl: Methods

Structure searches were performed using the AIRSS method [49] with primitive cells containing up to four BaCl units. Electronic structure calculations were performed using VASP [32]. PAW potentials [31] with a PBE functional [20] were used, with $5s^2 5p^6 6s^2$ for Ba and $3s^2 3p^5$ for Cl treated as valence states. Magnetic structures were calculated using the HSE hybrid functional [22] and VASP, with a mixing of 25% of the exact Hartree-Fock exchange to 75% of the LDA exchange. Dense *k*-point meshes were chosen to converge the total energy to within 1 meV/atom. The band structure and *lm*-decomposed density of states (DOS) were calculated using the Quantum ESPRESSO program [78].

2.4.3 BaCl: Results and Discussion

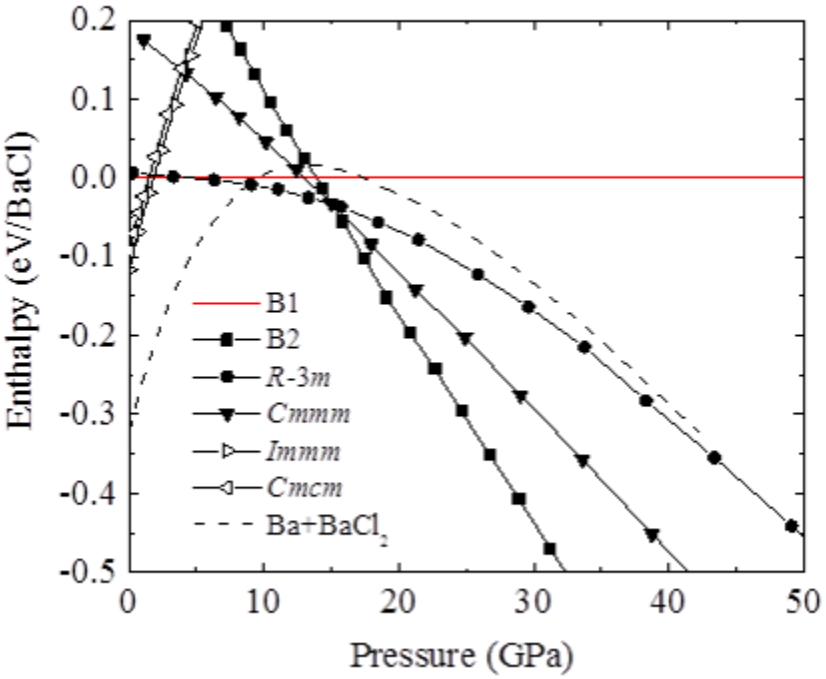

Figure 2-10. Pressure dependences of enthalpies for different structures with the *Fm*-3*m* structure as the zero-enthalpy reference. Figure produced by Y. Yao.

A stable BaCl compound has previously been suggested to have the *Fm*-3*m* structure via radioactive decay [77] but it was also noted, since Ba is divalent, that it may not be synthesized in conventional solid-state methods. Here we suggest that it is possible to produce BaCl by compressing solid $BaCl_2$ and Ba at high pressure. Calculated enthalpies of the predicted BaCl structures are compared to the solid mixture of Ba and $BaCl_2$ in Fig. 2-10. At low pressures, the solid mixture is thermodynamically stable, indicating that a system of Ba and Cl should stay in the $BaCl_2$ form. At ~9 GPa, however, the BaCl solid becomes more stable than the solid mixture which signifies the viability of the $Ba+BaCl_2 \rightarrow 2BaCl$ reaction at high pressure. As the *Fm*-3*m* structure becomes energetically favored, it undergoes a transition to the *Pm*-3*m* structure via an

intermediate *R*-3*m* structure along the Buerger path. Above 15 GPa, the *Pm*-3*m* structure is the lowest enthalpy structure of the BaCl. Calculated phonon dispersion relations suggest all three structures of BaCl are mechanically and dynamically stable at high-pressure (Figs. 2-11a to 2-11c).

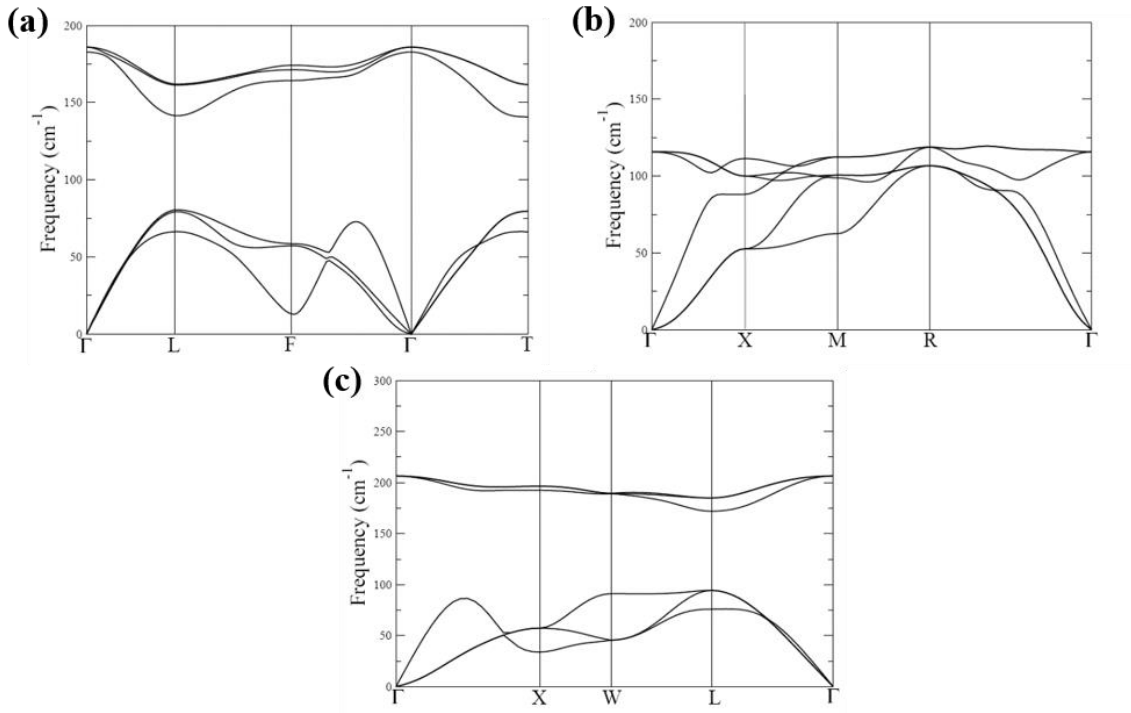

Figure 2-11. Calculated phonon dispersion relations for (a) *R*-3*m* BaCl at 1.4 GPa (b) *Pm*-3*m* BaCl at P = 0 GPa and (c) *Fm*-3*m* BaCl at 2.84 GPa. Note Phonon dispersion relations for the *Fm*-3*m* structure also indicate stability at P= 0 GPa but required single point calculation near and at the X point to obtain stability. Figure produced by D. D. Klug.

Most significantly, the high-pressure *Pm*-3*m* structure is also predicted to be mechanically and dynamically stable at ambient pressure (Fig. 2-11b). The *Pm*-3*m* structure therefore would be formed at high pressure, where it is thermodynamically stable, and may be quench recovered to ambient conditions due to the high kinetic stability. The *Fm*-3*m* structure has been previously calculated to be stable at low pressure [77] and was verified here. It is important to note that CsCl has the same *Pm*-3*m* structure. If BaCl is produced from the radioactive decay of ^{137}CsCl,

then the *Pm*-3*m* structure will likely be maintained. This finding is particularly critical to the research of spent nuclear fuel reprocessing, as the radioparagenesis of CsCl to BaCl has been suggested as one approach to eliminate ^{137}Cs in fission wastes.

The formation of BaCl is very unusual and seems to violate the 'octet rule' as Ba has one more electron than Cs. If BaCl forms the same structure as CsCl, an obvious question to address is where this extra electron resides. The Pauli Exclusion Principle states that this electron needs to occupy empty quantum states, either on the Ba 5*d* orbitals or in the interstitial voids. It is well known that when alkaline earth metals are compressed, the valence electrons can migrate to the interstitial voids driven by Coulombic repulsions. Known as interstitial quasi-atoms (ISQs) [79], electrons in the interstitial space form quantized states, and interact with the environment in the same way as a new atom. In BaCl, however, the ISQs were not formed. The calculated charge distributions showed that the electrons in BaCl are still localized to the atomic sites (Figs. 2-12a and 2-12b).

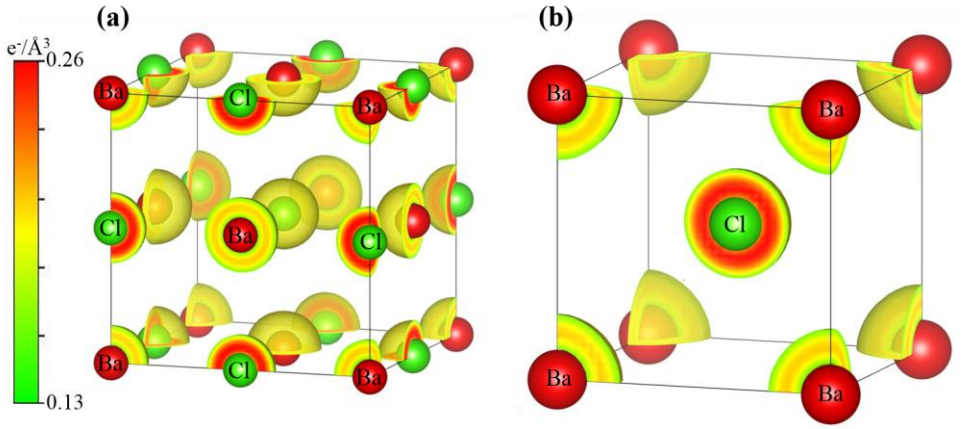

Figure 2-12. Total charge density of (a) *Fm*-3*m* structure and (b) *Pm*-3*m* structure, both at ambient pressure. The colour scale applies to both charge densities. The charge density of the chlorine site in (b) has been cut along the (100) plane for clearer presentation of the changes in charge density.

Specifically, the extra electron in BaCl is found in the Ba 5*d* orbital which is energetically more favorable than the ISQ orbitals. This *s* to *d* transition is clearly revealed from the projected density of states (pDOS) for the *Fm*-3*m* and *Pm*-3*m* structures at ambient pressure (Figs. 2-13a and 2-13b).

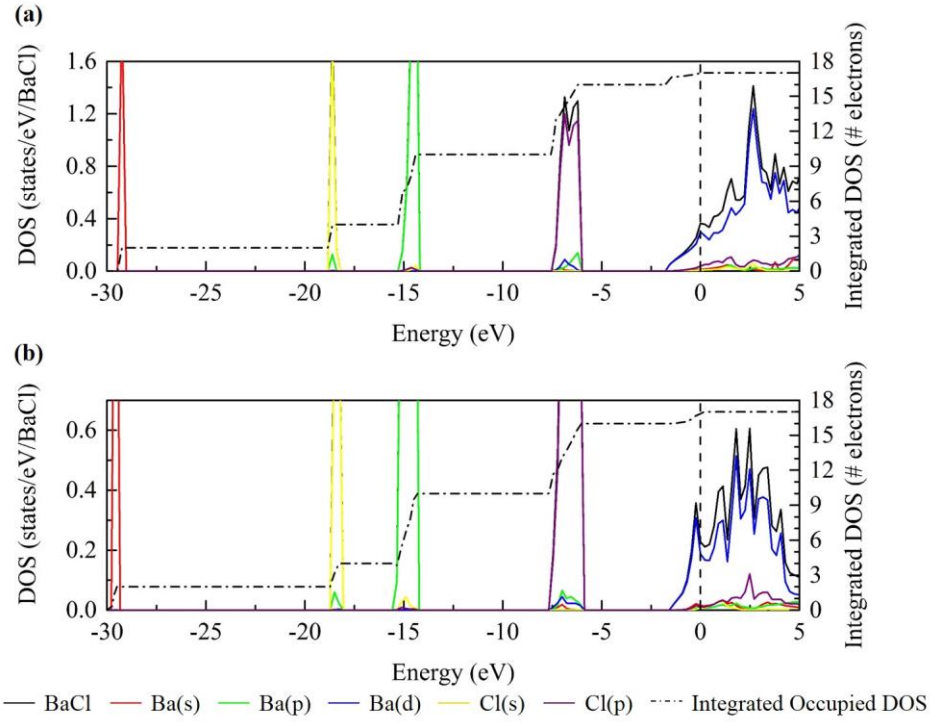

Figure 2-13. DOS, *l*-decomposed DOS and integrated occupied density of states at ambient pressure for (a) the *Fm*-3*m* structure and (b) the *Pm*-3*m* structure. The energy range was chosen to show all the occupied states from both the barium and chlorine sites, as well as the bands up to 5 eV above the Fermi level.

In the semi-core region, the pDOS are separated into four fully occupied subsets characteristic of Ba 5*s*, Cl 3*s*, Ba 5*p*, and Cl 3*p* states. The DOS around the Fermi level consists primarily of Ba 5*d* states with minor contributions from the semi-core states, forming a metallic ground state in BaCl. The Ba atoms therefore act as the charge carriers, and the 5*d* electrons as conduction electrons.

The band structure and *lm*-decomposed DOS near the Fermi level were calculated for the *Fm*-3*m* and *Pm*-3*m* structures (Figs. 2-14a and 2-14b).

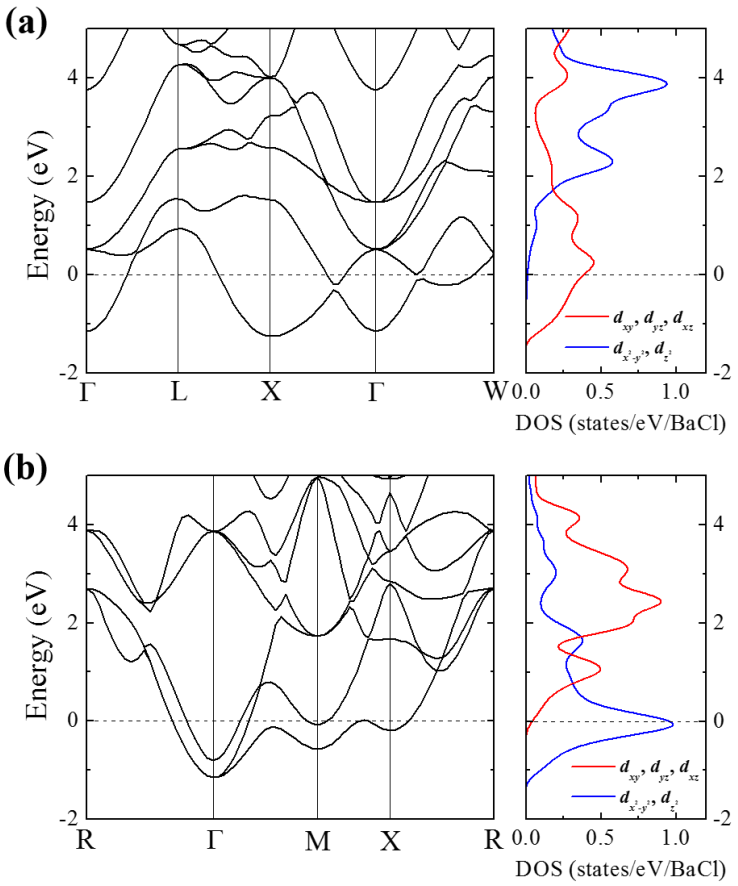

Figure 2-14. Electronic band structure and *lm*-decomposed DOS around the Fermi level of (a) the *Fm*-3*m* structure and (b) the *Pm*-3*m* structure at ambient pressure. Figure produced by Y. Yao.

The dominant electronic contribution from the Ba 5*d* orbitals clearly yields the t_{2g} and e_g states near the Fermi level. For the *Fm*-3*m* structure, the occupied bands below the Fermi level are in triply degenerate t_{2g} (d_{xy}, d_{xz} and d_{yz}) states, while the doubly degenerate e_g (d_{z^2} and $d_{x^2-y^2}$) states are essentially unoccupied. This energy splitting is clearly a response to the octahedral crystal field, and is also supported by the density distribution of the conduction electrons (Fig. 2-15a). The electrons will naturally reside in the t_{2g} orbitals (Fig. 2-15b), *i.e.*, in the off-axis directions, to

avoid unfavorable interactions with the Cl^- anions. This electron topology is reflected in the four-fold lobed structure in the charge density distribution. Conversely, in the *Pm*-3*m* structure (Fig. 2-14b) the electrons occupy primarily the e_g states below the Fermi level, while the t_{2g} states are mostly unoccupied. This arrangement is once again supported by the density distribution of the conduction electrons (Fig. 2-15c). To avoid unfavorable interactions with the Cl^- anions, the electrons occupy the on-axis areas, showing the four-fold lobed structure of the $d_{x^2-y^2}$ orbital (Fig. 2-15d), as well as the extended lobes of the d_{z^2} orbital (Fig. 2-15e).

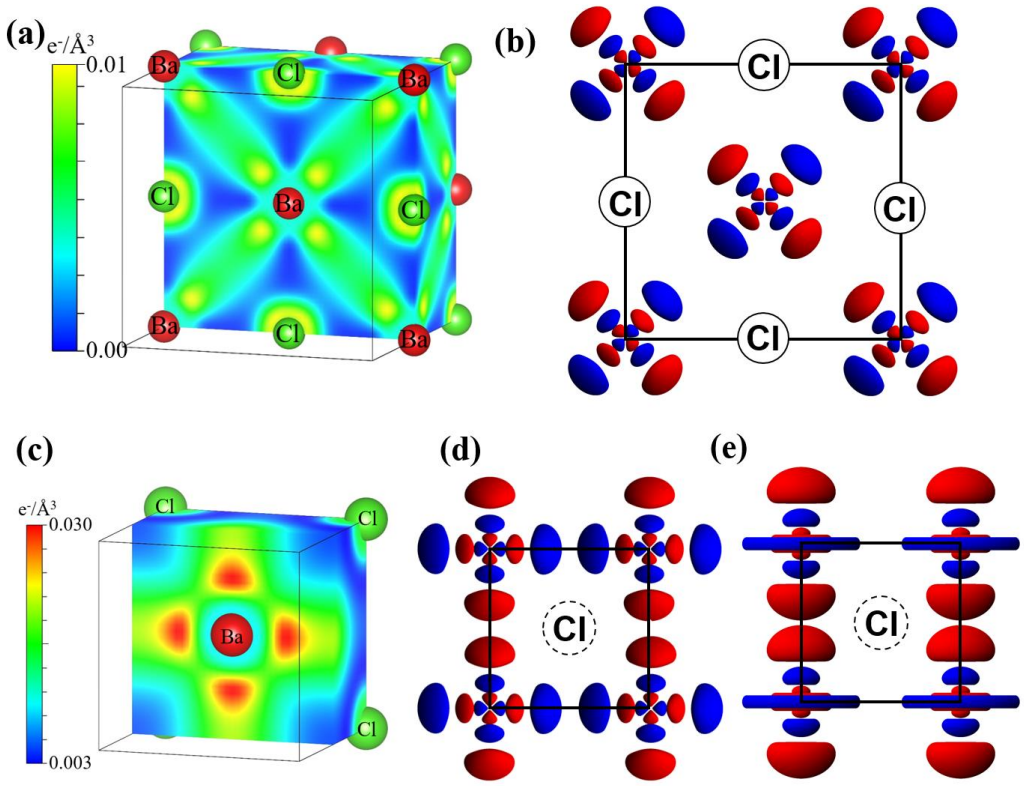

Figure 2-15. Charge density for electrons in the bands near the Fermi level of the (a) *Fm*-3*m* structure and the (c) *Pm*-3*m* structure at ambient pressure. Topology of (b) the t_{2g} orbitals in the *Fm*-3*m* structure, and (d) and (e) the e_g orbitals in the *Pm*-3*m* structure. Orbitals are for demonstration only, and are not plotted to scale. Figure produced by M. J. Greschner and Y. Yao.

The existence of an unpaired electron in BaCl raises interesting possibilities as to the magnetic properties. We examined different magnetic orderings for the *Fm*-3*m* and *Pm*-3*m*

structures and found both structures assume a ferromagnetic ground state. We have examined ferromagnetic, non-magnetic, and several antiferromagnetic ordering for the *Fm*-3*m* and *Pm*-3*m* structures. Six antiferromagnetic orderings, grouped into three sets, were examined for each structure type. For the three sets, ferromagnetic ordering is placed on the (100), (110), and (111) planes, respectively. In each set, two structures were constructed by arranging the ferromagnetic planes in antiferromagnetic ordering along the perpendicular direction by (1) alternating every plane or (2) alternating every second plane. In the GGA method, it was predicted that at ambient pressure the ferromagnetic ordering of the *Pm*-3*m* structure is more energetically favorable than the non-magnetic structure (by *ca.* 15 meV/BaCl), and the antiferromagnetic orderings (by *ca.* 10 meV/BaCl). For the *Fm*-3*m* structure, the antiferromagnetic orderings were less energetically favorable for all pressures, while the weak ferromagnetic and non-magnetic orderings have comparable energies. Based on the energetics, the ferromagnetic orderings were the only ones considered in the HSE [22] calculations. It should be noted however that the energy differences between different magnetic orderings in BaCl are fairly small. The lowest-energy ferromagnetic magnetic ordering represents a possible solution, which does not eliminate the possibility that other magnetic orderings may also exist in BaCl. Here it is important to note [16] that the spin-polarized ground state was obtained in HSE hybrid calculations, as the GGA method is biased towards non-magnetic states. Finding a magnetic ground state in a main-group compound is very unusual. The calculated spin polarized DOS (Figs. 2-16a and 2-16b) shows this interesting feature, as well as the difference between the *Fm*-3*m* and *Pm*-3*m* structures.

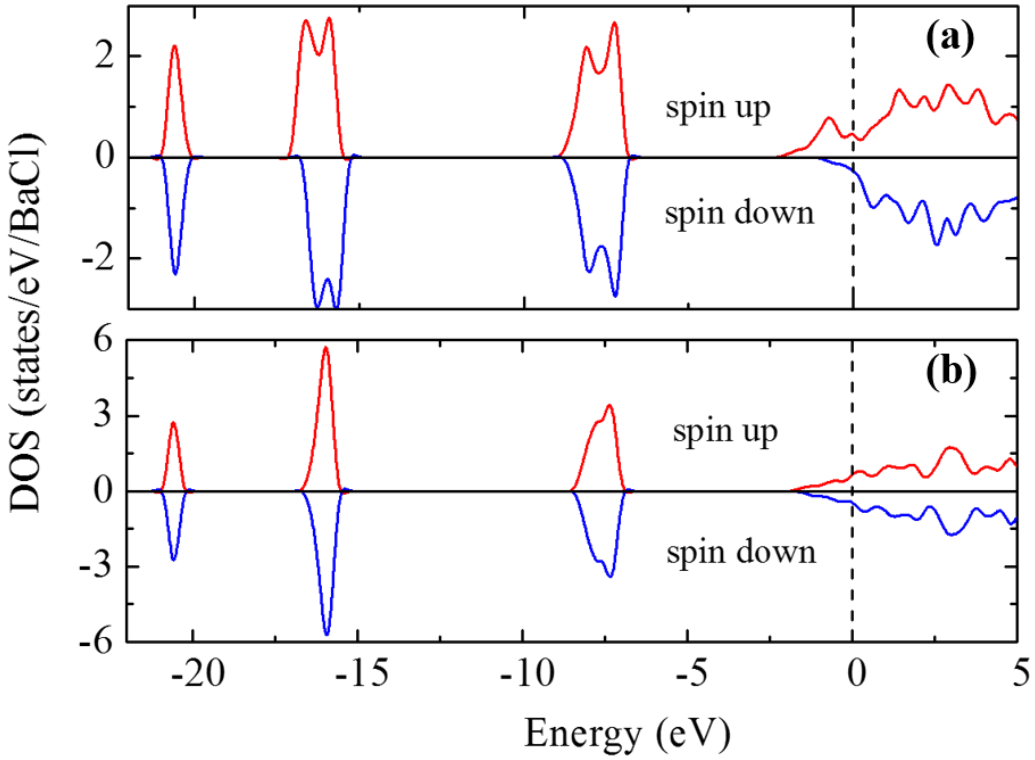

Figure 2-16. Spin polarized total DOS for (a) *Pm*-3*m* and (b) *Fm*-3*m* structures calculated at ambient pressure. Figure produced by Y. Yao.

The DOS of the *Pm*-3*m* structure (Fig. 2-16a) is consistent with the description of a half-metal [80], where the e_g states around the Fermi level are dominated by electrons with one spin component. This spin disparity yields a sizeable magnetic moment, i.e. ~0.70 μ_B/Ba. The *Pm*-3*m* ferromagnetic structure is more energetically favored than the non-magnetic structure (by ~50 meV/BaCl) at ambient pressure. The *Fm*-3*m* structure in contrast has a much smaller magnetic moment, *i.e.*, 0.13 μ_B/Ba, as the two spin components are almost equal (Fig. 2-16b). The greater energy splitting of the spin-up and spin-down bands in the *Pm*-3*m* structure can be understood [81] as $\Delta E \sim SJ(M/M0)$, where M and M_0 are the total and saturated magnetizations of the system, respectively, and J describes the exchange interaction strength between nearest neighbor spins (S). In the *Pm*-3*m* structure, the Ba-Ba distance is very short, *i.e.*, 3.5 Å at ambient

pressure, which induces strong e_g - e_g mixing (Figs. 2-15d and 2-15e) that account for a large *J*. In the *Fm*-3*m* structure the Ba-Ba distance is much longer, *i.e.*, 4.5 Å, resulting in substantially weakened t_{2g} - t_{2g} interactions (Fig. 2-15b) and a smaller *J*. Moreover, the *Pm*-3*m* structure also has greater DOS at the Fermi level, which, according the Stoner criterion [10], supports a stronger ferromagnetic state. The super-exchange interactions will also affect the ferromagnetism, however this is less significant compared to the direct exchanges.

These structures were then investigated for possible superconductivity behavior, as the Ba acquired transition metal properties with sufficient *d*-electron content allowing strong electron-phonon coupling. BaCl seems to satisfy the empirical rules of conventional superconductivity (Matthias rules [82]) by having *d*-electrons, high symmetries, and high valence electron density. In addition, half-metals were suggested to be possible superconductors [83, 84]. The superconducting behavior was therefore investigated for BaCl based on Eliashberg theory [85]. The calculated electron-phonon coupling constant, λ, for the *Fm*-3*m*, *R*-3*m* and *Pm*-3*m* structures are shown in Fig. 2-17a. The λ is notably higher in the *Fm*-3*m* structure than the other two structures, 0.82 at ambient pressure. At the same level of theory, it is higher than the λ for MgB_2 (~0.7) [86]. The strong coupling in the *Fm*-3*m* structure is primarily induced by the acoustic phonon branches, in particular by the softened mode at the *X* point. This suggests that near the point of structural instability, the electronic system of BaCl becomes perturbed by the increased atomic vibrations and is strongly coupled with them. This effect is most significant near the Fermi surface where the transition of 5*d* electrons to bound pairs occurs by virtue of exchanging phonons. This phenomenon has been observed under high pressure in alkali and alkaline earth metals [87, 88]. Using the Allen and Dynes modified McMillan equation [89], the estimated T_c in the *Fm*-3*m* structure is ~3.4 K at ambient pressure (Fig. 2-17b), which is close to the T_c of Ba

(~5 K) [90]. In this estimate, the Coulomb pseudopotential, μ^*, was taken at an empirical value of 0.1. At ambient pressure, the estimated T_c for the *R*-3*m* and *Pm*-3*m* structures are ~1.5 K, comparable to the T_c of Al (~1.2 K). At high pressures, the electronic structures become stabilized while the electron-screened Coulombic repulsions are enhanced. As a result, the T_c in all three structures decreases with increasing pressure and vanish at ~15 GPa (Fig. 2-17b).

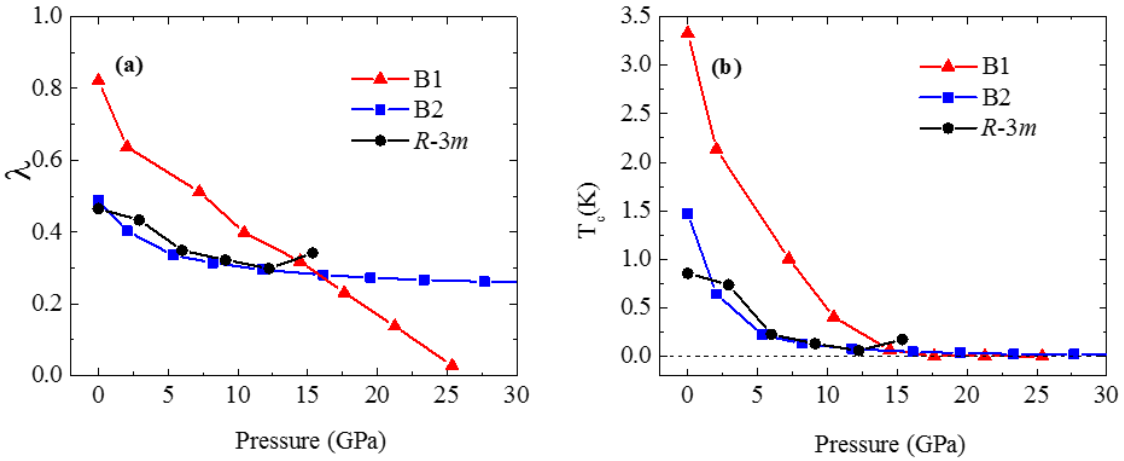

Figure 2-17. (a) Pressure dependence of electron-phonon coupling constant, λ, for structures of BaCl. (b) Pressure dependence of calculated Tc for structures of BaCl. Figure produced by Y. Yao.

2.4.4 BaCl: Conclusion

We predict novel BaCl compounds form at high pressure by reacting $BaCl_2$ with Ba. At ~9 GPa, a *Fm*-3*m* structure becomes energetically favorable, which then transforms via an intermediate *R*-3*m* structure to a *Pm*-3*m* structure at ~15 GPa. The *Pm*-3*m* structure is predicted to be thermodynamically stable above ~15 GPa, and also possibly quench recoverable to ambient pressure. The formation of BaCl is made possible by the transition of a Ba 6*s* electron to the Ba 5*d* shell. HSE calculations suggest that the *Fm*-3*m* and *Pm*-3*m* structures may be ferromagnetic,

with the *Fm*-3*m* structure showing a weak magnetic moment of ~0.13 μ_B/Ba and the *Pm*-3*m* structure displaying half-metallic properties and a more sizable magnetic moment of ~0.70 μ_B/Ba. The significant *s*–*d* transition identified for BaCl at high pressure is shown to be primarily responsible for predicted superconducting behavior. The electron-phonon calculation results for these structures predicted superconducting behavior for all three structures and raises interesting speculation regarding their superconducting behavior near ambient pressure.

As we can see, these results may offer an alternative explanation into the behavior of CuO, as well as that of BaCl. Both compounds are predicted to take on cubic structures at high pressure, following the trend of *Fm*-3*m* to *Pm*-3*m*. They both also have transition metal properties, BaCl from the Ba *s* to *d* transition and CuO due to copper being a transition metal itself. We also predict that the *Fm*-3*m* structure will have a reduced magnetic moment in comparison to the *Pm*-3*m* structure for both compounds. As such, further research into the electronic structure for CuO may be necessary for an even clearer picture of the processes driving these transitions.

2.5 Conclusion

As a potential room-temperature multiferroic material, CuO has received increasing interest in recent years. The pressure-induced changes to the multiferroic properties have been investigated for the antiferromagnetic monoclinic phase. In this article, we predicted two new phases, *Fm*-3*m* and *Pm*-3*m*, as high-pressure forms of CuO using the density functional method. The *Fm*-3*m* phase resulted from the pressure-induced suppression of the Jahn-Teller distortion in the monoclinic phase and is stabilized by a net zero magnetic moment near 70 GPa. The *Pm*-3*m*

phase takes on a ferromagnetic ordering and is obtained near 400 GPa by an indirect transformation through an intermediate *R*-3*m* phase. The superexchange interactions between the Cu sites via the oxygen are critical to the phase stability and are shown to delay the phase transitions once the magnetic ordering is imposed. It is noteworthy that the stabilization of CuO structure under high pressure is determined by multiple competing mechanisms including the Jahn-Teller effects, back donation of electrons, magnetic ordering, and others. The results presented in this article represent new possibilities in the search for potential multiferroic materials and hopefully can encourage experimental efforts in this direction. BaCl also gives us further insights into transition metal-like elements. As such, future research into both of these compounds should primarily focus on experimental confirmation of the structures and examination of the magnetic properties so that more accurate predictions and understanding can be made of their multiferroic or superconducting capabilities.

CHAPTER 3

DIHYDROGEN BONDING IN COMPRESSED AMMONIA BORANE AND ITS ROLES IN STRUCTURAL STABILITY

3.1 Introduction

Hydrogen, the most abundant element in the universe, is a promising candidate to eventually replace petroleum as the fuel of choice. In the context of hydrogen storage research, ammonia borane (NH_3BH_3) has received continuous attention for decades due to its high storage capacity and moderate dehydrogenation temperature. Molecular NH_3BH_3 is a prototypical electron donor-acceptor complex formed between NH_3 and BH_3 molecules and arranged in a staggered conformation similar to the geometry of the isoelectronic ethane (C_2H_6). In the solid state, however, NH_3BH_3 and C_2H_6 have very different physical properties. For example, the melting temperature of NH_3BH_3 is higher than that of C_2H_6 by 285 K. This suggests a strong intermolecular interaction, often referred to as 'dihydrogen bonding' [91-93], to be present in NH_3BH_3. The dihydrogen bonding originates from the $N–H^{\delta+}\cdots{}^{\delta-}H–B$ charge-transfer interaction which usually occurs when the intermolecular distance $d_{H\cdots H}$ is shorter than the sum of the van der Waals (vdW) radii. A survey of the Cambridge Structural Database (CSD) carried out by Richardson et al. [92] shows that dihydrogen bonding has a preference for a bent ∠B–H···HN angle and a nearly linear ∠N–H···HB angle, arranged such that the N–H vector points toward

the middle of the B–H vector. This geometry suggests that the electron donor of the dihydrogen bond is the B–H σ bond, rather than an individual atom. This is an extraordinary illustration of the versatility of the hydrogen bonding; in the past we have seen π electrons of a multiple bond or aromatic ring, or a transition metal center, act as electron donors [94, 95].

Clearly, dihydrogen bonding, to a great extent, determines the crystal structures of NH_3BH_3. At ambient conditions, NH_3BH_3 adopts a dynamical disordered structure (*I*4*mm*) which exhibits halos of hydrogen atom occupancy surrounding the N and B atoms [96, 97]. Below 225 K, NH_3BH_3 has an ordered phase [98] with fixed hydrogen positions ($Pmn2_1$). Upon an increase in pressure, the Raman spectra of NH_3BH_3 show a redshift in the N-H stretching mode and a blueshift in the B–H stretching mode [99-102], indicating a strengthening of the dihydrogen bond via enhanced charge transfer (δ). X-ray diffraction measurements assisted by *ab initio* calculations have established the crystal structures of two high-pressure phases. An ordered $Cmc2_1$ structure [103, 104] is found to be stable above 1.0 GPa at room temperature. Upon heating, the $Cmc2_1$ structure transforms to a proton-disordered *Pnma* structure [105]. Infrared measurement, Raman spectroscopy, X-ray and neutron diffractions, as well as molecular dynamics (MD) simulations have provided evidences that there are other stable phases of NH_3BH_3 at high pressure [106-111].

This paper reports a theoretical study on the high-pressure structures of NH_3BH_3. Two new crystalline structures, with space groups *Ama*2 and $P2_1/m$ as stable phases under high pressure, were predicted. The *Ama*2 structure is calculated to be more stable than all previously reported NH_3BH_3 structures above 5.8 GPa, while the $P2_1/m$ structure becomes more stable than the *Ama*2 structure above 25 GPa. Remarkably, all NH_3BH_3 molecules in the predicted structures adopt an unprecedented eclipsed conformation, which is stabilized under high pressure by

dihydrogen interactions. To investigate the details of the dihydrogen bonding, the local environment of the NH_3BH_3 molecules in the solid is characterized by a variety of theoretical techniques, including the quantum theory of atoms-in-molecules (QTAIM) [112], natural bond orbital (NBO) [113], Wiberg bond index (WBI) [114], and charge decomposition analysis (CDA) [115]. The results confirm the primary role of dihydrogen bonding in stabilizing the solid structures. A significant finding is the identification of a subtle $B–H^{\delta-}\cdots^{\delta-}H–B$ interaction between hydrogen atoms of the same polarity. This interaction helps to stabilize the otherwise unfavorable eclipse conformation and becomes progressively important under high pressure. The outline of this paper is as follows. First, the structure and bonding of solid NH_3BH_3 phases at ambient pressure are discussed. The purpose is to examine the role of the heteropolar $N–H^{\delta+}\cdots^{\delta-}H–B$ bonding in the solid state. Next, the effect of pressure on the conformation of the NH_3BH_3 molecules in the crystals is presented. The occurrence of the homopolar $B–H^{\delta-}\cdots^{\delta-}H–B$ bonding are characterized. Finally, the relative importance of the heteropolar and homopolar bonding in the stabilization of the crystal and molecular structures is discussed.

3.2 Methods

To identify the low-energy crystal structures of NH_3BH_3, we employed a structure search scheme to locate the energy minima through an exhaustive scan of the energy surface by numerous trials. This method has been applied successfully in the past for the determination the high-pressure phase of ammonium borohydride (NH_4BH_4) [116]. Trial crystal structures were constructed from random distributions of either staggered or eclipsed NH_3BH_3, using the molecular structures optimized in gas phase. For each molecule type, 200 different stacking

patterns were generated randomly in unit cells of arbitrary shapes that contain up to four molecules. The orientations of the molecules are also randomized in the unit cell. The geometries of all the trial structures were then fully optimized. Those with the lowest enthalpies were then annealed to 300 K and equilibrated for 10 ps, in a 2×2×2 supercell, using *ab initio* MD calculations in a canonical (NVT) ensemble. This is followed by a second structural optimization. The purpose of the annealing step is to ensure that the crystalline structure indeed reaches an energy minimum as, occasionally, new structures were found after annealing [117].

Geometry optimization, enthalpies, and phonon band structures were calculated using first principles electronic structure methods based on DFT. Electronic and MD calculations were performed with VASP [32]. The PAW potential [31, 118] treats the 2*s* and 2*p* orbitals as valence levels for N and B atoms with the PBE exchange-correlation functional [20]. The wavefunctions are expanded in a planewave basis set with an energy cutoff of 700 eV. Dense *k*-point meshes were employed to sample the BZ to ensure the energies converged to better than 1 meV/atom. Phonon band structures were calculated using the ABINIT program [119], employing the Troullier-Martins pseudopotentials [120, 121], the PBE functional, and an energy cutoff of 80 Ry. The interatomic force constant matrix was calculated using linear response method in a 4×4×4 *q*-point mesh and an 8×8×8 *k*-point mesh. The all-electron charge density was computed in a 60×60×60 grid of the unit cell using the VASP program. Topological analysis of the charge density was carried out using the InteGrity program [122] based on the QTAIM. The AIM theory is an extension of quantum mechanics to open systems in which an atom within a solid is defined through the 'zero-flux' condition of the electron density gradient $\nabla\rho(r)$. The electron density distribution $\rho(r)$ and its curvatures at the saddle point along a bond path, often referred to as the 'bond critical point (BCP)', provides information about the electron concentration in the

interatomic regions, which correlate closely to the type and properties of bonding. The AIM theory has been applied with great success for the characterization of a variety of systems, such as ionic, covalent, or hydrogen-bonded compounds [123-125]. The NBO and WBI calculations were performed using the Gaussian 09 suite program [126], employing the PBE1PBE density functional and 6-31G(d) basis sets. The Multiwfn [127] was used to perform CDA and extended charge decomposition analysis (ECDA). Structure and orbitals presented in the figures were prepared with the VESTA program [128] and the VMD program [129].

3.3 Results and Discussions

3.3.1 Solid NH_3BH_3 at Ambient Pressure

Crystalline structures of NH_3BH_3 at 1 atmosphere were constructed in two groups consist of either solely staggered or eclipsed molecules. The *Pmn*2_1 structure (Fig. 3-1a) observed experimentally at low temperatures [98] was found to have the lowest energy among all structures examined. This structure was found to be more stable than the lowest energy structure that contains only eclipsed molecules, by about 2.6 kcal/mol; coincidentally, this energy difference is almost identical to the energy difference between two molecular conformers [130]. In the *Pmn*2_1 structure, each NH_3BH_3 molecule is linked to four nearest-neighbor molecules and four second-nearest-neighbor molecules in a head-to-tail fashion through $N–H^{\delta+}\cdots^{\delta-}H–B$ bonds (Fig. 3-1b). These dihydrogen bonds are arranged in layers perpendicular to the *c*-axis; one such layer is depicted in Fig. 3-1c. Within the layer all NH_3 and BH_3 groups have identical orientations. The neighboring layers above or below would have been identical, but since the

molecules are staggered, they must have the N–H and B–H bonds pointing in the opposite directions. A QTAIM analysis has identified the locations of the bond critical points in the crystal (Figs. 3-1b and 3-1c). The shortest H···H contact (1.89 Å) was found in a pair of bonds, N2–H···H–B1 and N3–H···H–B1, which has a bent ∠B–H···HN (100º) and a nearly linear ∠N–H···HB (161º). Both features are close to the expected ideal geometry described above (see below). The second shortest H···H contact (2.07 Å) was found in another pair, N4–H···H–B1 and N5–H···H–B1, which however has a nearly linear ∠B–H···HN (158º) and a bent ∠N–H···HB (128º). The occurrence of the two types of dihydrogen geometry is due to the fact that, in the solid state, it is not possible to arrange all the dihydrogen bonds in the same, preferred manner. QTAIM calculated charge densities at the bond critical points for the two H···H contacts are 0.84 and 0.45 e^{-}/Å^3, respectively, confirming that the shorter bonds are indeed stronger. Furthermore, even though the geometries are different, both dihydrogen bonds have small but positive Laplacians, a characteristic of the closed-shell interactions [131, 132]. The *I*4*mm* structure observed at above 225 K is a hydrogen disordered phase [96, 97]. Since the hydrogen positions cannot be uniquely defined, we have not calculated the energy of this structure. It is expected that the *I*4*mm* structure should have energy comparable to that of the *Pmn*2$_1$ structure. Due to the rotating NH_3 and BH_3 groups, the dihydrogen bonding environment is not able to be unambiguously characterized in this structure.

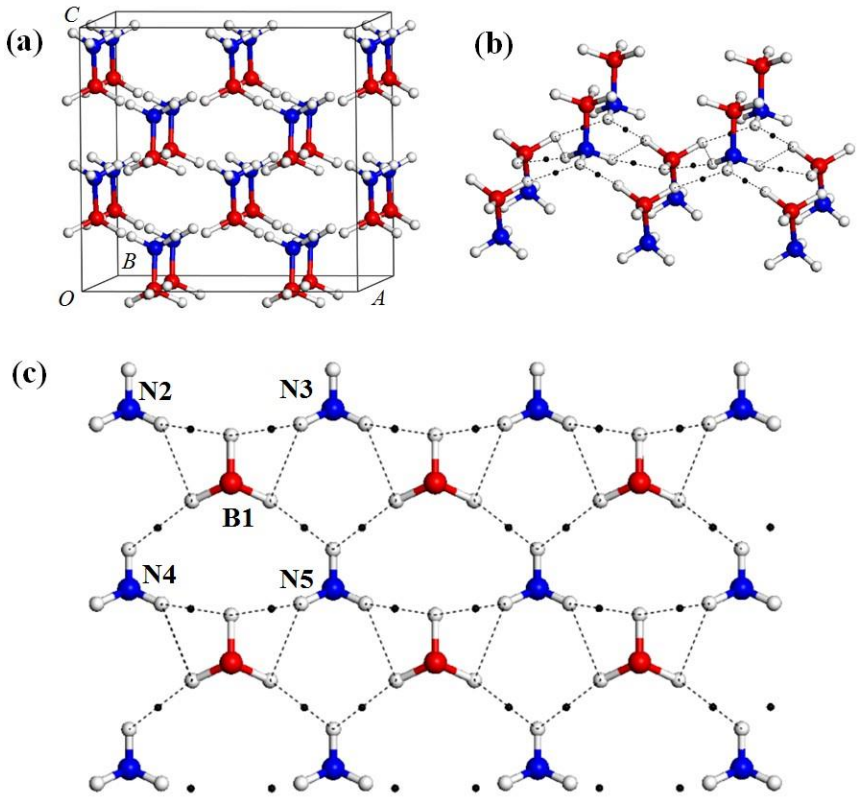

Figure 3-1. (a) The *Pmn*2$_1$ structure shown in a 2×2×2 supercell. Network of intermolecular H···H contacts (dashed lines) shown (b) in an extended structure and (c) on a plane perpendicular to the *c*-axis. Nitrogen, boron and hydrogen atoms are colored in blue, red, and white, respectively. Positions of the bond critical points are indicated by black dots [27].

3.3.2 Crystalline Structures of NH_3BH_3 at High Pressure: Earlier Studies

Spectroscopic studies have revealed at least three consecutive structural transitions of NH_3BH_3 upon compression to 20 GPa. At room temperature, two phase transitions were identified by X-ray diffraction experiments. The first phase transition near 1.5 GPa is well established, where the *I*4*mm* structure transforms to an orientational ordered *Cmc*2$_1$ structure [103, 104]. In the *Cmc*2$_1$ structure, all NH_3BH_3 molecules have a staggered conformation. The second phase transition was observed close to 12.9 GPa, and the new phase was suggested to have a *P*2$_1$ space group and may consist of both types of molecular conformers [110]. At

elevated temperatures, the *Cmc*2_1 structure undergoes a transition to a hydrogen disordered *Pnma* phase [105]. A separate X-ray diffraction study [107] shows that a structure with very low *P*1 symmetry may exist above 8 GPa. Recent MD simulations [108] also suggest two model structures, both with the *P*2_1 space group, to become stable at 15 and 25 GPa, respectively. Furthermore, a recent Raman spectroscopic measurement up to 65 GPa [102] reported a phase transition at 27 GPa, although the structure of this new phase remains elusive. Previous high-pressure studies of NH_3BH_3 and their implications to hydrogen storage applications have recently reviewed by Song [133].

3.3.3 NH_3BH_3 under Pressure: Interplay of Molecular Conformation and Dihydrogen Bonding

Crystalline structures built from either staggered or eclipsed NH_3BH_3 molecules were investigated at high pressures. In Fig. 3-2, the enthalpies of three predicted low-energy structures with the *Ama*2, *P*2_1/*m*, and *P*2_1/*c* space groups are compared with those of the experimentally known *Pmn*2_1, *Cmc*2_1, and *Pnma* structures, and that of the theoretically predicted *P*2_1 structure [108], in the pressure range of 0 – 40 GPa. The alternative *P*2_1 structure [110] was found to be mechanically and dynamically unstable and energetically non-competitive in this pressure range and will not be discussed here.

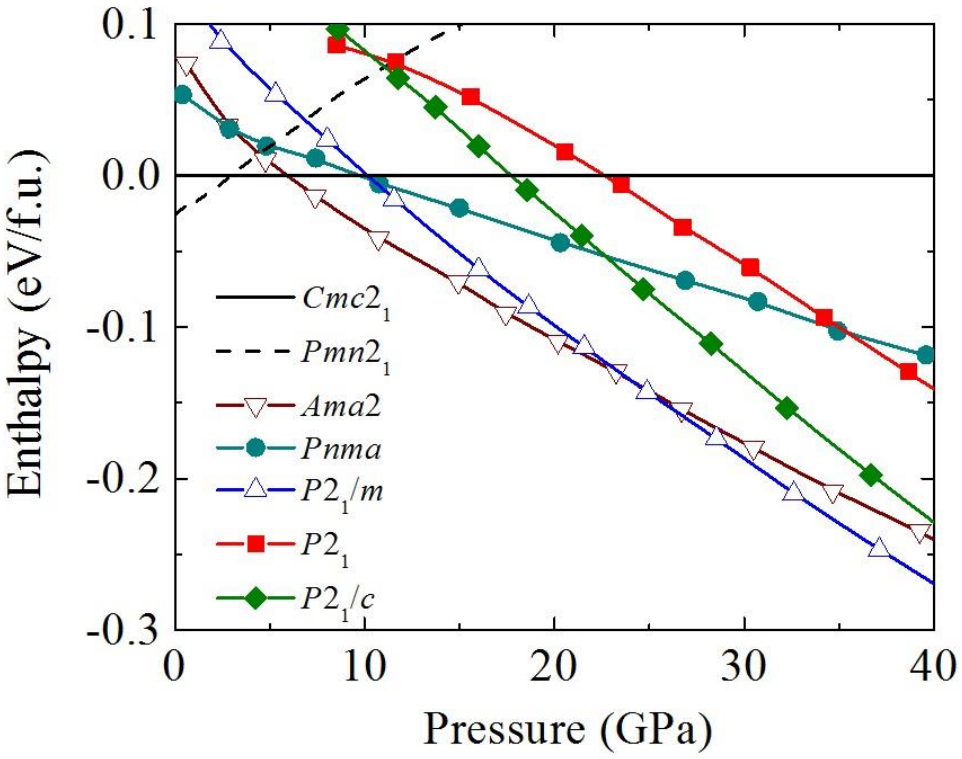

Figure 3-2. Calculated pressure dependences of enthalpies for selected NH_3BH_3 solid structures, relative to the *Cmc*2_1 structure [27].

Figure 3-2 shows that the *Cmc*2_1 structure becomes more stable than the *Pmn*2_1 structure at *ca.* 2.8 GPa, which compares well with the experimental transition pressure of 1.5 GPa (measured at T ≈ 180 K) [103]. At 9.6 GPa, the *Pnma* structure is predicted to become more stable than the *Cmc*2_1 structure. Experimentally, the *Pnma* structure has only been studied under high-temperature conditions, *i.e.*, 380 K and upward [105]. Therefore, it is not straightforward to make a direct comparison of the relative stability of the two phases from athermal calculations; an explicit consideration of entropic effect is needed. Nevertheless, X-ray diffraction measurements had revealed that the *Pnma* structure became stable and co-existed with the *Cmc*2_1 structure at high temperature near 5.5 GPa, in close agreement with the calculations. It is

important to note that both the *Cmc*2$_1$ and *Pnma* structures consist entirely of staggered molecules (Fig. 3-3).

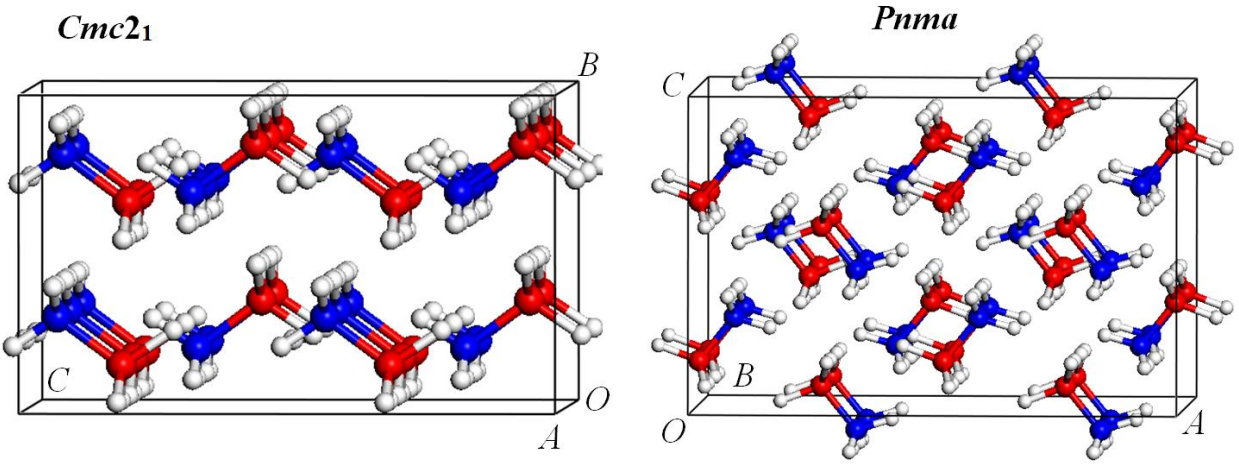

Figure 3-3. Two experimentally determined high-pressure phases of NH_3BH_3. Structures are shown in a supercell [27].

In the *Cmc*2$_1$ structure, each NH_3BH_3 molecule is connected to 10 neighbors, through 12 N–$H^{\delta+}\cdots^{\delta-}$H–B dihydrogen bonds, four of which are bifurcated. Similar to the zero-pressure high-temperature *I*4*mm* structure, the *Pnma* structure is also a hydrogen-disordered rotor phase. The positions of hydrogen atoms used in the enthalpy calculations were obtained from the optimized static geometry. Clearly, the structural motifs of the *Cmc*2$_1$ and *Pnma* structures are similar to their corresponding ambient-pressure counterparts, *Pmn*2$_1$ and *I*4*mm* structures, respectively.

Near 6 GPa, a structure consisting of only eclipsed NH_3BH_3 molecules with the *Ama*2 space group is found to be thermodynamically most stable (Fig. 3-2). This structure was predicted to transform to a *P*2$_1$/*m* phase, also made up of eclipsed molecules, at *ca*. 23.9 GPa. In this pressure range, structures containing staggered molecules are higher in enthalpy when compared to these two structures. Calculated phonon band structures (Fig. 3-4a and 3-4b) for both structures show no imaginary frequencies, indicating that both structures are mechanically and dynamically stable.

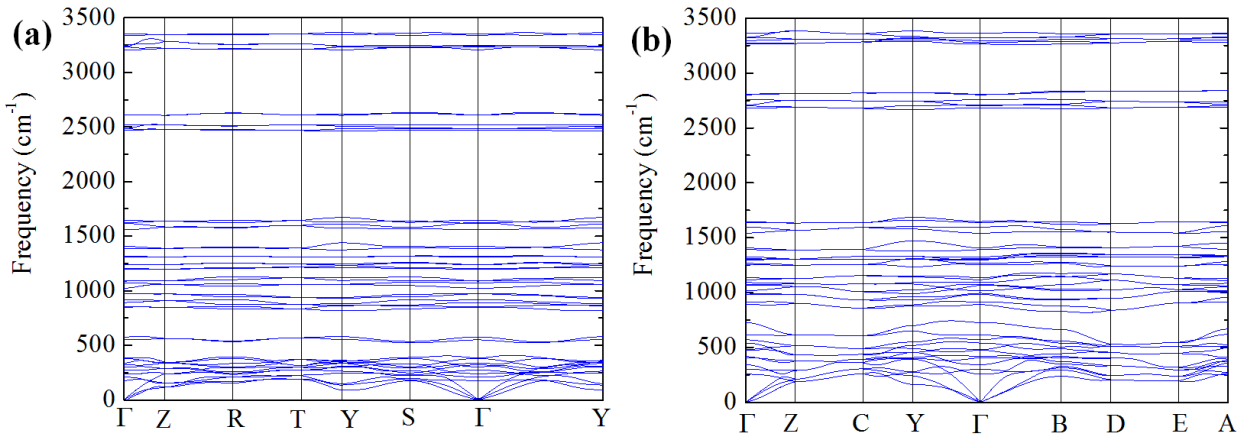

Figure 3-4. Calculated phonon dispersion relations for (a) the *Ama*2 structure at 15 GPa and (b) the $P2_1/m$ structure at 40 GPa [27].

The optimized structural parameters for the *Ama*2 and the $P2_1/m$ structures are listed in Table 3-1.

Structure	P (GPa)	Lattice parameters (Å, º)	Atomic coordinates (fractional)			
*Ama*2	10	a = 5.60, b = 8.14, c = 3.67	N 4b	0.2500	0.1353	0.3009
			B 4b	0.7500	0.1822	0.6737
			H 4b	0.2500	0.5498	0.5951
			H 8c	0.1019	0.1134	0.4609
			H 8c	0.4226	0.8869	0.8014
			H 4b	0.7500	0.1759	0.3467
$P2_1/m$	40	a = 3.97, b = 5.05, c = 3.32 β = 69.33	N 2e	0.2501	0.2500	0.3771
			B 2e	0.3748	0.7500	0.9584
			H 2e	0.0497	0.2500	0.2503
			H 2e	0.6230	0.2500	0.6903
			H 4f	0.2122	0.9381	0.9225
			H 4f	0.7850	0.9121	0.4274

Table 3-1. Structure parameters for the predicted crystalline phases of NH_3BH_3. Unique axis b is used in the space group of $P2_1/m$.

The predicted $P2_1/m$ structure is depicted in Fig. 3-5a. Similar to the *Ama*2 structure, which is stable at lower pressures, the $P2_1/m$ structure also contains only the eclipsed NH_3BH_3 molecules. In the $P2_1/m$ structure, the eclipsed molecules are held together in slabs by heteropolar dihydrogen bonds. This configuration therefore results in four equivalent $N–H^{\delta+}\cdots^{\delta-}H–B$ bonds for each NH_3BH_3 molecule, connected to four nearest neighbors, as shown in Fig3-5b. At 20 GPa, the intermolecular H···H distance within the slabs is 1.48 Å, which compares well to the value calculated in the *Ama*2 structure (1.491 Å) at the same pressure. The ∠B–H···HN and ∠N–H···HB angles are 135.35º and 160.80º, respectively. The slabs in the $P2_1/m$ structure are linked together by weaker, homopolar dihydrogen interactions (Fig. 3-5c).

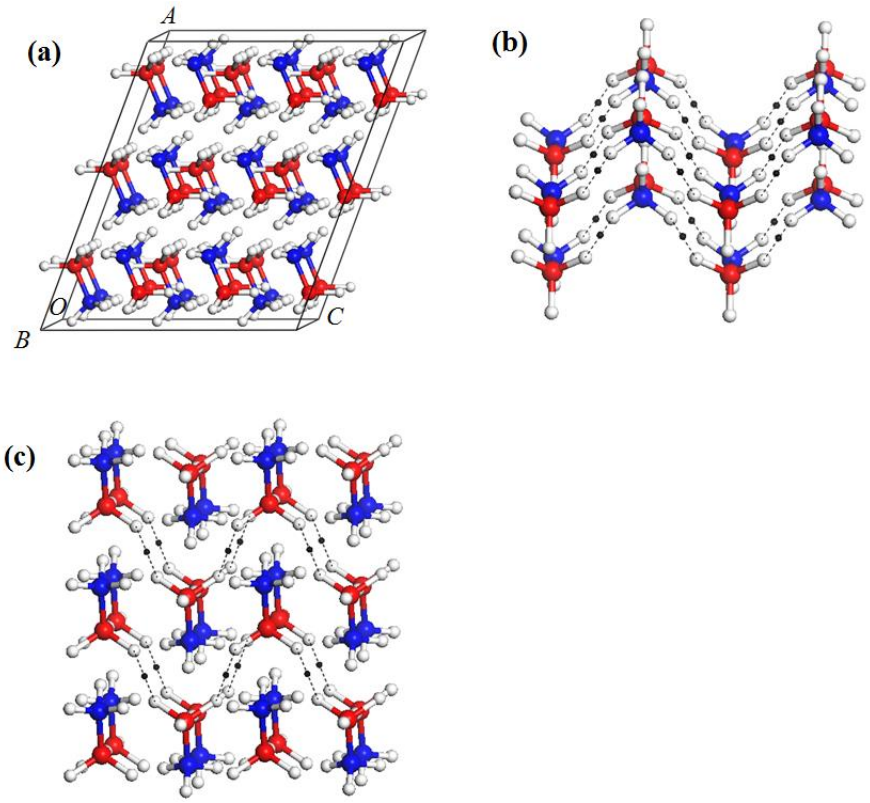

Figure 3-5. (a) The $P2_1/m$ structure shown in a 3×2×3 supercell. (b) Network of the heteropolar N–H···H–B interactions. (c) Network of the homopolar B–H···H–B interactions. Bond critical points are indicated by black dots [27].

Each NH_3BH_3 molecule is connected to another two molecules in the nearest slab by two equivalent B–$H^{\delta-}\cdots^{\delta-}$H–B interactions. Being primarily covalent, the B–$H^{\delta-}\cdots^{\delta-}$H–B bond is symmetrical with respect to the center of the H···H contact. At 20 GPa, the calculated H···H distance is 1.767 Å, whereas the ∠B–H···HB angle is 141.92º, both corresponding well with the values of the *Ama*2 structure. The $P2_1/m$ and *Ama*2 structures have very similar bonding motifs. Their enthalpies, however, are different because of the different stacking patterns of molecules. It is interesting, and significant, that theoretical calculations predict that NH_3BH_3 adopts an eclipsed conformation in solid state once sufficient pressure is applied. As a well-known fact, the staggered conformer is intrinsically lower in energy than the eclipsed one [134]. Compression will certainly have an effect on the molecular geometry; molecules in the crystals are expected to be distorted. However, it is unlikely that the energy involved in the small distortions can compensate for the reversal of the order of the molecular stability. To illustrate this point, we have extracted an eclipsed molecule from the *Ama*2 structure and a staggered molecule from the $Cmc2_1$ structure, and compared their energy difference, which turns out to be *ca.* 0.09 eV/f.u., almost the same as the energy difference between undistorted molecules [130]. Clearly, the stabilization of eclipsed molecules in high-pressure crystals must come from a different origin. We can thus show that a new type of dihydrogen interaction helps in overcoming the energetic disadvantages of the eclipsed conformation, and that the stacking of the molecules in the crystal plays a key role.

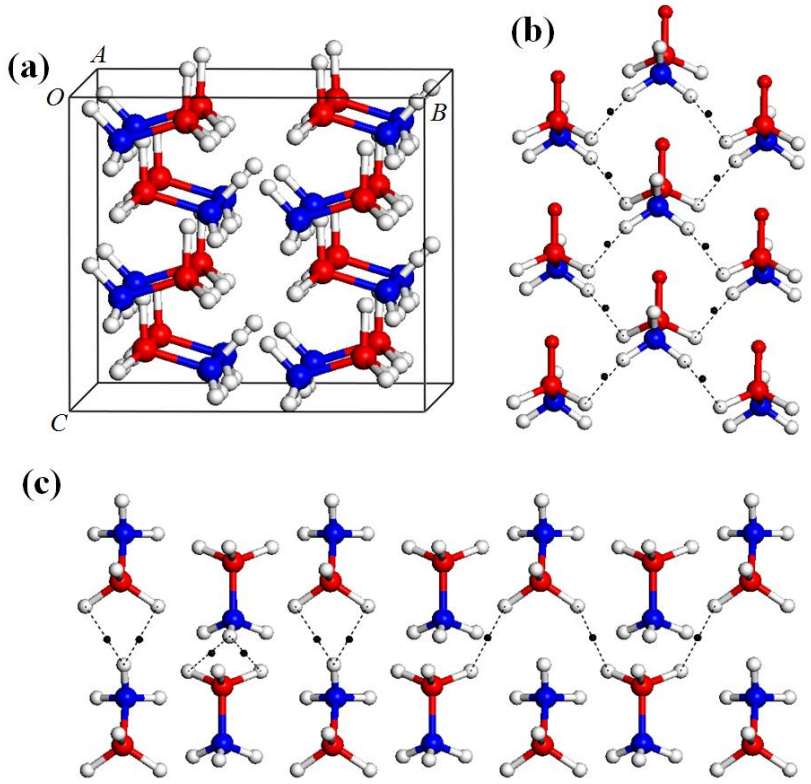

Figure 3-6. (a) The *Ama*2 structure shown in a 2×2×2 supercell. (b) Network of the shortest intermolecular H···H contacts. (c) Network of the second shortest (left half) and the third shortest (right half) intermolecular H···H contacts. Bond critical points are indicated by black dots [27].

As an explicit example, we shall study the crystal and electronic structures of the high-pressure *Ama*2 phase (Fig. 3-6a) in detail. In this structure, NH_3BH_3 molecules form slabs parallel to the *a*-*c* plane; one such slab is shown in Fig. 3-6b. Within each slab, the molecules are connected to four nearest neighbors in a head-to-tail fashion via dihydrogen bonds. As a result of these interactions, the N-B bonds are tilted toward their nearest neighbors. The dihydrogen bonds are arranged in two layers, and, since the molecules are eclipsed, these two layers have identical geometry. This configuration, therefore, allows all four equivalent $N–H^{\delta+}\cdots{}^{\delta-}H–B$ bonds connected to a molecule to have a bent ∠B–H···HN (101.45º) and a nearly linear ∠N–H···HB

(161.35º), which is the preferred geometry for the N–H$^{\delta+}$···$^{\delta-}$H–B bond (see below). In Fig. 3-7a, the all-electron density map depicted on one of these layers shows unambiguously an accumulation of electrons between the NH_3 and BH_3 groups. To accommodate the head-to-tail configuration when two NH_3BH_3 molecules are brought close to each other, electrons from the two molecular fragments are pushed into the intermolecular regions to compensate for the unfavorable inter-proton repulsions [135]. The dihydrogen bonding network originates from these accumulated electron densities. A more quantitative analysis from the examination of the bond critical points along the bond paths will be presented later (see above). The N–H$^{\delta+}$···$^{\delta-}$H–B bonds in the slabs have short H···H contacts, *i.e.*, 1.60 Å (at 10 GPa), which is significantly shorter than the vdW separation (2.40 Å). In comparison, at the same pressure the shortest H···H contacts in the *Cmc*2$_1$ structure and the *Pnma* structure are 1.73 Å and 1.85 Å, respectively.

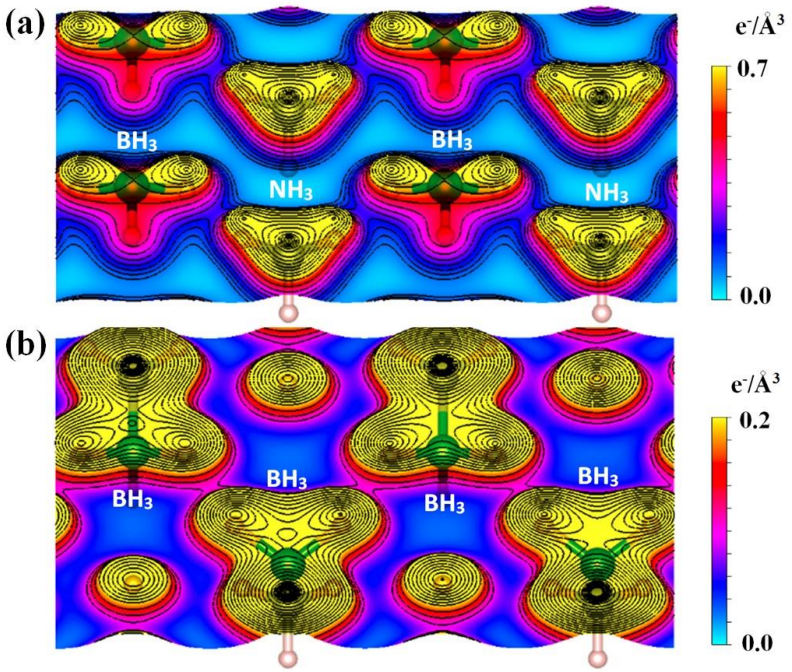

Figure 3-7. All-electron density maps for (a) the shortest N–H$^{\delta+}$···$^{\delta-}$H–B contacts within a slab and (b) the shortest B–H$^{\delta-}$···$^{\delta-}$H–B contacts across adjacent slabs, in the *Ama*2 structure optimized at 10 GPa [27].

The adjacent slabs in the *Ama*2 structure are also linked by dihydrogen interactions. The interactions can be classified into two distinct types: bifurcated N–$H^{\delta+}\cdots^{\delta-}$H–B bond and homopolar B–$H^{\delta-}\cdots^{\delta-}$H–B bond (Fig. 3-6c). The bifurcated bonding features two equivalent H···H bonds involving one hydrogen atom from NH_3 and two hydrogen atoms from BH_3. The calculated H···H distance is 1.96 Å, notably longer than those within the slabs. The ∠N–H···HB and ∠B–H···HN are 149.48º and 97.63º, respectively. A similar bifurcated geometry has been suggested [136] for the head-to-tail $(NH_3BH_3)_2$ dimer. The calculated H···H distance of 1.99 Å, ∠N–H···HB of 144.48º, and ∠B–H···HN of 88.6º, for the dimer are comparable to those in the *Ama*2 solid. Significantly, the homopolar B–$H^{\delta-}\cdots^{\delta-}$H–B interaction also appears to participate in stabilizing the eclipsed conformers in the crystal. A major structural difference between the homopolar and heteropolar bonds is that the former has a symmetric geometry, *i.e.*, the B–H bond lengths and the ∠B–H···HB angles are equal for both molecular fragments. As will be shown below, this geometrical arrangement is a result of a secondary covalent interaction, which can be explained, in part, through molecular orbital theory. This is an important feature of the B–$H^{\delta-}\cdots^{\delta-}$H–B interaction which separates it from the vdW types of interactions: the latter have no preferred directionality, and are much weaker in strength. At 10 GPa, the calculated ∠B–H···HB angle and H···H distance for the homopolar interaction are 139.39º and 2.03 Å, respectively. Clearly, this H···H distance is still much shorter than the sum of two vdW radii. The calculated all-electron density map on the plane containing B–$H^{\delta-}\cdots^{\delta-}$H–B bonds shows an accumulation of electrons, albeit with lower densities, between two homopolar hydrogen atoms (Fig. 3-7b). This is the sign of a subtle, but significant, bonding interaction. The concept of homopolar dihydrogen interaction is not new. This phenomenon has been observed previously in a wide variety of organic and organometallic molecules; a review of this is given in Ref. 137. The B–$H^{\delta-}\cdots^{\delta-}$H–B

interaction was predicted to be present in an isolated ammonia borane tetramer in gas phase [138]. Evidences of this interaction have also been found in the thermal decomposition process of NH_3BH_3 [139]. Similar interactions also present in alkali-metal amido-boranes [140] and potentially can play a key role in hydrogen storage applications. The homopolar C–H···H–C interactions have also been observed in alkanes [141, 142].

In Table 3-2, the topological properties of the electron density in the *Ama*2 structure are presented and compared with those in the $Cmc2_1$ structure. This comparison reveals a general "shorter bond = stronger bond" paradigm. The electron density $\rho(r_{BCP})$ at the bond critical point is directly determined by the H···H distance *d*; the relation is almost linear, and independent of the bond polarities. For conventional hydrogen bonds, earlier ambient pressure studies [123, 124] suggest that the $\rho(r_{BCP})$ should fall in a range of 0.04 to 0.24 $e^-/Å^3$. By this approximate measure all dihydrogen interactions in solid NH_3BH_3 may be comparable in strength to that of conventional hydrogen bonds. Notably, the intraslab $N–H^{\delta+}\cdots^{\delta-}H–B$ bonds (1.60 Å) in the *Ama*2 structure appear to be on the stronger side of this category. The Laplacian at the bond critical point, $\nabla^2\rho(r_{BCP})$, identifies the ionicity of the bond. For closed-shell interactions, the $\nabla^2\rho(r_{BCP})$ is positive and its magnitude decreases from ionic bonding to hydrogen bonding, and on to vdW interactions. It has been shown that the $\nabla^2\rho(r_{BCP})$ of conventional hydrogen bonds has a range of 0.578 to 0.843 $e^-/Å^5$ [123, 124]. By this measure, all heteropolar bonds in Table 3-2 show greater ionicity than conventional hydrogen bonds, whereas the homopolar one is a shared interaction in nature.

Structure	d Å	Bond Type	Multiplicity	$\rho(r_{BCP})$ $e^-/Å^3$	$\nabla^2\rho(r_{BCP})$ $e^-/Å^5$	E_{BD} kJ/mol
*Ama*2	1.60	N-H$^{\delta+}\cdots^{\delta-}$H-B	4	0.2186	1.4435	31.367
	1.96	N-H$^{\delta+}\cdots^{\delta-}$H-B	4	0.1099	1.1495	13.106
	2.03	B-H$^{\delta-}\cdots^{\delta-}$H-B	4	0.1039	0.8314	10.957
*Cmc*2$_1$	1.73	N-H$^{\delta+}\cdots^{\delta-}$H-B	4	0.1621	1.4809	21.798
	1.76	N-H$^{\delta+}\cdots^{\delta-}$H-B	4	0.1363	1.4053	17.672
	1.89	N-H$^{\delta+}\cdots^{\delta-}$H-B	4	0.1294	1.2193	15.891

Table 3-2. Topological properties of the bond critical points at the three shortest intermolecular H···H contacts for the *Ama*2 and *Cmc*2$_1$ structures at 10 GPa. Multiplicity is the number of dihydrogen bonds connected to a NH_3BH_3 molecule.

The dissociation energy (E_{BD}) for hydrogen bonds and their variants can be estimated from the potential energy density $V(r_{BCP})$ at the bond critical points, *i.e.*, $E_{BD} = -(1/2)V(r_{BCP})$ [143, 144]. One way to calculate $V(r_{BCP})$ is by using the virial theorem, which relates $V(r_{BCP})$ and the kinetic energy density $G(r_{BCP})$ to the local Laplacian $\nabla^2\rho(r_{BCP})$,

$$V(r_{BCP}) = \frac{\hbar^2}{4m}\nabla^2\rho(r_{BCP}) - 2G(r_{BCP}) \quad (3.1)$$

For closed-shell interactions, a simple approach has been proposed for the evaluation of the $G(r_{BCP})$ from the experimental electron density distribution [145],

$$G(rBCP) = \frac{3}{10}(3\pi^2)^{\frac{2}{3}}\rho^{\frac{5}{3}}(r_{BCP}) + \frac{1}{6}\nabla^2\rho(r_{BCP}) \quad (3.2)$$

This approximation was shown to yield a good agreement with the Hartree−Fock calculations [146] of $G(r_{BCP})$ in the medium-range region, *i.e.*, 0.5−2.1 Å to the nuclei, where the chemical bonding usually takes place. As listed in Table 3-2, the leading N−H$^{\delta+}\cdots^{\delta-}$H−B bonds (1.60 Å) in

the *Ama*2 structure has the highest E_{BD} of 31.367 kJ/mol (about 7% of the E_{BD} for a H_2 molecule), representing the strongest intermolecular interactions in this structure. These bonds are responsible for stabilizing the eclipsed molecules in the slabs. The secondary $N{-}H^{\delta+}\cdots^{\delta-}H{-}B$ bonds (1.96 Å) and the homopolar $B{-}H^{\delta-}\cdots^{\delta-}H{-}B$ bonds (2.03 Å) are inherently weaker, but still very important as they help to hold the slabs together. All three $N{-}H^{\delta+}\cdots^{\delta-}H{-}B$ bonds in the *Cmc*2_1 structure are significantly weaker than the intraslab $N{-}H^{\delta+}\cdots^{\delta-}H{-}B$ bonds in the *Ama*2 structure, which appear to be a reason why the latter is thermodynamically more stable. An additional advantage of the shorter bond length is that it yields a higher packing efficiency, or a smaller crystal volume (Fig. 3-8). From ambient pressure to 100 GPa, the volume of the *Ama*2 structure falls in the range of 96.2%–97.1%, to that of the *Cmc*2_1 structure, which makes the former energetically more favorable by virtue of a smaller *p*V work.

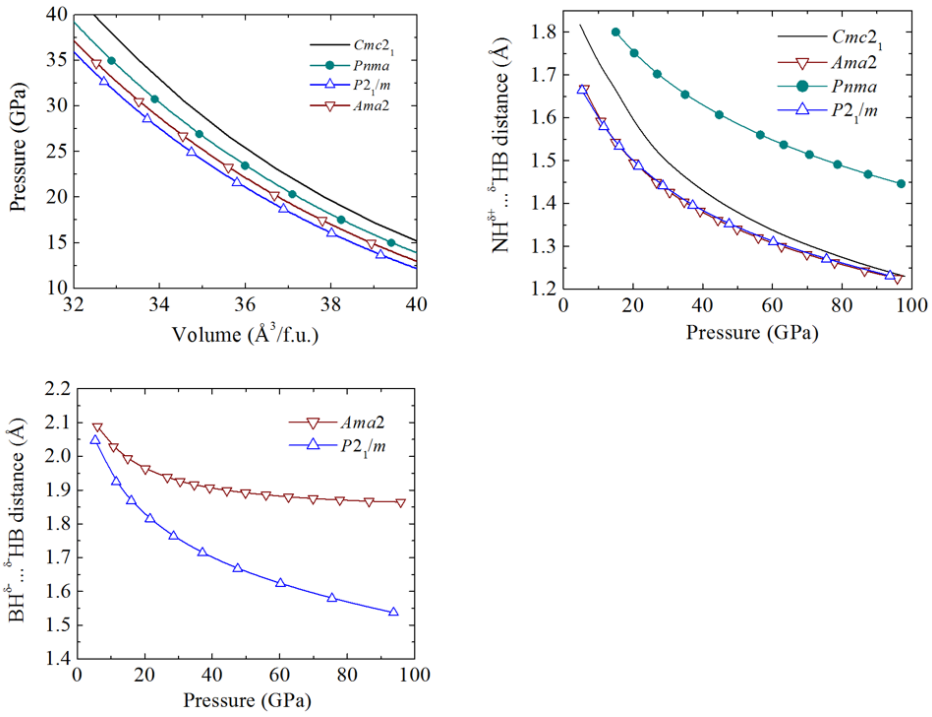

Figure 3-8. Pressure dependences of the crystal volume and dihydrogen bond distances for NH_3BH_3 structures [27].

To characterize the homopolar dihydrogen interaction, we can extract a tail-to-tail $(NH_3BH_3)_2$ dimer from the *Ama*2 structure (Fig. 3-9a).

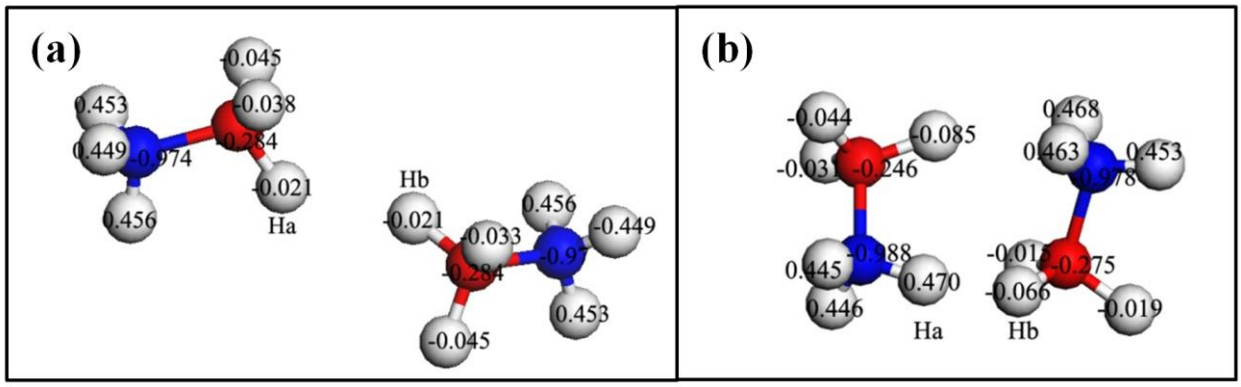

Figure 3-9. The (NH_3BH_3) dimers extracted from the *Ama*2 structure optimized at 10GPa. (a) A tail-to-tail dimer linked by a homopolar B–$H^{\delta-}\cdots^{\delta-}$H–B bond. (b) A head-to-tail dimer linked by a heteropolar N–$H^{\delta+}\cdots^{\delta-}$H–B bond. Nitrogen, boron and hydrogen atoms are colored in blue, red, and white, respectively. Numbers displayed on the atoms are the values of the NBO charges. Figure produced by X. Yong [27].

The two NH_3BH_3 molecules are linked by a B−$H^{\delta-}\cdots^{\delta-}$H−B interaction, which, in the crystal, belong to two adjacent slabs. In this geometry, the two hydrogen atoms are equivalent (indicated as H_a and H_b). The calculated NBO charges on both H_a and H_b are −0.021 e^-, indicating a weak, shared interaction presenting between them. The calculated $\rho(r_{BCP})$ and $\nabla^2\rho(r_{BCP})$ at the bond critical point between H_a and H_b are 0.114 $e^-/Å^3$ and 1.35 $e^-/Å^5$, respectively; both are comparable to the corresponding values in the solid (Table 3-2). The calculated WBI value at the bond critical point is low, *i.e.*, 0.012, which is also consistent with a weak, shared interaction [114]. This secondary B−$H^{\delta-}\cdots^{\delta-}$H−B interaction is different from the charge transfer character of the heteropolar N−$H^{\delta+}\cdots^{\delta-}$H−B interaction. For comparison, we can separate a head-to-tail $(NH_3BH_3)_2$ dimer from the same slab in the *Ama*2 structure (Figure 3-9b). For this dimer, the calculated amount of charge transfer in the N−$H^{\delta+}\cdots^{\delta-}$H−B bond is *ca.* −0.033 e^-, which is revealed in the NBO analysis as a more negatively charged H_b, compared to the other

two H atoms bonded to the same B atom, and a more electron deprived H_a, compared to the other H atoms bonded to the same N atom. The same analysis revealed no evidence of charge transfer in the homopolar interaction for the tail-to-tail dimer.

The overlap population between two molecular fragments provides information on the nature of the interaction between the two fragmental orbitals; that is, positive and negative overlaps correspond to bonding (in-phase) and antibonding (out-of-phase) interactions, respectively. The CDA calculated overlap populations between the two NH_3BH_3 molecules in the tail-to-tail dimer are 0.072, 0.040, −0.009, and −0.165 for molecular orbitals (MO) #15, #16, #17, and #18, respectively. These results clearly reveal that orbitals #15 and #17 are bonding MOs, and orbitals #16 and #18 are their antibonding counterparts; an extended CDA molecular orbital diagram is shown in Figure 3-10.

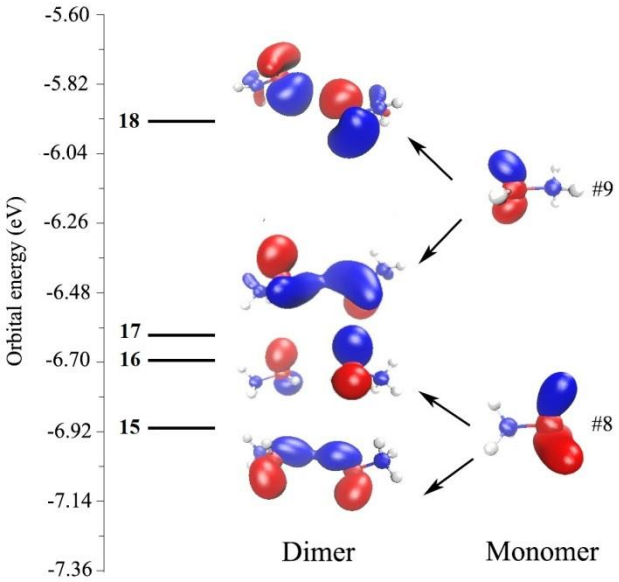

Figure 3-10. Molecular orbital diagram calculated for the homopolar B−$H^{\delta-}\cdots^{\delta-}$H−B bond in a tail-to-tail $(NH_3BH_3)_2$ dimer extracted from the *Ama*2 structure (optimized at 10 GPa). The orbitals were plotted using an isovalue of 0.04 $e^-/Å^3$. Figure produced by X. Yong [27].

The MO pair #15 and #16 is primarily derived from interactions between the fragmental orbital (#8) of the NH_3BH_3 monomers, while the pair #17 and #18 is primarily constructed by the

fragmental orbital #9. In both cases, the MOs are dominated by the H–B pπ orbital with a larger lobe on the B atoms. Therefore, the B−$H^{\delta-}\cdots^{\delta-}$H−B bond is the result of a secondary interaction of B–H bonds between the monomers. The calculated seconder order interaction energy (E^2) is 0.78 kcal/mol, which indicates a relatively weak interaction, but stronger than usually anticipated.

3.4 Conclusions

As a potential hydrogen storage material, NH_3BH_3 has received extensive scientific investigation over the past decades. The NH_3BH_3 molecules adopt a staggered conformation, which, in crystalline structures, are stabilized by the charge-transfer N−$H^{\delta+}\cdots^{\delta-}$H−B interactions. In this article, we predicted the unprecedented eclipsed conformer to exist in the solid state of NH_3BH_3 under high pressure. A novel hydrogen−hydrogen interaction facilitated by hydrogen atoms with the same polarity, namely the homopolar B−$H^{\delta-}\cdots^{\delta-}$H−B interaction, was also revealed in the solid state, which, surprisingly, may have the strength comparable to that of conventional hydrogen bonds. The B−$H^{\delta-}\cdots^{\delta-}$H−B interaction originates from the secondary interactions between two BH_3 groups, in which the electron density is shared symmetrically between the participating H atoms. This bonding mechanism is distinctly different from the ubiquitous N−$H^{\delta+}\cdots^{\delta-}$H−B interaction where electron donor and acceptor can be clearly identified. In the high-pressure crystalline structures, the B−$H^{\delta-}\cdots^{\delta-}$H−B interaction has determining influences on crystal packing, which helps to stabilize the otherwise unfavorable eclipsed molecules. The results presented in this article represent an important advance in the understanding of ammonia borane, and dihydrogen interactions in general. The dihydrogen

interactions potentially have the ability to assist in the release of molecular H_2 from solid structures, which may provide promising new routes to a rational design of hydrogen storage materials.

CHAPTER 4

CONCLUDING REMARKS

Increased forces and stress on a solid due to high pressure has been seen to have an extreme effect on the physical properties of a material. The atomic positions can shift, altering the crystal structure to novel lower energy forms. The electronic structure can change, which can affect the magnetic properties, the conductive properties, and can even alter the behavior of an alkaline earth metal to be like a transition metal. High pressure research offers insights into materials which may have new and interesting properties which are not observed at ambient conditions otherwise, such as multiferroics, superconductors, or hydrogen fuel storage materials.

While there are practical limits to the extremes that laboratory experiments can reach in terms of pressure, numerical computations are limited by the computing power and time available, and the accuracy of the approximations used in the calculations. In this thesis, we examined the structural, electronic and magnetic properties of three solid materials. In particular, we predicted that CuO changes from a monoclinic structure to, first, a rocksalt structure near 70 GPa and then to a CsCl structure near 400 GPa. This structural change is accompanied by an electron charge back-transfer from the oxygen site to the copper site in the rocksalt phase, and a change in the magnetic structure from antiferromagnetic to non-magnetic to ferromagnetic, respectively. While the pressure for the rocksalt phase at least is readily attainable, the CsCl phase may require state of the art techniques to verify experimentally, though it may exist within the earth, where pressures are much higher. These predictions may offer insight into multiferroic

behavior for transition metal oxides. We also examined BaCl, which was also predicted to have a high pressure rocksalt phase which transitions to the CsCl phase, accompanied by a reduced magnetic moment for the rocksalt phase and a ferromagnetic structure for the CsCl phase. The Ba in BaCl also adopts transition metal properties due to the pressure. This seems to lend support to the predictions made for CuO, and as the pressures predicted for the BaCl transitions are lower than the CuO transitions, they will be much easier to verify experimentally.

Alternative fuel sources are also a growing field of interest, especially in the fields of locating hydrogen fuel storage materials which allow for easy release of H_2 molecules. We predicted that NH_3BH_3 takes on two high pressure forms, both of which adopt an eclipsed conformation. This eclipsed conformation is due to the homopolar dihydrogen bonds between layers in the solid. These dihydrogen bonds in NH_3BH_3 may allow for H_2 molecules to be more easily extracted from the solid, making ammonia borane a good potential hydrogen fuel storage medium, and perhaps directing hydrogen fuel storage research towards finding other materials which may also share these homopolar dihydrogen bonds.

LIST OF REFERENCES

[1] P. A. M. Dirac. “Quantum mechanics of many-electron systems”. *Proc. Roy. Soc. A.* **1929**, *123*, 714

[2] N. W. Ashcroft and N. D. Mermin. *Solid State Physics*. Thomson Learning, Inc. **1976**

[3] A. Torabi, “Computational Studies of Compressed Diborane and Engineered Narrow-Gap Semiconductors”. *Electronic Thesis and Dissertation Repository*. Thesis, University of Western Ontario, **2015**, Paper 3163, http://ir.lib.uwo.ca/etd/3163

[4] Y. Yao. “Structures, bonding and transport properties of high pressure solids”. *University of Saskatchewan Electronic Theses and Dissertations*. Thesis, University of Saskatchewan, **2008**, http://hdl.handle.net/10388/etd-09172008-152817

[5] R. O. Jones. “Density functional theory: Its origins, rise to prominence, and future”. *Rev. Mod. Phys.* **2015**, *87*, 897

[6] P. Hohenberg and W. Kohn. “Inhomogeneous Electron Gas”. *Phys. Rev.* **1964**, *136*, B864

[7] W. Kohn and L. J. Sham. “Self-Consistent Equations Including Exchange and Correlation Effects’. *Phys. Rev.* **1965**, *140*, A1133

[8] V. N. Staroverov. “Density-functional approximations for exchange and correlation”. *A Matter of Density: Emploring the Electron Density Concept in the Chemical, Biological, and Materials Sciences*. John Wiley & Sons, Hoboken, NJ. **2013**, 125-156

[9] R. O. Jones and O. Gunnarson. “The density functional formalism, its applications and prospects”. *Rev. Mod. Phys.* **1989**, *31*, 6779

[10] E. C. Stoner. “Collective electron ferromagnetism”. *Proc. R. Soc. London Ser. A.* **1938**, *165*, 372

[11] M. Cococcioni and S. de Gironcoli. “Linear response approach to the calculation of the effective interaction parameters in the LDA+U method”. *Phys. Rev. B.* **2005**, *71,* 035105

[12] V. I. Anisimov, J. Zaanen and O. K. Andersen. “Band theory and Mott insulators: Hubbard *U* instead of Stoner *J*”. *Phys. Rev. B.* **1991**, *44,* 943

[13] A. I. Liechtenstein, V. I. Anisimov and J. Zaanen. “Density-functional theory and strong interactions: Orbital ordering in Mott-Hubbard insulators”. *Phys. Rev. B.* **1995**, *52,* R5467

[14] S. L. Dudarev, G. A. Botton, S. Y. Savrasov, C. J. Humphreys and A. P. Sutton. “Electron-energy-loss spectra and the structural stability of nickel oxide: An LSDA+U study”. *Phys. Rev. B.* **1998**, *57,* 1505

[15] J. P. Perdew, K. Burke and Y. Wang. “Generalized gradient approximation for the exchange-correlation hole of a many electron system”. *Phys. Rev. B.* **1996**, *54,* 16533

[16] J. Botana, X. Wang, C. Hou, D. Yan, H. Lin, Y. Ma and M Miao. “Mercury under Pressure acts as a Transition Metal: Calculated from First Principles”. *Angew. Chem. Int. Ed.* **2015**, *54,* 9280

[17] A. D. Becke. “Density-functional thermochemistry. III. The role of exact exchange”. *J. Chem. Phys.* **1993**, *98,* 5648

[18] M. Levy and J. P. Perdew. “Density Functionals for Exchange and Correlation Energies: Exact Conditions and Comparison of Approximations”. *Int. J. of Quantum Chem*. **1994**, *49,* 539

[19] E. H. Lieb and S. Oxford. “Improved Lower Bound on the Indirect Coulomb Energy”. *Int. J. of Quantum Chem.* **1981**, *19,* 427

[20] J. P. Perdew, K. Burke and M. Ernzerhof. “Generalized Gradient Approximation Made Simple”. *Phys. Rev. Lett.* **1996**, *77*¸ 3865

[21] J. P. Perdew, A. Ruzsinszky, G. I. Csonka, O. A. Vydrov, G. E. Scuseria, L. A. Constantin, X. Zhou and K. Burke. “Restoring the Density-Gradient Expansion for Exchange in Solids and Surfaces”. *Phys. Rev. Lett.* **2008**, *100*, 136406

[22] J. Heyd, G. E. Scuseria and M. Ernzerhof. “Hybrid functionals based on a screened Coulomb potential”. *J. Chem. Phys.* **2003**, *118*, 8207

[23] C. Kittel. *Introduction to Solid State Physics 8th ed.* John Wiley & Sons, Inc., New Jersey, **2005**

[24] M. C. Payne, M. P. Teter, D. C. Allan, T. A. Arias and J. D. Joannopoulos. “Iterative minimization techniques for *ab initio* total-energy calculations: molecular dynamics and conjugate gradients”. *Rev. Mod. Phys.* **1992**, *62*, 1045

[25] H. J. Monkhorst and J. D. Pack. “Special points for Brillouin-zone integrations”. *Phys. Rev. B.* **1976**, *13*, 5188

[26] E. Engel. “Normconserving Pseudopotentials”. **April 19, 2004**. http://th.physik.uni-frankfurt.de/~engel/ncpp.html

[27] Y. Yao, X. Yong, J. S. Tse and M. J. Greschner. “Dihydrogen Bonding in Compressed Ammonia Borane and Its Roles in Structural Stability”. *J. Phys. Chem. C.* **2014**, *118*, 29591

[28] P. D. De Cicco and F. A. Johnson. “The Quantum Theory of Lattice Dynamics. IV”. *Proc. R. Soc. London Ser. A.* **1969**, *310*, 111

[29] R. M. Pick, M. H. Cohen and R. M. Martin. “Microscopic Theory of Force Constants in the Adiabatic Approximation”. *Phys. Rev. B.* **1970**, *1*, 910

[30] M. J. Greschner, N. Chen and Y. Yao. “Pressure-driven suppression of the Jahn-Teller effects and structural changes in cupric oxide”. *J. Phys.: Cond. Matt.* **2016**, *28*, 025401

[31] G. Kresse and D. Joubert. “From ultrasoft pseudopotentials to the projector augmented-wave method”. *Phys. Rev. B.* **1999**, *59*, 1758

[32] G. Kresse and J. Hafner. “*Ab initio* molecular dynamics for liquid metals”. *Phys. Rev. B.* **1993**, *47*, 558

[33] D. Alfè. “PHON: A program to calculate phonons using the small displacement method”. *Comp. Phys. Commun.* **2009**, *180*, 2622

[34] T. Kimura, T. Goto, H. Shintani, K. Ishizaka, T. Arima and Y. Tokura. "Magnetic control of ferroelectric polarization". *Nature*. **2003**, *426*,

[35] S. W. Cheong and M. Mostovoy. "Multiferroics: a magnetic twist for ferroelectricity". *Nat. Mater*. **2007**, *6*,

[36] X. Rocquefelte, K. Schwarz, P. Blaha, S. Kumar and J. van den Brink. "Room-temperature spin-spiral multiferroicity in high-pressure cupric oxide". *Nat. Commun*. **2013**, *4*,

[37] M. A. Kastner, R. J. Birgeneau, G. Shirane and Y. Endoh. "Magnetic, transport, and optical properties of monolayer copper oxides". *Rev. Mod. Phys*. **1998**, *70*,

[38] S. Åsbrink and L. J. Norrby. "A refinement of the crystal structure of copper(II) oxide with a discussion of some exceptional e.s.d.'s". *Acta Crystallogr. Section B Struct. Crystallogr. and Crystal Chem*. **1970**, *26*,

[39] M. Derzsi, P. Piekarz and W. Grochala. "Structures of late transition metal monoxides from Jahn-Teller instabilities in the rock salt lattice". *Phys. Rev. Lett*. **2014**, *113*,

[40] L. C. Bourne, P. Y. Yu, A. Zettl and M. L. Cohen. "High-pressure electrical conductivity measurements in the copper oxides". *Phys. Rev. B.* **1989**, *40*,

[41] K. Reimann and K. Syassen. "Pressure dependence of Raman modes in CuO". *Solid State Communications*. **1990**, *76*, 136

[42] J. B. Forsyth and S. Hull. "The effect of hydrostatic pressure on the ambient temperature structure of CuO". *J. of Phys.: Cond. Matt*. **1991**, *3*,

[43] H. Ehrenberg, J. A. McAllister, W. G. Marshall and J. P. Attfield. "Compressibility of copper-oxygen bonds: a high-pressure neutron powder diffraction study of CuO". *J. of Phys.: Cond. Matt*. **1999**, *11*,

[44] Z. W. Wang, V. Pischedda, S. K. Saxena and P. Lazor. "X-ray diffraction and Raman spectroscopic study of nanocrystalline CuO under pressures". *Solid State Communications*. **2002**, *121*,

[45] T. Chatterji, P. J. Brown and J. B. Forsyth. "High pressure neutron diffraction investigation of CuO". *J. of Phys.: Cond. Matt*. **2005**, *17*,

[46] M. A. Halcrow. "Jahn-Teller distortions in transition metal compounds, and their importance in functional molecular and inorganic materials". *Chem. Soc. Rev*. **2013**, *42*,

[47] Y. Yao and D. D. Klug. "High-pressure phases of lithium borohydride LiBH4: A first-principles study". *Phys. Rev. B.* **2012**, *86*, 064107

[48] K.-T. Park, D. L. Novikov, V. A. Gubanov and A. J. Freeman. “Electronic structure of noble-metal monoxides: PdO, PtO, and AgO”. *Phys. Rev. B.* **1994**, *49*, 4425

[49] C. J. Pickard and R. J. Needs. “High-Pressure Phases of Silane”. *Phys. Rev. Lett.* **2006**, *97*, 045504

[50] Y. Joly. "X-Ray Absorption Near Edge Structure Calculation Beyond the Muffin-Tin Approximation". *Le Journal de Physique IV*. **1997**, *7*, C2-111

[51] J. E. Jaffe, J. A. Snyder, Z. Lin and A. C. Hess. "LDA and GGA calculations for high-pressure phase transitions in ZnO and MgO". *Phys. Rev. B.* **2000**, *62*, 1660

[52] H. Liu, H.-K. Mao, M. Somayazulu, Y. Ding, Y. Meng and D. Häusermann. "B1-to-B2 phase transition of transition-metal monoxide CdO under strong compression". *Phys. Rev. B*. **2004**, *70*, 094114

[53] A. Schleife, F. Fuchs, J. Furthmuller and F. Bechstedt. "First-principles study of ground- and excited-state properties of MgO, ZnO, and CdO polymorphs". *Phys. Rev. B*. **2006**, *73*, 245212

[54] H. Ozawa, F. Takahashi, K. Hirose, Y. Ohishi and N. Hirao. "Phase transition of FeO and stratification in Earth's outer core". *Science*. **2011**, *334*, 792

[55] J. B. Forsyth, P. J. Brown and B. M. Wanklyn. "Magnetism in Cupric Oxide". *J. Phys. C: Solid State*. **1988**, *21*, 2917

[56] G. Giovannetti, S. Kumar, A. Stroppa, J. van den Brink, S. Picozzi and J. Lorenzana. "High-T_c Ferroelectricity Emerging from Magnetic Degeneracy in Cupric Oxide". *Phys. Rev. Lett*. **2011**, *106*, 026401

[57] T. Oguchi, K. Terakura and A. R. Williams. "Band Theory of the Magnetic Interaction in MnO, MnS, and NiO". *Phys. Rev. B*. **1983**, *28*, 6443

[58] J. E. Pask, D. J. Singh, I. I. Mazin, C. S. Hellberg and J. Kortus. "Structural, electronic, and magnetic properties of MnO". *Phys. Rev. B*. **2001**, *64*, 024403

[59] D. Herrmann-Ronzaud, P. Burlet and J. Rossat-Mignod. "Equivalent type-II magnetic structures: CoO, a collinear antiferromagnet". *J. Phys. C: Solid State*. **1978**, *11*, 2123

[60] J. Ghijsen, L. H. Tjeng, J. van Elp, H. Eskes, J. Westerink, G. A. Sawatzky and M. T. Czyzyk. "Electronic structure of Cu_2O and CuO". *Phys. Rev. B*. **1988**, *38*, 11322

[61] J. E. Pask, D. J. Singh, I. I. Mazin, C. S. Hellberg and J. Kortus. "Structural, electronic, and magnetic properties of MnO". *Phys. Rev. B*. **2001**, *64*, 024403

[62] T. Eom, H.-K. Lim, W. A. Goddard and H. Kim. "First-Principles Study of Iron Oxide Polytypes: Comparison of GGA+U and Hybrid Functional Method". *J. Phys. Chem. C*. **2014**, *119*, 556

[63] J. B. Goodenough. "An interpretation of the magnetic properties of the perovskite-type mixed crystals $La_{1-x}Sr_xCoO_{3-\lambda}$". *Journal of Physics and Chemistry of Solids*. **1958**, *6*, 287

[64] M. Buerger. *Phase Transformations in Solids* Ed. R. Smoluchwski, J. E. Mayers and W. A. Weyl. Wiley John Wiley & Sons, Inc., New York, **1948**, p 183-211.

[65] M. Watanabe, M. Tokonami and N. Morimoto. "The transition mechanism between the CsCl-type and NaCl-type structures in CsCl". *Acta. Crystallogr*. **1977**, *A33*, 284

[66] P. Tolédano, K. Knorr, L. Ehm and W. Depmeier. "Phenomenological theory of the reconstructive phase transition between the NaCl and CsCl structure types". *Phys. Rev. B*. **2003**, *67*, 144106

[67] H. T. Stokes, D. M. Hatch, J. Dong and J. P. Lewis. "Mechanisms for the reconstructive phase transition between the B1 and B2 structure types in NaCl and PbS". *Phys. Rev. B.* **2004**, *69*, 174111

[68] A. Prescimone, C. Morien, D. Allan, J. A. Schlueter, S. W. Tozer, J. L. Manson, S. Parsons, E. K. Brechin and S. Hill. "Pressure-driven orbital reorientations and coordination-sphere reconstructions in $[CuF_2(H_2O)_2(pyz)]$". *Angew. Chem. Int. Ed. Engl*. **2012**, *51*, 7490

[69] M. Merlini, N. Perchiazzi, M. Hanfland and A. Bossak. "Phase transition at high pressure in $Cu_2CO_3(OH)_2$ related to the reduction of the Jahn-Teller effect". *Acta Crystallogr. B*. **2012**, *68*, 266

[70] Y. Yao, R. Martoňák, S. Patchkovskii and D. D. Klug. "Stability of simple cubic calcium at high pressure: A first-principles study". *Phys. Rev. B*. **2010**, *82*, 094107

[71] S. I. Zabinsky, J. J. Rehr, A. Ankudinov, R. C. Albers and M. J. Eller. "Multiple-scattering calculations of x-ray-absorption spectra". *Phys. Rev. B.* **1995**, *52*, 2995

[72] L. J. Parker, T. Atou and J. V. Badding. "Transition element-like chemistry for potassium under pressure". *Science*. **1996**, *273*, 95

[73] M. M. Abd-Elmeguid, H. Pattyn and S. Bukshpan. "Microscopic observation of the *s*→*d* transition in metallic cesium under high pressure". *Phys. Rev. Lett*. **1994**, *72*, 502

[74] A. Sanna, C. Franchini, A. Floris, G. Profeta, N. N. Lathiotakis, M. Lüders, M. A. L. Marques, E. K. U. Gross, A. Continenza and S. Massidda. "*Ab initio* prediction of pressure-induced superconductivity in potassium". *Phys. Rev. B*. **2006**, *73*, 144512.

[75] R. Nelmes, D. Allan, M. McMahon and S. Belmonte. "Self-Hosting Incommensurate Structure of Barium IV". *Phys. Rev. Lett*. **1999**, *83*, 4081

[76] I. Loa, R. J. Nelmes, L. F. Lundegaard and M. I. McMahon. "Extraordinarily complex crystal structure with mesoscopic patterning in barium at high pressure". *Nat. Mater*. **2012**, *11*, 627

[77] C. Jiang, C. R. Stanek, N. A. Marks, K. E. Sickafus and B. P. Uberuaga. "Predicting from first principles the chemical evolution of crystalline compounds due to radioactive decay: The case of the transformation of CsCl to BaCl". *Phys. Rev. B.* **2009**, *79*, 132110

[78] P. Giannozzi, S. Baroni, N. Bonini, M. Calandra, R. Car, C. Cavazzoni, D. Ceresoli, G. L. Chiarotti, M. Cococcioni, I. Dabo, A. Dal Corso, S. de Gironcoli, S. Fabris, G. Fratesi, R. Gebauer, U. Gerstmann, C. Gougoussis, A. Kokalj, M. Lazzeri, L. Martin-Samos, N. Marzari, F. Mauri, R. Mazzarello, S. Paolini, A. Pasquarello, L. Paulatto, C. Sbraccia1, S. Scandolo, G. Sclauzero, A. P. Seitsonen, A. Smogunov, P. Umari and R. M. Wentzcovitch.

"QUANTUM ESPRESSO: a modular and open-source software project for quantum simulations of materials". *J. Phys.: Condens. Matter*. **2009**, *21*, 395502

[79] M.-S. Miao and R. Hoffmann. "High-Pressure Electrides: The Chemical Nature of Interstitial Quasiatoms". *J. Am. Chem. Soc*. **2015**, *137*, 3631

[80] R. A. de Groot, F. M. Mueller, P. G. van Engen and K. H. J. Buschow. "New Class of Materials: Half-Metallic Ferromagnets". *Phys. Rev. Lett*. **1983**, *50*, 2024

[81] C. Haas. "Spin-Disorder Scattering and Magnetoresistance of Magnetic Semiconductors". *Phys. Rev*. **1968**, *168*, 531

[82] W. L. McMillan. "Transition Temperature of Strong-Coupled Superconductors". *Phys. Rev*. **1968**, *167*, 331

[83] W. E. Pickett. "Single Spin Superconductivity". *Phys. Rev. Lett*. **1996**, *77*, 3185

[84] R. E. Rudd and W. E. Pickett. "Single-spin superconductivity: Formulation and Ginzburg-Landau theory". *Phys. Rev. B*. **1998**, *57*, 557

[85] G. M. Eliashberg. "Interactions between Electrons and Lattice Vibrations in a Superconductor". *Zh. Eksp. Teor. Fiz*. **1960**, *38*, 966

[86] P. P. Singh. "From E_{2g} to Other Modes: Effects of Pressure on Electron-Phonon Interaction in MgB_2". *Phys. Rev. Lett*. **2006**, *97*, 247002

[87] D. Kasinathan, J. Kuneš, A. Lazicki, H. Rosner, C. S. Yoo, R. T. Scalettar and W. E. Pickett. "Superconductivity and Lattice Instability in Compressed Lithium from Fermi Surface Hot Spots". *Phys. Rev. Lett*. **2006**, *96*, 047004

[88] Y. Yao, J. S. Tse, K. Tanaka, F. Marsiglio and Y. Ma. "Superconductivity in lithium under high pressure investigated with density functional and Eliashberg theory". *Phys. Rev. B*. **2009**, *79*, 054524

[89] P. B. Allen and R. C. Dynes. “Superconductivity at very strong coupling”. *J. Phys. C: Solid State Phys*. **1975**, *8*, L158

[90] K. J. Dunn and F. P. Bundy. “Pressure-induced superconductivity in strontium and barium”. *Phys. Rev. B*. **1982**, *25*, 194

[91] M.P. Brown and R. W. Heseltine. “Co-ordinated BH_3 as a Proton Acceptor Group in Hydrogen Bonding”. *Chem. Commun*. **1968**, 23, 1551

[92] T. B. Richardson, S. de Gala, R. H. Crabtree and P. E. M. Seigbhan. “Unconventional Hydrogen Bonds: Intermolecular B–H···H–N Interactions”. *J. Am. Chem. Soc*. **1995**, *117*, 12875.

[93] R. Custelcean and J. E. Jackson. “Dihydrogen Bonding: Structures, Energetics, and Dynamics”. *Chem. Rev*. **2001**, *101*, 1963

[94] M. J. Calhorda. “Weak Hydrogen Bonds: Theoretical Studies”. *Chem. Commun*. **2000**, *10*, 801

[95] E. S. Shubina, N. V. Belkova and L. M. Epstein. “Novel Types of Hydrogen Bonding with Transition Metal π-Complexes and Hydrides”. *J. Organomet. Chem.* **1997**, *536−537*, 17

[96] M. E. Bowden, G. J. Gainsford and W. T. Robinson. “Room-Temperature Structure of Ammonia Borane”. *Aust. J. Chem*. **2007**, *60*, 149

[97] D. G.Allis, M. E. Kosmowski and B. S. Hudson. “The Inelastic Neutron Scattering Spectrum of $H_3B{:}NH_3$ and the Reproduction of Its Solid-State Features by Periodic DFT”. *J. Am. Chem. Soc*. **2004**, *126*, 7756

[98] W. T. Klooster, T. F. Koetzle, P. E. M. Siegbahn, T. B. Richardson and R. H. Crabtree. “Study of the N–H···H–B Dihydrogen Bond Including the Crystal Structure of BH_3NH_3 by Neutron Diffraction”. *J. Am. Chem. Soc*. **1999**, *121*, 6337

[99] S. Trudel and D. F. R. Gilson. “High-Pressure Raman Spectroscopic Study of the Ammonia−Borane Complex. Evidence for the Dihydrogen Bond”. *Inorg. Chem*. **2003**, *42,* 2814

[100] R. Custelcean and Z.A. Dreger. “Dihydrogen Bonding under High Pressure: A Raman Study of BH_3NH_3 Molecular Crystal”. *J. Phys. Chem. B*. **2003**, *107*, 9231

[101] Y. Lin, W. L. Mao, V. Drozd, J. Chen and L. L. Daemen. “Raman Spectroscopy Study of Ammonia Borane at High Pressure”. *J. Chem. Phys.* **2008**, *129,* 234509

[102] I. Kupenko, L. Dubrovinsky, V. Dmitriev and N. Dubrovinskaia. “In Situ Raman Spectroscopic Study of the Pressure Induced Structural Changes in Ammonia Borane”. *J. Chem. Phys*. **2012**, *137,* 074506

[103] Y. Filinchuk, A. H. Nevidomskyy, D. Chernyshov and V. Dmitriev. “High-Pressure Phase and Transition Phenomena in Ammonia Borane NH_3BH_3 from X-ray Diffraction, Landau Theory, and *Ab Initio* Calculations”. *Phys. Rev. B*. **2009**, *79*, 214111

[104] J. Chen, H. Couvy, H. Liu, V. Drozd, L. L. Daemen, Y. Zhao and C.-C. Kao. “In Situ X-ray Study of Ammonia Borane at High Pressures”. *Int. J. Hydrogen Energy*. **2010**, *35,* 11064

[105] J. Nylén, L. Eriksson, D. Benson and U. Häussermann. “Characterization of a High Pressure, High Temperature Modification of Ammonia Borane (BH_3NH_3)”. *J. Chem. Phys*. **2013**, *139*, 054507

[106] S. Xie, Y. Song and Z. Liu. “In Situ High-Pressure Study of Ammonia Borane by Raman and Infrared Spectroscopy”. *Can. J. Chem*. **2009**, *87*, 1235

[107] R. S. Kumar, X. Z. Ke, J. Z. Zhang, Z. J. Lin, S. C. Vogel, M. Hartl, S. Sinogeikin, L. Daemen, A. L. Cornelius, C. F. Chen and Y. S. Zhao. “Pressure Induced Structural

Changes in the Potential Hydrogen Storage Compound Ammonia Borane: A Combined X-ray, Neutron and Theoretical Investigation". *Chem. Phys. Lett*. **2010**, *495*, 203

[108] L. Wang, K. Bao, X. Meng, X. Wang, T. Jiang, T. Cui, B. Liu and G. Zou. "Structural and Dynamical Properties of Solid Ammonia Borane under High Pressure". *J. Chem. Phys*. **2011**, *134*, 024517

[109] A. Liu and Y. Song. "In Situ High-Pressure and Low-Temperature Study of Ammonia Borane by Raman Spectroscopy". *J. Phys. Chem. C*. **2012**, *116*, 2123

[110] Y. Lin, H. W. Ma, C. W. Matthews, B. Kolb, S. Sinogeikin, T. Thonhauser and W. L. Mao. "Experimental and Theoretical Studies on a High Pressure Monoclinic Phase of Ammonia Borane". *J. Phys. Chem. C*. **2012**, *116*, 2172

[111] S. Najiba, J. Chen, V. Drozd, A. Durygin and Y. Sun. "Ammonia Borane at Low Temperature Down to 90 K and High Pressure up to 15 GPa". *Int. J. Hydrogen Energy*. **2013**, *38*, 4628

[112] R. F. W. Bader. *Atoms in Molecules: A Quantum Theory*. Oxford University Press, Oxford, **1990**

[113] F. Weinhold. *Discovering Chemistry with Natural Bond Orbitals*. John Wiley & Sons, New York, **2012**

[114] K. Wiberg. "Application of the Pople-Santry-Segal CNDO Method to the Cyclopropylcarbinyl and Cyclobutyl Cation and to Bicyclobutane". *Tetrahedron*. **1968**, *24*, 1083

[115] G. Frenking and N. Fröhlich. "The Nature of the Bonding in Transition-Metal Compounds". *Chem. Rev*. **2000**, *100*, 717

[116] R. Flacau, Y. Yao, D. D. Klug, D. Desgreniers and C. I. Ratcliffe. “Structural Phase Transitions Induced by Pressure in Ammonium Borohydride”. *Phys. Chem. Chem. Phys*. **2012**, *14*, 7005

[117] Y. Yao and R. Hoffmann. BH_3 under Pressure: Leaving the Molecular Diborane Motif”. *J. Am. Chem. Soc*. **2011**, *133*, 21002

[118] P. E. Blöchl. “Projector Augmented-Wave Method”. *Phys. Rev. B*. **1994**, *50*, 17953

[119] X. Gonze, J.-M. Beuken, R. Caracas, F. Detraux, M. Fuchs, G.-M. Rignanese, L. Sindic, M. Verstraete, G. Zerah, F. Jollet, M. Torrent, A. Roy, M. Mikami, Ph. Ghosez, J.-Y. Raty and D. C. Allan. “First-Principles Computation of Material Properties: the ABINIT Software Project”. *Comput. Mater. Sci*. **2002**, *25*, 478

[120] N. Troullier and J. Martins. “Efficient Pseudopotentials for Plane-Wave Calculations”. *Phys. Rev. B*. **1991**, *43*, 1993

[121] M. Krack. “Pseudopotentials for H to Kr Optimized for Gradient-Corrected Exchange-Correlation Functionals”. *Theor. Chem. Acc*. **2005**, *114*, 145

[122] C. Katan, P. Rabiller, C. Lecomte, M. Guezo, V. Oison and M. Souhassou. “Numerical Computation of Critical Properties and Atomic Basins from Three-Dimensional Grid Electron Densities”. *J. Appl. Crystallogr*. **2003**, *36*, 65

[123] U. Koch and P. L. A. Popelier. “Characterization of C–H–O Hydrogen Bonds on the Basis of the Charge Density”. *J. Phys. Chem*. **1995**, *99*, 9747

[124] P. L. A. Popelier. “Characterization of a Dihydrogen Bond on the Basis of the Electron Density”. *J. Phys. Chem. A*. **1998**, *102*, 1873

[125] J. S. Tse, Y. Yao, D. D. Klug and S. Desgreniers. “Bonding in the ε-Phase of High Pressure Oxygen”. *J. Phys.: Conf. Ser*. **2008**, *121*, 012006

[126] M. J. Frisch, G. W. Trucks, H. B. Schlegel, G. E. Scuseria, M. A. Robb, J. R. Cheeseman, G. Scalmani, V. Barone, B. Mennucci, G. A. Petersson, H. Nakatsuji, M. Caricato, X. Li, H. P. Hratchian, A. F. Izmaylov, J. Bloino, G. Zheng, J. L. Sonnenberg, M. Hada, M. Ehara, K. Toyota, R. Fukuda, J. Hasegawa, M. Ishida, T. Nakajima, Y. Honda, O. Kitao, H. Nakai, T. Vreven, J. A. Montgomery, Jr., J. E. Peralta, F. Ogliaro, M. Bearpark, J. J. Heyd, E. Brothers, K. N. Kudin, V. N. Staroverov, R. Kobayashi, J. Normand, K. Raghavachari, A. Rendell, J. C. Burant, S. S. Iyengar, J. Tomasi, M. Cossi, N. Rega, J. M. Millam, M. Klene, J. E. Knox, J. B. Cross, V. Bakken, C. Adamo, J. Jaramillo, R. Gomperts, R. E. Stratmann, O. Yazyev, A. J. Austin, R. Cammi, C. Pomelli, J. W. Ochterski, R. L. Martin, K. Morokuma, V. G. Zakrzewski, G. A. Voth, P. Salvador, J. J. Dannenberg, S. Dapprich, A. D. Daniels, Ö. Farkas, J. B. Foresman, J. V. Ortiz, J. Cioslowski, and D. J. Fox. *Gaussian 09*. Gaussian, Inc., Wallingford, CT, **2009**

[127] T. Lu and F. Chen. "Multiwfn: A Multifunctional Wavefunction Analyzer". *J. Comput. Chem*. **2012**, *33*, 580

[128] K. Momma and F. Izumi. "VESTA 3 for Three-Dimensional Visualization of Crystal, Volumetric and Morphology Data". *J. Appl. Crystallogr*. **2011**, *44*, 1272

[129] W. Humphrey, A. Dalke and K. Schulten. "VMD: Visual Molecular Dynamics". *J. Mol. Graphics*. **1996**, *14*, 33

[130] Y. Mo, L. Song, W. Wu and Q. Zhang. "Charge Transfer in the Electron Donor−Acceptor Complex BH_3NH_3". *J. Am. Chem. Soc*. **2004**, *126*, 3974

[131] R. F. W. Bader P. J. MacDougall and C. D. H. Lau. "Bonded and Nonbonded Charge Concentrations and Their Relation to Molecular Geometry and Reactivity". *J. Am. Chem. Soc*. **1984**, *106*, 1594

[132] D. Cremer and E. Kraka. “Chemical Bonds without Bonding Electron Density: Does the Difference Electron-Density Analysis Suffice for a Description of the Chemical Bond?” *Angew. Chem., Int. Ed*. **1984**, *23*, 627

[133] Y. Song. “New Perspectives on Potential Hydrogen Storage Materials using High Pressure”. *Phys. Chem. Chem. Phys*. **2013**, *15*, 14524

[134] J. Clayden, N. Greeves and S. Warren. *Organic Chemistry*. Oxford University Press, Oxford, **2012**

[135] W. Grochala R. Hoffmann, J. Feng and N. W. Ashcroft. “The Chemical Imagination at Work in Very Tight Places”. *Angew. Chem., Int. Ed*. **2007**, *46*, 3620

[136] C. J. Cramer and W. L. Gladfelter. “*Ab Initio* Characterization of $[H_3N{\cdot}BH_3]_2$, $[H_3N{\cdot}AlH_3]_2$, and $[H_3N{\cdot}GaH_3]_2$”. *Inorg. Chem*. **1997**, *36*, 5358

[137] C. F. Matta. *In: Hydrogen Bonding-New Insights*. S. J. Grabowski, Ed. Springer, New York, **2006**

[138] D. Guerra, J. David and A. Restrepo. “$(H_3N–BH_3)_4$: The Ammonia Borane Tetramer”. *Phys. Chem. Chem. Phys*. **2012**, *14*, 14892

[139] D. J. Wolstenholme, K. T. Traboulsee, Y. Hua, L. A. Calhoun and G. S. McGrady. “Thermal Desorption of Hydrogen from Ammonia Borane: Unexpected Role of Homopolar N–H···H–B Interactions”. *Chem. Commun*. **2012**, *48*, 2597

[140] D. J. Wolstenholme, J. T. Titah, F. N. Che, K. T. Traboulsee, J. Flogeras and G. S. McGrady. “Homopolar Dihydrogen Bonding in Alkali-Metal Amidoboranes and Its Implications for Hydrogen Storage”. *J. Am. Chem. Soc*. **2011**, *133*, 16598

[141] J. J. Novoa and M.-H. Whangbo. “Interactions Energies Associated with Short Intermolecular Contacts of C–H Bonds. II. *Ab Initio* Computational Study of the C–H···H–C Interactions in Methane Dimer”. *J. Chem. Phys*. **1991**, *94*, 4835

[142] J. Echeverría, G. Aullon, D. Danovich, S. Shaik and Alvarez. “Dihydrogen Contacts in Alkanes Are Subtle But Not Faint”. *Nat. Chem*. **2011**, *3*, 323

[143] M. Souhassou, C. Lecomte, N.-E. Ghermani, M. M. Rohmer, R. Wiest, M. Benard and R. H. Blessing. “Electron Distributions in Peptides and Related Molecules. 2. An Experimental and Theoretical Study of (Z)-N-Acetyl-α, β-dehydrophenylalanine Methylamide”. *J. Am. Chem. Soc*. **1992**, *114*, 2371

[144] E. Espinosa, E. Molins and C. Lecomte. “Hydrogen Bond Strengths Revealed by Topological Analyses of Experimentally Observed Electron Densities”. *Chem. Phys. Lett*. **1998**, *285*, 170

[145] Y. A. Abramov. “On the Possibility of Kinetic Energy Density Evaluation from the Experimental Electron-Density Distribution”. *Acta Crystallogr*. **1997**, *A53*, 264

[146] R. F. W. Bader and H. Essén. “The Characterization of Atomic Interactions”. *J. Chem. Phys*. **1984**, *80*, 1943

APPENDIX

PERMISSIONS

Figure 1-1 is reprinted with permission from M. Cococcioni and S. de Gironcoli, Phys. Rev. B, 71, 035105, 2005. Copyright 2005 by the American Physical Society (see below).

AMERICAN PHYSICAL SOCIETY LICENSE TERMS AND CONDITIONS

Jan 14, 2016

This Agreement between Michael J Greschner ("You") and American Physical Society ("American Physical Society") consists of your license details and the terms and conditions provided by American Physical Society and Copyright Clearance Center.

License Number	3787780769249
License date	Jan 14, 2016
Licensed Content Publisher	American Physical Society
Licensed Content Publication	Physical Review B
Licensed Content Title	Linear response approach to the calculation of the effective interaction parameters in the $\mathrm{LDA}+\mathrm{U}$ method
Licensed Content Author	Matteo Cococcioni and Stefano de Gironcoli
Licensed Content Date	Jan 18, 2005
Licensed Content Volume Number	71
Type of Use	Thesis/Dissertation
Requestor type	Student
Format	Print, Electronic
Portion	chart/graph/table/figure
Number of charts/graphs/tables/figures	1
Portion description	Figure 1
Rights for	Main product
Duration of use	Life of Current Edition
Creation of copies for the disabled	no
With minor editing privileges	no
For distribution to	Worldwide
In the following language(s)	Original language of publication
With incidental promotional use	no
The lifetime unit quantity of new product	0 to 499
The requesting person/organization is:	Michael J Greschner
Order reference number	None
Title of your thesis / dissertation	PREDICTION OF STRUCTURES AND PROPERTIES OF HIGH-PRESSURE SOLID MATERIALS USING FIRST PRINCIPLES METHODS

Expected completion date	Feb 2016
Expected size (number of pages)	122
Requestor Location	Michael J Greschner 830 Lamarsh Lane Saskatoon, SK S7W1B7 Canada Attn: Michael J Greschner
Billing Type	Invoice
Billing Address	Michael J Greschner 830 Lamarsh Lane Saskatoon, SK S7W1B7 Canada Attn: Michael J Greschner
Total	0.00 CAD

Terms and Conditions

Terms and Conditions

The American Physical Society (APS) is pleased to grant the Requestor of this license a non-exclusive, non-transferable permission, limited to [**print** and/or **electronic** format, depending on what they chose], provided all criteria outlined below are followed.

1. For electronic format permissions, Requestor agrees to provide a hyperlink from the reprinted APS material using the source material's DOI on the web page where the work appears. The hyperlink should use the standard DOI resolution URL, http://dx.doi.org/{DOI}. The hyperlink may be embedded in the copyright credit line.
2. For print format permissions, Requestor agrees to print the required copyright credit line on the first page where the material appears: "Reprinted (abstract/excerpt/figure) with permission from [(FULL REFERENCE CITATION) as follows: Author's Names, APS Journal Title, Volume Number, Page Number and Year of Publication.] Copyright (YEAR) by the American Physical Society."
3. Permission granted in this license is for a one-time use and does not include permission for any future editions, updates, databases, formats or other matters. Permission must be sought for any additional use.
4. Use of the material does not and must not imply any endorsement by APS.
5. Under no circumstance does APS purport or intend to grant permission to reuse materials to which it does not hold copyright. It is the requestors sole responsibility to ensure the licensed material is original to APS and does not contain the copyright of another entity, and that the copyright notice of the figure, photograph, cover or table does not indicate that it was reprinted by APS, with permission from another source.
6. The permission granted herein is personal to the Requestor for the use specified and is not transferable or assignable without express written permission of APS. This license may not be amended except in writing by APS.
7. You may not alter, edit or modify the material in any manner.
8. You may translate the materials only when translation rights have been granted.
9. You may not use the material for promotional, sales, advertising or marketing purposes.
10. The foregoing license shall not take effect unless and until APS or its agent, Copyright

Clearance Center (CCC), receives payment in full in accordance with CCC Billing and Payment Terms and Conditions, which are incorporated herein by reference.

11. Should the terms of this license be violated at any time, APS or CCC may revoke the license with no refund to you and seek relief to the fullest extent of the laws of the USA. Official written notice will be made using the contact information provided with the permission request. Failure to receive such notice will not nullify revocation of the permission.

12. APS reserves all rights not specifically granted herein.

13. This document, including the CCC Billing and Payment Terms and Conditions, shall be the entire agreement between the parties relating to the subject matter hereof.

Other Terms and Conditions

Questions? customercare@copyright.com or +1-855-239-3415 (toll free in the US) or +1-978-646-2777.

Chapter 2 is adapted with permission, as outlined in the "Author's Rights after Publication by IOP" ("[…]upon transfer of copyright, IOP and/or the copyright owner grants back to authors a number of rights. These include the right to copy the article for teaching purposes, and to include the article in research theses or dissertations. Please include citation details and for online use, a link to the Version of Record. IOP's permission will be required for commercial use of an article published as part of your thesis."
http://authors.iop.org/atom/help.nsf/LookupJournalSpecific/WebPermissionsFAQ~**), from M. J. Greschner, N. Chen and Y. Yao. "Pressure-driven suppression of the Jahn-Teller effects and structural changes in cupric oxide". *J. Phys.: Cond. Matt*. 2016, 28, 025401. Copyright 2016 IOP Publishing LTD. BaCl discussion adapted from M. J. Greschner, D. D. Klug and Y. Yao. "Prediction of a Novel Stable Half-Metal Ferromagnetic BaCl Solid". (accepted to Phys. Rev. B. February 22, 2016)

Chapter 3 is adapted with permission from Y. Yao, X. Yong, J. S. Tse and M. J. Greschner. "Dihydrogen bonding in Compressed Ammonia Borane and Its Roles in Structural Stability". J. Phys. Chem. C. 2014, 118, 29591. Copyright 2014 American Chemical Society (See below).

Title: Dihydrogen Bonding in Compressed Ammonia Borane and Its Roles in Structural Stability

Author: Yansun Yao, Xue Yong, John S. Tse, et al

Publication: The Journal of Physical Chemistry C

Publisher: American Chemical Society

Date: Dec 1, 2014

PERMISSION/LICENSE IS GRANTED FOR YOUR ORDER AT NO CHARGE

This type of permission/license, instead of the standard Terms & Conditions, is sent to you because no fee is being charged for your order. Please note the following:

- Permission is granted for your request in both print and electronic formats, and translations.
- If figures and/or tables were requested, they may be adapted or used in part.
- Please print this page for your records and send a copy of it to your publisher/graduate school.
- Appropriate credit for the requested material should be given as follows: "Reprinted (adapted) with permission from (COMPLETE REFERENCE CITATION). Copyright (YEAR) American Chemical Society." Insert appropriate information in place of the capitalized words.
- One-time permission is granted only for the use specified in your request. No additional uses are granted (such as derivative works or other editions). For any other uses, please submit a new request.

BACK | CLOSE WINDOW